Tuning the Photoluminescence Properties of Indium Phosphide Quantum Dots Through Atomistic Surface Chemistry

Nayon Park

A dissertation

submitted in partial fulfillment of the

requirements for the degree of

Doctor of Philosophy

University of Washington

2022

Reading Committee:

Brandi M. Cossairt, Chair

Daniel R. Gamelin

David S. Ginger

Program Authorized to Offer Degree:

Chemistry

University of Washington

Abstract

Tuning the Photoluminescence Properties of Indium Phosphide Quantum Dots Through Atomistic Surface Chemistry

Nayon Park

Chair of the Supervisory Committee:

Brandi M. Cossairt

Department of Chemistry

Colloidal semiconducting nanocrystals, also known as quantum dots, are a leading class of materials for optoelectronic devices that is shaping the technologies of the future. Quantum dots are 2-20 nm in diameter and get their name from the quantum confinement effect, where their size dictates their absorbance and emission wavelengths. The high surface to volume ratio of quantum dots requires that the surface chemistry be carefully controlled to access the desired optoelectronic properties. The solution processability, together with tunable size, shape, and chemical environment of quantum dots opens vast possibilities for surface chemistry and opportunities for prescriptive design through deeper understanding of structure-function relationships. This

dissertation focuses on using atomistic surface chemistry of indium phosphide quantum dots (InP QDs) to improve their photoluminescence properties, including brightness, linewidth, and stability.

Chapter 1 connects the surface chemistry of colloidal quantum dots with their luminescence properties. By following the historical arc that began with shell growth and led to an atomistic description of surface-derived charge trapping, the role of surface chemistry in luminescence properties is presented with an outlook toward emerging concepts such as surface dipoles and vibronic coupling. Chapter 2 discusses tuning of the InP core quantum dot stoichiometry and explores the impacts on the photoluminescence properties of an InP/ZnSe core/shell system. The stoichiometry of both anions (P, As, S, Se) and cations (In, Zn) was controlled at the InP/ZnSe core/shell interface and correlated with the resultant steady-state and time-resolved optical properties. Cluster-model density functional theory supported our experimental findings with the implication of the electronic defect states arising from the interfacial anions. Chapter 3 presents a novel, colloidal synthesis of metal oxide shells on InP QDs and their use as an interface within emissive core/shell heterostructures. Computational modeling was used to explore the optoelectronic properties of a set of metal oxide shelled InP QDs. Characterization techniques such as ^{1}H NMR, X-ray emission spectroscopy (XES), X-ray diffraction (XRD), extended X-ray absorption fine structure spectroscopy (EXAFS) showed evidence of bulk and local structures of the metal oxide shells, and their impact on the final emission properties of InP/ZnSe core/shell QDs was examined.

TABLE OF CONTENTS

LIST OF FIGURES

LIST OF TABLES

ACKNOWLEDGEMENTS

In preparing for concluding this chapter of my life and looking back at the past 5 years, I am completely filled with gratitude toward my mentors, friends, family, and everyone else who have been helping me in this journey. I feel truly lucky that I have so many people to thank, and I hope that I can do my gratitude some justice with the words I am about to put down.

First off, I want to thank Brandi. She has been the most supportive and enthusiastic advocate and advisor for me, as well as a compassionate and positive role model and mentor. I have been encouraged and cheered on by her in ways that I did not always expect to be and in times that I really needed it. Her excitement at our big and small victories, the seasonal themed hangouts that are our lab's traditions, and the birthday cakes that she bakes for every lab member will be some of my fondest memory of grad school. I got to finish up my last manuscript, which makes up the final chapter of this thesis, during the Nanocrystals GRC in Switzerland, just weeks before my defense. I had a really great time, and I cannot say enough how grateful I am that she has been nothing but supportive and looking out for what's best for me until the moment I was finishing up.

I also want to thank my committee members: Daniel Gamelin, David Ginger, Jerry Seidler, and Munira Khalil. They have been supporting me and my development as a chemist through their insightful questions and discussions. I'm truly grateful to have received their guidance, stimulating scientific input, and friendly and enthusiastic support throughout my graduate career.

My time here would not have been half as enjoyable without the past and present members of the Cossairt lab whom I had the absolute privilege to work alongside of. Jenny was my lab mentor who took me under her wing immediately and also introduced me to Penny, who was just down the hallway from us. All the meals that I shared with Jenny and Penny, from the extravagant homemade hotpots to "everyday 50% off" sushi rolls to the all-salmon nigiri plates and chirashi bowls, and the heart-to-hearts with them gave me the most needed and delightful respite from the hectic first year and beyond of grad school. I only tried to emulate the mentorship and friendship they gave me in the earlier years of grad school, and hope that I was even mildly successful in paying it forward to others.

Nobody is in grad school forever, and even as people come and go, I always had a lot of people looking out for me in the lab. I want to give a special shoutout to David, who would stroll over to the right office every now and then to share snacks with me and stay longer for late-night office chats. David and I spent a lot of time on zoom during the pandemic, sometimes coordinating to cook the same meal together, only a screen apart. David has always been willing (his "I" energy pending) to hang out in my typical fashion of spontaneous plan-making and has always been there to gas me up through my ups and downs, even unprompted. Max has always been generous and kind in his mentorship and time, and I was very lucky to be able to tap into his meticulous and awe-inspiring lab skills, intellect, compassion, and many strengths as an organizer. It was truly a blessing to have someone so close by for many years and be able to just walk up and ask for advice that comes from a place of so much expertise and thoughtfulness.

I am so glad that I got to spend a lot of time hanging out with my amazing labmates who are also some of my favorite people: Flo, who loves corn and could probably extract useful feedstock chemicals from corn husks using her photocatalysis skills; Micaela, who loves her cat

Vi and is a hugely talented e-chemist (I will miss our biweekly catch-up dinners); Hao, who loves bubble tea, true to form of his silica shelling science and will likely win a mobile phone one day after already spending a few grands at Haidilao; Ding-Yuan, who loves lychee, travelling, nature and sings Imagine Dragons at karaoke; Cecilia, who loves lots of random things like Weird Al, moose facts, and her accordion with an amazing story; Ian, whose love for karaoke is too true and too real to surpass; Forrest, who loves his adorable pup Kiwi and shooting lasers; Madison, who also enjoys spending time with her two dogs, Gris and Glen; Ric, whose love for teaching and helping others I have benefitted so much from in navigating the steep learning curve for phosphortron (or P-tron, used for P XES); Emily, who loves office banter and somehow managed to be a D1 athlete in grad school; Helen, who loves chocolate ice cream like no one else I know and has shared many enlightening moments in organizing with me; Sam, who loves fun and started blasting music from the 2010s in the lab creating a massive throwback for all of us; Hunter, whose style is always on point from the neon-colored to the tropical-themed items; Grant, who loves cows and analogies, and whose pensive moments I treasure and appreciate; Soren, who is a bit unhinged and loved by everyone for it; Emi, who is the sweetest (she travelled from PNNL to come to my thesis defense) and will graciously be adopting my plants when I leave; and Sarah, who loves reading just about anything and would make enthusiastic book recommendations on topics like climate justice. I couldn't have asked for a better group of people to work and share the ups and down of grad school with, and I feel confident that the Cossairt lab will continue to be a supportive and healthy environment for everyone to do great science.

Outside of the lab, I had some incredible friends in the department who organized around equity and inclusion in academia and worked on improving the research accessibility and mentorship for undergrads with me. Thank you, Marissa, Bri, Theresa, Helen, Flo, and Ben for

taking on the incredibly hard but life-giving work with me so willingly and cheerfully, and Sarah S, Emily C, Alex D, and Emma C for the strength and commitment that carried our dreams of seeing ProCURE's work forward and the nearing-end-of-grad-school camaraderie we shared.

One big facet of my time at graduate school was painted with union organizing with my colleagues throughout the UW campuses for our academic student employees, postdocs, and now research scientists' union, UAW 4121. I'm eternally grateful for the mentorship and friendship of the following people: Dan, Max F, Shua, Sam S, Levin, Emily, Soohyung, Yuying, David P. This work has been the light of my graduate life, and these people and their incredible leadership and good hearts have been a constant source of inspiration for me in my personal growth as a community member and in becoming who I am today.

Closer to home, I had the greatest joy of having friends who were just minutes away by walk to spend the holidays and celebrate our way through grad school with: Ather, Alex, Ellen, Remy, Jialin, and Zoey (may this sweetest, fluffiest cat rest in peace). They have been my family and home away from home, and I am excited to see where our lives will take us next as some of us start to embark on our new journeys.

In my wider net of support system who have long been constant sources of friendship, joy, and comfort are Joyce, Haley, John, Daniel, Jin, Serena, Lisa, Max E, Roma, Sameen, Izzi, and Conner. I appreciate and cherish all the moments we have shared together near and far from each other and look forward to many more of lives' events.

And most importantly, my core bedrock that makes everything I do possible is my family, my mom and dad and my brother, Gunou. I am so lucky to have them as my family, to travel and make lots of memories with them. I am so proud of my brother for everything he does so thoughtfully and with a lot of care and love in looking out for our family while I have been

physically absent back at home. I hope he knows that our long phone conversations have both been a refreshing change in pace and a chance for me to be deeply impressed and touched by this thoughtfulness.

I look up to my mom and dad a lot and find myself following their examples. They are constant inspiration for me to keep learning to new things and to extend myself, while at times to remember to pause and look up at the skies and observe the changing seasons. My dad has always had all of his faith in me and made sure that I know that by always being ready to cheer me on and letting me carry myself to where I wanted to be. My mom has always been my safe place and continues to bring a lot of clarity for me in moments of stress and uncertainty. Without my family, I truly wouldn't be where I am today. I'm beyond grateful for them, and this accumulation of work from my past 5 years is dedicated to them.

DEDICATION

To umma and appa

Joohee Hong and Heung Sun Park

And to my brother, Gunou

Chapter 1. INTRODUCTION

This section has been published as a perspectives article.[1]

Quantum dots are used in the research laboratory and in commercial applications for their bright, size-tunable luminescence. While empirical synthesis and processing optimization have led to many quantum dot systems with photoluminescence quantum yields at or approaching 100%, our understanding of the chemical principles that underlie this performance and our ability to access such materials on demand has lagged. In this perspective, we present the status of our understanding of the connections between surface chemistry and quantum dot luminescence. We follow the historical arc that began with shell growth, which then led to an atomistic description of surface-derived charge trapping, and finally has brought us to a more nuanced picture of the role of surface chemistry on luminescence properties, including emerging concepts like surface dipoles and vibronic coupling.

1.1 Understanding Quantum Dot Surface Chemistry for Improved Photoluminescence

Following more than three decades of constant development, today quantum dots are widely used in displays, solid state lighting, and biological imaging for their bright and tunable luminescence characteristics and their ease of processing. For some compositions, including CdSe and InP, photoluminescence quantum yields (PL QYs) in the visible approaching 100% are now achievable, if not routine. While bright emission can sometimes be a coincidental byproduct of synthesis or the result of empirical optimization, a deep understanding of the underlying structural and electronic properties that control luminescence is critical to the design of bright, color-pure quantum dot emitters. Today, it is appreciated that many properties of quantum dots are controlled

not only by the quantum confined nature of the semiconductor core, but also in large part by their surface chemistry. The question we want to address in this perspective is: How does surface chemistry impact quantum dot luminescence? A primary answer to this question relates to under-passivated atoms or defects at the surface that serve as sites for charge carrier trapping. An early synthetic strategy developed to eliminate these trap sites was shelling, which aimed to separate the quantum dot core and its charge carriers from the surrounding environment using a wider bandgap semiconductor layer that is structurally well-matched to minimize strain at the core/shell interface. Our understanding of the atomistic details that underlie luminescence enhancement in shelled quantum dots has been advanced by detailed spectroscopic and structural investigations, as well as by targeted ionic and molecular chemical treatments of the quantum dot surface. Taken together, these studies are revealing a picture that is more complex and nuanced than previously appreciated. Factors including alloying (or doping), surface dipoles and (more generally) ligand electronegativity, and vibronic coupling are emerging as critical factors in understanding the origins of quantum dot luminescence and consequently our ability to control it. In this perspective, we seek to piece this knowledge together to reveal the current state of how surface chemistry impacts luminescence in quantum dots and how this knowledge can be used to advance the synthesis of perfect luminophores of diverse compositions for next generation technologies.

1.2 SHELLING

To reliably increase the quantum yield of colloidal quantum dots, a shell of a wider bandgap semiconducting material is grown on the surface (**Figure 1.1**). This serves a two-fold purpose; to localize the photoexcited electron/hole pair to the core of the material and to help passivate surface defects that are largely responsible for the loss of luminescence in these materials. The traditional type I architecture has been explored in depth, with quantum yields reaching 75% for materials

such as CdSe/ZnS.[2] Additionally, many have reported a remarkable increase in PL QY by shelling CdSe with CdS.[3–5] However, when a thicker 8 monolayer CdS shell is applied, a red shift is observed along with a lengthened exciton lifetime, features indicative of a shift to a quasi-type II electronic structure (**Figure 1.1**). In this quasi-type II system, the conduction band edge energies of the core and shell materials are aligned, allowing the electron to be delocalized to the shell where it could encounter an electron trap. However, the confinement of the photogenerated hole to the core of the material leads to the suppression of nonradiative recombination as the carriers are spatially separated – only the interaction of the trapped electron with a thermal vibration will allow the electron to repopulate the internal excitonic energy level and radiatively recombine. One of the first thick-shelled, quasi-type II, CdSe/CdS systems was described by Bawendi et al. with reported PL QY reaching up to 98%. This was accomplished by an alternating deposition of cadmium and sulfur to the surface of the CdSe nanocrystal using a selective ion layer adsorption and reaction approach.[5] Further development of these thick-shelled CdSe/CdS heterostructures was achieved through altering the shell precursor composition, with octanethiol replacing $S(SiMe_3)_2$ as the chalcogen precursor. This change in chemistry allowed quantum yields to be maintained at or above 97%, but the average on-time of the materials increased from 60 to 90%, creating more reliably emissive ensembles.[6] Alivisatos et al. reported that omitting oleylamine results in reduced desorption of Z-type $Cd(oleate)_2$ surface ligands and thus higher ligand coverage, along with reduced charge trapping.[7] By first controlling the surface stoichiometry of the core and inner shells, then performing additional shelling reactions, the quantum yield can reach as high as 99.6% for 8 monolayer-shell CdSe/CdS.

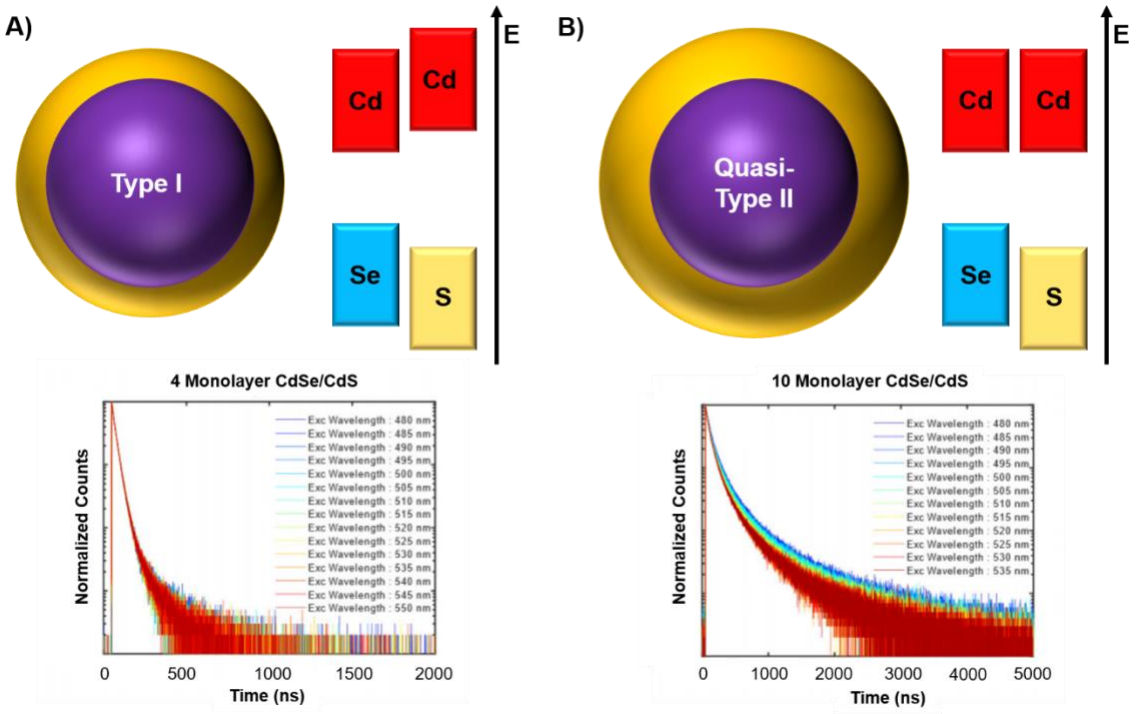

Figure 1.1. Quantum dot shelling and classification by relative band edge alignment into A) type I and B) quasi-type II systems. Representative TR PL data for each type in the case of CdSe/CdS QDs are shown. Adapted in part with permission from ref. 7. Copyright 2019 The American Association for the Advancement of Science.

While II-VI QDs have relied on these quasi-type II architectures to achieve the highest PL QY, III-V QDs have predominantly relied on the type I architecture to achieve high PL QY by confining the photogenerated carriers to the core and avoiding recombination at non-luminescent surface traps.[8] However, due to lattice strain between the InP core and the typical ZnS shell layer, new approaches using gradient shells have risen in popularity as a way to manage lattice mismatch and improve quantum yield further.[9,10] Although gradient shells have dominated research for the last decade, a recent shift in the zeitgeist has occurred, with treatment/tuning of the native core's surface before shelling emerging as a highly important factor. Control over the surface

stoichiometry of the native nanocrystals resulted in PL QYs as high as 93% for III-V based emitters.[11] By removing excess indium at the surface of the core, In atoms were prevented from incorporating into the shell, allowing the pristine shell layer to effectively serve as an energetic barrier to confine the photogenerated carriers to the core. This fine surface control has been further augmented by surface etching using HF prior to shelling InP QDs. This process removes both excess indium on the surface and phosphates that results from surface oxidation. The removal of these species, followed by the growth of gradient ZnSeS shell led to near-unity PL QY, with high stability maintained for ~4300 hrs.[12]

1.3 Atomistic Chemical Modification

Taken together, the historical development of shelling chemistry and the assessment of its impact on PL QY have revealed the importance of control of the core/shell interface in achieving unity quantum yields. Pushing our understanding beyond these empirically determined design principles, however, necessitates an atomistic description of QD surface chemistry. A wide variety of chemical treatments have led to enhancement of PL QYs without the growth of a full shell, prompting more in-depth investigations to interrogate the origin of these effects. This atomistic approach, in contrast with shelling, has allowed for examining cationic or anionic surface sites separately, revealing the critical role of stoichiometry and the presence of undercoordinated surface sites in QD luminescence (**Figure 1.2**). A variety of both shallow and deep trap states have been identified and implicated spectroscopically for II-VI and III-V quantum dots.[13–17] Eliminating these surface traps is a crucial step in obtaining bright QDs because these traps act as local energy minima that can prevent or delay electron-hole recombination.[18]

Theoretical models have provided guiding principles for the chemical identity of surface traps that can be experimentally verified. For example, for II-VI QDs with a zinc blende structure,

it has been concluded that a primary source of surface hole traps are stable two-coordinate chalcogenide ions at the QD surface that arise from the displacement of, or a synthesis-specific lack of termination by, Z-type metal complexes.[16,19] Intriguingly, two and three-coordinate metal ions at the QD surface did not show a propensity to form mid-gap trap states. Because of this, the addition of neutral L-type ligands to the undercoordinated surface sites does not dramatically impact the luminescence properties in these systems.[19] Furthermore, it has been shown that depending on the relative positions of the valence and conduction band edges of a QD material, chemical oxidation (*i.e.*, by air) or n-type doping during synthesis can result in surface speciation that also introduces mid-gap traps.[16]

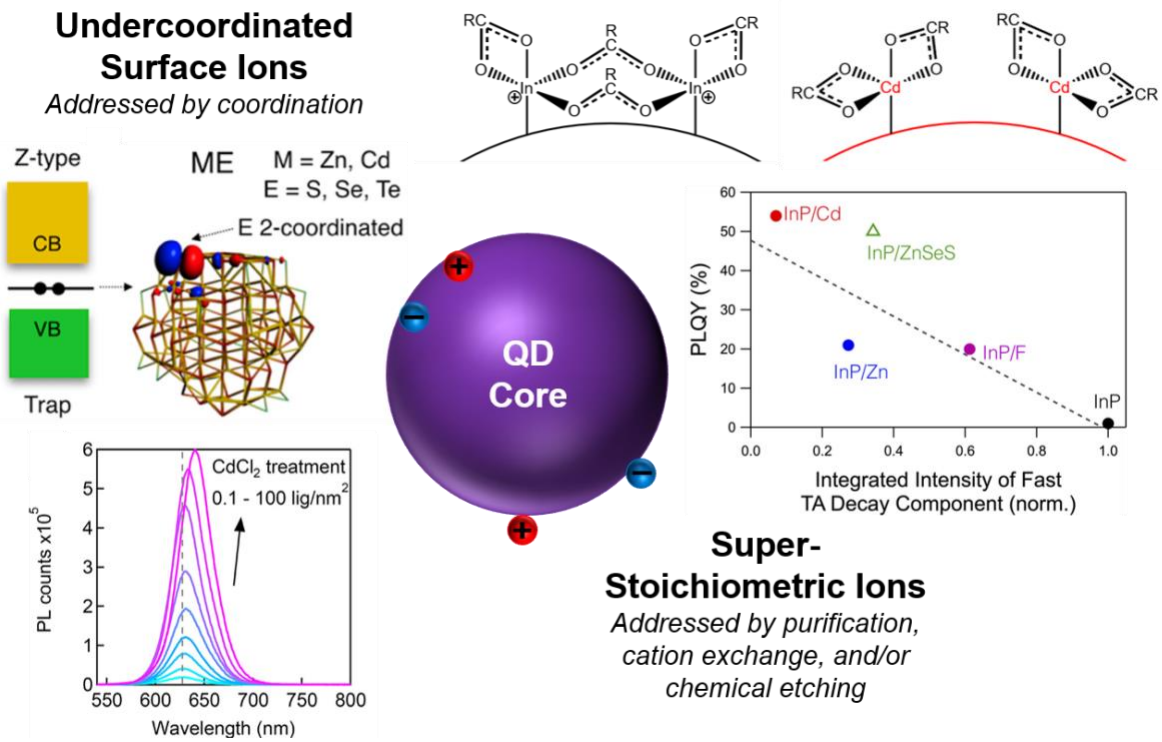

Figure 1.2. Electronic trap sites in binary QDs arising from undercoordinated surface ions, as seen for II-VI QDs, and super-stoichiometric ions, as seen for III-V QDs. Adapted in part with permission from ref. 19-21. Copyright 2016, 2018, and 2019, respectively, The American Chemical Society.

These theoretical studies suggest that the stoichiometry of QD surfaces should play a dominant role in QD PL QY and our ability to tune it. While as-synthesized QDs are typically cation-rich, the surface can be post-synthetically modified to tune the cation to anion ratio.[22] Sfeir et al. reported on the carrier dynamics of CdSe QDs whose surface composition was controlled from cation-rich (~80% surface Cd) to stoichiometric (~50% surface Cd) using N,N,N',N'-tetramethylethylenediamine (TMEDA).[23] Tuning the QD stoichiometry in this way requires consideration of the number and type of ligands to maintain charge neutrality, which was achieved through the displacement of the metal-ligand complex, *i.e.* Cd carboxylate. It was observed that the reduced surface Cd fraction led to a nonlinear decrease in the PL QY and an increase in the PL decay rate due to hole trapping at the newly exposed surface Se atoms. From these results, surface coverage by Cd carboxylate and the rate of hole trapping were correlated, noting the heterogeneity in the chemical and electronic structure of the surface Se sites. In terms of the surface structure, it was hypothesized that such heterogeneity may arise from the facet-dependent orbital interactions of adjacent undercoordinated Se atoms. The (111) plane, where there is higher population of these undercoordinated Se atoms, is likely to lower the energy of hole trap states through orbital interactions, while the correct orbital symmetry of Se *p*-orbitals on the (100) plane may contribute to the formation of the surface Se trap states.

This effect of stoichiometry modulation has been extended to other surface treatments, with a deep focus on Lewis acids to passivate undercoordinated anion sites and thereby eliminate hole traps as discussed above. For example, it was demonstrated that QD surface treatment with Z-type ligands (*i.e.* metal halides and carboxylates) leads to an increase in the PL QY to varying degrees depending on the identity of the Z-type ligand.[20] While the highest PL QYs (>70 %) were achieved with $InCl_3$ and $CdCl_2$ on phosphonate-capped CdTe QDs, the effects were also generalized to

CdSe, CdS, InP, and Zn-doped InP QDs. Moderate increases in PL QY were attributed to weaker binding and steric repulsion based on the observation that smaller halide ions and shorter carboxylate chain lengths trend towards higher PL QY. It was also noted that ligands such as amines and alkylammonium chloride that are not Z-type ligands give rise to a smaller increase in PL QY. While theoretical models predicted only anion-related trap states upon removal of Z-type ligands, these experimental results drew attention to cation-related trap states, adding to the complexity of addressable QD surface states, especially outside the II-VI family of compounds where increased covalency could render super-stoichiometric cations sites for electron trapping.

Phenomenologically similar effects of Lewis acids on the PL QY of carboxylate-capped InP QDs have been previously reported by our group. We observed that the surface treatment of InP QDs with Zn or Cd carboxylate leads to increases in the PL QY of up to >50 % and confirmed that Zn and Cd carboxylate displaces the native surface In carboxylate based on elemental analysis and the eventual formation of independent In_2O_3 particles.[24] Further, extended X-ray absorption fine structure (EXAFS) analysis corroborated that the divalent metal cations were mostly on the surface rather than incorporated into the InP core. This surface treatment is reversible with the use of TMEDA, which cleaves off metal carboxylate from the surface and results in a consistent decrease in PL QY upon titration.

In a study that followed, ultrafast TA and TR PL spectroscopy were used in tandem to probe the charge carrier dynamics of the surface-treated InP QDs.[21,25] Interestingly, it was revealed that of both electron and hole traps that exist in InP QDs, it is the electron traps that are eliminated as a result of the surface treatment by the divalent Lewis acids. A similar effect was also observed for treatments with fluoride. Taken together, this elimination of electron traps points to In dangling bonds as a possible culprit in the low PL QY. Coordination by small, hard anions like fluoride, or

replacing undercoordinated In with Cd or Zn carboxylate eliminate these sources of electron trapping. This mechanism of trivalent indium carboxylate displacement by divalent Lewis acids was recently given further support from thermodynamic measurements by Alivisatos et al. In these studies, isothermal titration calorimetry was used to show that metal halides displace indium carboxylates, enhancing the luminescence, and revealing the importance of interligand interactions at QD surfaces.[26]

1.4 THINKING BEYOND TRAP STATES

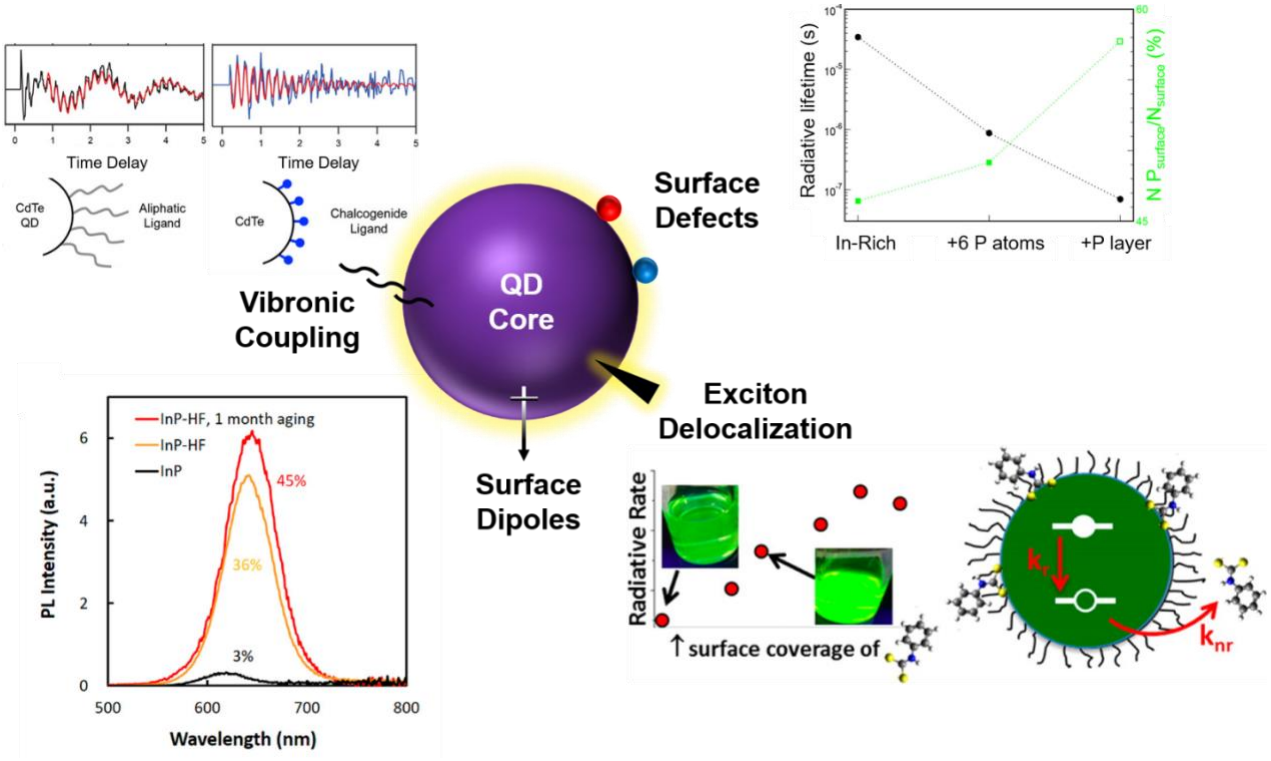

Figure 1.3. Modulation of QD optical properties by modulation of surface dipoles, binding of exciton delocalizing ligands, vibronic coupling, and surface stoichiometry. Adapted in part with permission from ref. 28, 30, 32, 33. Copyright 2018, 2016, 2018, and 2020, respectively, The American Chemical Society.

Atomistic surface modifications can do more than simply passivate or introduce electronic trap states (**Figure 1.3**). Fluorination of an InP QD surface is a facile method for PL QY enhancement that has been known for as long as the synthesis of colloidal InP QDs itself.[27] Recently, Alivisatos et al. revisited the surface passivation of InP with fluoride and offered new hypotheses regarding the structural and electronic modifications that influence the PL properties.[28] The observation that surface fluoride ions, at low concentration, cause a redshift in both absorption and emission rather than a blueshift expected from surface etching was attributed to greater delocalization of electrons in the conduction band, along with the decrease of the optical oscillator strength due to the highly electronegative fluoride layer. The oscillator strength of QDs, which is dependent on the QD ligand environment and influences the shape and symmetry of the charge carrier wavefunctions, was calculated to show a decrease with fluoride passivation of surface In sites. This agrees with the longer radiative PL decay time (*i.e.*, lower radiative recombination rate) that was measured, as oscillator strength is proportional to the radiative recombination rate. The strong electron withdrawing property of fluorides, combined with their small size and high binding affinity, makes the optical properties of InP/F distinct from as synthesized or shelled InP QDs. Upon further investigation of metal halide passivation on InP QD surfaces, it was proposed that PL QY enhancement is influenced by the electron-withdrawing effects of the surface ligands that withdraw the negative charge from the surface and reduce hole trapping.[26]

The effects of surface ligands that are "exciton-delocalizing" have been reported by Weiss et al. in the case of CdSe QDs capped with phenyldithiocarbamate (PTC) by ligand exchange.[29,30] To achieve mixing with the exciton wavefunction, the ligand orbitals must have a suitable match in both energy and symmetry. Successful electronic coupling of QD exciton and ligand orbitals in the case of PTC was demonstrated by a characteristic redshift, along with an increase in the PL

QY and the oscillator strength of emissive transitions, due to the delocalization of the charge carrier wavefunctions. Similarly, Dukovic et al. showed that inorganic chalcogenide ligands, such as Se^{2-} on CdTe QDs, behave as if they are a passivating shell layer.[31] Significant delocalization of the carrier wavefunctions beyond the QD surface itself was observed.

If chalcogenide ligands can couple strongly to exciton wavefunctions in II-VI QDs, this leads to a natural question about the role of pnictides on III-V QDs. As discussed previously, Peng et al. have recently demonstrated experimentally that stoichiometry control of InP cores to increase the relative ratio of P:In is a viable strategy to enhance QY in these materials.[11] Their hypothesis focused on reducing indium alloying in the shell as the mechanism for PL QY enhancement, but recent computational work may suggest an additional factor. Califano et al. created atomistically ideal and fully passivated InP QDs and found that these structures may still exhibit undesirable PL properties.[33] The long radiative lifetimes, broad linewidths, and low PL QY were attributed to a relative displacement between the electron and hole wavefunctions and therefore reduced coupling between them.[33] The addition of a few P atoms on the In-rich surface, however, was shown to reduce the radiative lifetime and the Stokes shift, suggesting a path forward to increasing QY by controlling the core stoichiometry.

A complex relationship between photoluminescence and vibrational lattice modes (phonons) is also emerging. Bawendi et al. demonstrated the interplay between luminescence broadening and the shell composition of CdSe/CdS QDs.[34] In this study, it was found that the most drastic broadening occurs where the photoexcited electron wavefunction spreads into the shell, while the hole stays localized in the core. An interesting consequence of this decreased wavefunction overlap is polarization of the nanocrystal, which enhances electron coupling to longitudinal optical phonons. Alternatively, this increase can also be explained by increased

Fröhlich coupling in the CdS compared to CdSe – the photoexcited electron can also interact with shell phonons more than it does with the core.

Phonons have also been noted to play a critical role in the emission of InP core/shell structures, with recombination processes involving both optical and acoustic phonons of the core and shell materials.[35] As the shell composition changes and allows for more electron wavefunction delocalization, slight polarization of the nanocrystal occurs and the electron-phonon coupling is increased, resulting in decreased lifetimes observed via low temperature TRPL spectroscopy. Notably, at low temperatures, the dark state of InP is dominant, requiring electron-phonon coupling to become emissive. Phonons also broaden the dark state emission spectrum of InP, suggesting another potential avenue for tuning the emission linewidth, although the impacts for room-temperature applications in ensemble samples remains unknown.

Beyond shelling, phonon interactions can also be tuned by altering the capping ligands of the material.[32] By tuning the capping groups from aliphatic ligands to inorganic chalcogenides for example, it is possible to critically damp the acoustic phonons present in the material, ascribed to energy dissipation once phonons reach the surface and dissipates into the surroundings. In other studies, an exciton-induced electron density shift in InP clusters has been demonstrated to directly affect the vibrational motion of the carboxylate ligands on the surface using transient IR spectroscopy.[36] These results leave many questions regarding the extent of vibronic coupling to surface ligands and how to use this property to direct exciton relaxation pathways, a topic we expect will become highly relevant to future quantum dot design as the application space continues to broaden beyond the realm of displays, lighting, and biological imaging.

1.5 OUTLOOK

Chemists, materials scientists, and engineers have contributed to significant advances in our understanding of how surface chemistry impacts QD luminescence by combining synthesis, spectroscopy, and experimentally verifiable theoretical models. This work has moved us from empirical optimization of shelling chemistry, to the ability to atomistically tailor the surface chemistry in order to specifically address relevant defect or trap sites, and ultimately achieve improved optical properties through rational design. What's more, the role of ligand coupling through orbital mixing, phonon interactions, and surface dipole modulation has created a vast new parameter space for system design. Whereas early high performing QD emitters relied on thick, insulating shell layers, restricting applications to passive down-conversion, more modern approaches that focus on atomistic interfacial tuning generate core/shell QDs with high quantum yields that can still be modulated through electrical injection, paving the way for near horizon electroluminescent systems. As our sophistication to take advantage of trap passivation and ligand coupling advances, future generations of QDs with perfect quantum yields and no shell layers may be possible, which may open new opportunities in areas like catalysis and quantum information.

In the following chapters, I will present studies that focus on atomistic interfacial tuning of core/shell QDs by modifying the anion and cation stoichiometry or growing a thin metal oxide shell at the interface. In Chapter 2, we started with the hypothesis that hole traps may be effectively eliminated with anionic surface treatments (P, As, S, Se). In Chapter 3, we proposed that the oxidative instability of InP surfaces might be leveraged through surface oxide design (ZnO, CdO, GaO_x, AlO_x) to improve emission and overall stability. In both studies, the connection between atomistic surface modification and the resultant optoelectronic properties was examined through a combination of synthesis, characterization, and computational modelling. Ultimately through an

atomistic understanding of the surface structure, synthetic fine-tuning of the QD emission is not only possible but opens up new possibilities for predictive design. The structural complexity that is prescribed from a given synthesis and that is altered through post-synthetic surface chemistry can be widely leveraged for improved functionality in these technologically relevant colloidal optoelectronic nanomaterials.

1.6 REFERENCES

(1) Eagle, F. W.; Park, N.; Cash, M.; Cossairt, B. M. Surface Chemistry and Quantum Dot Luminescence: Shell Growth, Atomistic Modification, and Beyond. *ACS Energy Lett.* **2021**, *6* (3), 977–984.

(2) Hao, J.; Liu, H.; Miao, J.; Lu, R.; Zhou, Z.; Zhao, B.; Xie, B.; Cheng, J.; Wang, K.; Delville, M.-H. A Facile Route to Synthesize CdSe/ZnS Thick-Shell Quantum Dots with Precisely Controlled Green Emission Properties: Towards QDs Based LED Applications. *Sci. Rep.* **2019**, *9* (1), 12048.

(3) Li, J. J.; Wang, Y. A.; Guo, W.; Keay, J. C.; Mishima, T. D.; Johnson, M. B.; Peng, X. Large-Scale Synthesis of Nearly Monodisperse CdSe/CdS Core/Shell Nanocrystals Using Air-Stable Reagents via Successive Ion Layer Adsorption and Reaction. *J. Am. Chem. Soc.* **2003**, *125* (41), 12567–12575.

(4) Chen, Y.; Vela, J.; Htoon, H.; Casson, J. L.; Werder, D. J.; Bussian, D. A.; Klimov, V. I.; Hollingsworth, J. A. "Giant" Multishell CdSe Nanocrystal Quantum Dots with Suppressed Blinking. *J. Am. Chem. Soc.* **2008**, *130* (15), 5026–5027.

(5) Greytak, A. B.; Allen, P. M.; Liu, W.; Zhao, J.; Young, E. R.; Popović, Z.; Walker, B. J.; Nocera, D. G.; Bawendi, M. G. Alternating Layer Addition Approach to CdSe/CdS Core/Shell Quantum Dots with near-Unity Quantum Yield and High on-Time Fractions. *Chem. Sci.* **2012**, *3*, 2028–2034.

(6) Chen, O.; Zhao, J.; Chauhan, V. P.; Cui, J.; Wong, C.; Harris, D. K.; Wei, H.; Han, H.-S.; Fukumura, D.; Jain, R. K.; Bawendi, M. G. Compact High-Quality CdSe–CdS Core–Shell Nanocrystals with Narrow Emission Linewidths and Suppressed Blinking. *Nat. Mater.* **2013**, *12* (5), 445–451.

(7) Hanifi, D. A.; Bronstein, N. D.; Koscher, B. A.; Nett, Z.; Swabeck, J. K.; Takano, K.; Schwartzberg, A. M.; Maserati, L.; Vandewal, K.; Burgt, Y. van de; Salleo, A.; Alivisatos, A. P. Redefining Near-Unity Luminescence in Quantum Dots with Photothermal Threshold Quantum Yield. *Science* **2019**, *363* (6432), 1199–1202.

(8) Liang, L.; Reiss, P. One-Pot Synthesis of Highly Luminescent InP/ZnS Nanocrystals without Precursor Injection. *J. Am. Chem. Soc.* **2008**, *130*, 11588–11589.

(9) Mulder, J. T.; Kirkwood, N.; De Trizio, L.; Li, C.; Bals, S.; Manna, L.; Houtepen, A. J. Developing Lattice Matched ZnMgSe Shells on InZnP Quantum Dots for Phosphor Applications. *ACS Appl. Nano Mater.* **2020**, *3* (4), 3859–3867.

(10) Lim, J.; Bae, W. K.; Lee, D.; Nam, M. K.; Jung, J.; Lee, C.; Char, K.; Lee, S. InP@ZnSeS, Core@Composition Gradient Shell Quantum Dots with Enhanced Stability. *Chem. Mater.* **2011**, *23* (20), 4459–4463.
(11) Li, Y.; Hou, X.; Dai, X.; Yao, Z.; Lv, L.; Jin, Y.; Peng, X. Stoichiometry-Controlled InP-Based Quantum Dots: Synthesis, Photoluminescence, and Electroluminescence. *J. Am. Chem. Soc.* **2019**, *141* (16), 6448–6452.
(12) Won, Y.-H.; Cho, O.; Kim, T.; Chung, D.-Y.; Kim, T.; Chung, H.; Jang, H.; Lee, J.; Kim, D.; Jang, E. Highly Efficient and Stable InP/ZnSe/ZnS Quantum Dot Light-Emitting Diodes. *Nature* **2019**, *575* (7784), 634–638.
(13) Mićić, O. I.; Nozik, A. J.; Lifshitz, E.; Rajh, T.; Poluektov, O. G.; Thurnauer, M. C. Electron and Hole Adducts Formed in Illuminated InP Colloidal Quantum Dots Studied by Electron Paramagnetic Resonance. *J. Phys. Chem. B* **2002**, *106* (17), 4390–4395.
(14) Chestnoy, N.; Harris, T. D.; Hull, R.; Brus, L. E. Luminescence and Photophysics of CdS Semiconductor Clusters: The Nature of the Emitting Electronic State. *J. Phys. Chem.* **1986**, *90*, 3393–3399.
(15) Veamatahau, A.; Jiang, B.; Seifert, T.; Makuta, S.; Latham, K.; Kanehara, M.; Teranishi, T.; Tachibana, Y. Origin of Surface Trap States in CdS Quantum Dots: Relationship between Size Dependent Photoluminescence and Sulfur Vacancy Trap States. *Phys. Chem. Chem. Phys.* **2014**, *17* (4), 2850–2858.
(16) Giansante, C.; Infante, I. Surface Traps in Colloidal Quantum Dots: A Combined Experimental and Theoretical Perspective. *J Phys Chem Lett* **2017**, *8* (20), 5209–5215.
(17) Greaney, M. J.; Couderc, E.; Zhao, J.; Nail, B. A.; Mecklenburg, M.; Thornbury, W.; Osterloh, F. E.; Bradforth, S. E.; Brutchey, R. L. Controlling the Trap State Landscape of Colloidal CdSe Nanocrystals with Cadmium Halide Ligands. *Chem. Mater.* **2015**, *27* (3), 744–756.
(18) Singh, K.; Voznyy, O. It's a Trap! Fused Quantum Dots Are Undesired Defects in Thin-Film Solar Cells. *Chem* **2019**, *5* (7), 1692–1694.
(19) Houtepen, A. J.; Hens, Z.; Owen, J. S.; Infante, I. On the Origin of Surface Traps in Colloidal II–VI Semiconductor Nanocrystals. *Chem. Mater.* **2017**, *29* (2), 752–761.
(20) Kirkwood, N.; Monchen, J. O. V.; Crisp, R. W.; Grimaldi, G.; Bergstein, H. A. C.; du Fossé, I.; van der Stam, W.; Infante, I.; Houtepen, A. J. Finding and Fixing Traps in II–VI and III–V Colloidal Quantum Dots: The Importance of Z-Type Ligand Passivation. *J. Am. Chem. Soc.* **2018**, *140* (46), 15712–15723.
(21) Hughes, K. E.; Stein, J. L.; Friedfeld, M. R.; Cossairt, B. M.; Gamelin, D. R. Effects of Surface Chemistry on the Photophysics of Colloidal InP Nanocrystals. *ACS Nano* **2019**, *13* (12), 14198–14207.
(22) Anderson, N. C.; Hendricks, M. P.; Choi, J. J.; Owen, J. S. Ligand Exchange and the Stoichiometry of Metal Chalcogenide Nanocrystals: Spectroscopic Observation of Facile Metal-Carboxylate Displacement and Binding. *J. Am. Chem. Soc.* **2013**, *135* (49), 18536–18548.
(23) Busby, E.; Anderson, N. C.; Owen, J. S.; Sfeir, M. Y. Effect of Surface Stoichiometry on Blinking and Hole Trapping Dynamics in CdSe Nanocrystals. *J. Phys. Chem. C* **2015**, *119* (49), 27797–27803.
(24) Stein, J. L.; Mader, E. A.; Cossairt, B. M. Luminescent InP Quantum Dots with Tunable Emission by Post-Synthetic Modification with Lewis Acids. *J. Phys. Chem. Lett.* **2016**, *7* (7), 1315–1320.
(25) Mundy, M. E.; Eagle, F. W.; Hughes, K. E.; Gamelin, D. R.; Cossairt, B. M. Synthesis and Spectroscopy of Emissive, Surface-Modified, Copper-Doped Indium Phosphide Nanocrystals. *ACS Materials Lett.* **2020**, *2* (6), 576–581.

(26) Calvin, J. J.; Swabeck, J. K.; Sedlak, A. B.; Kim, Y.; Jang, E.; Alivisatos, A. P. Thermodynamic Investigation of Increased Luminescence in Indium Phosphide Quantum Dots by Treatment with Metal Halide Salts. *J. Am. Chem. Soc.* **2020**, *142* (44), 18897–18906.
(27) Micic, O. I.; Sprague, J.; Lu, Z.; Nozik, A. J. Highly Efficient Band Edge Emission from InP Quantum Dots. *Appl. Phys. Lett.* **1996**, *68*, 3150–3152.
(28) Kim, T.-G.; Zherebetskyy, D.; Bekenstein, Y.; Oh, M. H.; Wang, L.-W.; Jang, E.; Alivisatos, A. P. Trap Passivation in Indium-Based Quantum Dots through Surface Fluorination: Mechanism and Applications. *ACS Nano* **2018**, *12* (11), 11529–11540.
(29) Frederick, M. T.; Weiss, E. A. Relaxation of Exciton Confinement in CdSe Quantum Dots by Modification with a Conjugated Dithiocarbamate Ligand. *ACS Nano* **2010**, *4* (6), 3195–3200.
(30) Jin, S.; Harris, R. D.; Lau, B.; Aruda, K. O.; Amin, V. A.; Weiss, E. A. Enhanced Rate of Radiative Decay in CdSe Quantum Dots upon Adsorption of an Exciton-Delocalizing Ligand. *Nano Lett.* **2014**, *14* (9), 5323–5328.
(31) Schnitzenbaumer, K. J.; Dukovic, G. Chalcogenide-Ligand Passivated CdTe Quantum Dots Can Be Treated as Core/Shell Semiconductor Nanostructures. *J. Phys. Chem. C* **2014**, *118* (48), 28170–28178.
(32) Schnitzenbaumer, K. J.; Dukovic, G. Comparison of Phonon Damping Behavior in Quantum Dots Capped with Organic and Inorganic Ligands. *Nano Lett.* **2018**, *18* (6), 3667–3674.
(33) Rodosthenous, P.; Gómez-Campos, F. M.; Califano, M. Tuning the Radiative Lifetime in InP Colloidal Quantum Dots by Controlling the Surface Stoichiometry. *J. Phys. Chem. Lett.* **2020**, *11* (23), 10124–10130.
(34) Cui, J.; Beyler, A. P.; Coropceanu, I.; Cleary, L.; Avila, T. R.; Chen, Y.; Cordero, J. M.; Heathcote, S. L.; Harris, D. K.; Chen, O.; Cao, J.; Bawendi, M. G. Evolution of the Single-Nanocrystal Photoluminescence Linewidth with Size and Shell: Implications for Exciton–Phonon Coupling and the Optimization of Spectral Linewidths. *Nano Lett.* **2016**,
(35) Brodu, A.; Ballottin, M. V.; Buhot, J.; Dupont, D.; Tessier, M.; Hens, Z.; Rabouw, F. T.; Christianen, P. C. M.; de Mello Donega, C.; Vanmaekelbergh, D. Exciton-Phonon Coupling in InP Quantum Dots with ZnS and (Zn, Cd)S Shells. *Phys. Rev. B* **2020**, *101* (12), 125413.
(36) Leger, J. D.; Friedfeld, M. R.; Beck, R. A.; Gaynor, J. D.; Petrone, A.; Li, X.; Cossairt, B. M.; Khalil, M. Carboxylate Anchors Act as Exciton Reporters in 1.3 Nm Indium Phosphide Nanoclusters. *J. Phys. Chem. Lett.* **2019**, *10* (8), 1833–1839.

Chapter 2. Tuning the Interfacial Stoichiometry of InP Core and InP/ZnSe Core/Shell Quantum Dots

This work has been published.[1]

2.1 INTRODUCTION

Advances in the synthetic optimization of InP-based quantum dots (QDs) have led this material to a position of prominence for commercial display applications.[2–7] Recent demonstrations of near-unity quantum yield and >20% external quantum efficiency in electroluminescent devices have placed InP on par with cadmium-based quantum dot emitters.[8,9] The chemical design principles that underlie these advances, however, remain poorly understood. The atomistic synthesis of colloidal quantum dots that are defect-free, both structurally and electronically, has long been a topic of fundamental research and remains so even today. Typical solution-based hot injection and heat-up synthesis methods generate quantum dots that are marred by surface defects that create electronic trap states within the semiconductor band gap.[10–15] These mid-gap states introduce both radiative and non-radiative relaxation pathways that compete effectively with the desired band-edge recombination process. Consequently, the need to understand and modulate the surface chemistry that governs these photophysical properties has risen to paramount importance in the field.

The effects of surface passivation and ligand type on the photoluminescence and charge transfer properties have been abundantly reported.[16–24] Recent studies on InP-based core/shell quantum dots have reported a diverse set of factors affecting the photoluminescence properties of emissive InP QDs, including uniformity of the InP core,[25,26] thickness and composition of zinc chalcogenide shell,[25–27] electron and hole wavefunction overlap,[25,26] surface defects (such as

oxidized species) or dangling bonds,[8,24] and stacking faults at the core/shell interface due to lattice mismatch.[28,29] The achievement of 100% photoluminescence quantum yield (PL QY) has been attributed to well-confined electron and hole wavefunctions through engineering the inner shell layer,[26,30] removal of oxidative defects by etching with HF prior to shelling,[8] a well-passivated surface on a stoichiometric InP core,[9] and removal of indium defects in the shell by an additional washing step.[9,31] The high sensitivity of optical properties to the core stoichiometry and interface morphology has been highlighted in recent computational studies.[32,33] These considerations are influenced by the composition and the chemical environment at the core/shell interface, highlighting the need for further investigation on the nature of surface trap states and how to deterministically treat the quantum dot core en route to highly emissive, defect-free core/shell QDs.

In this study, we have sought to modify the interfacial stoichiometry of emissive InP QDs using surface-limited reaction chemistry to correlate interfacial composition with the PL properties of the resulting core and core/shell materials. Reactive silyl reagents containing the desired anion (P, Se, S, or As) were added to In-rich InP QDs capped with carboxylate ligands to obtain sub-stoichiometric to anion-rich cores. Optical spectroscopy of the resultant core QDs indicates delocalization of the exciton wavefunction and relaxation of exciton confinement. The efficacy of the reactive silyl reagents in shifting the stoichiometry of shelled QDs and their impact on improving the epitaxial growth to reduce ensemble heterogeneity were demonstrated. Time-resolved photoluminescence (TR PL) spectroscopy revealed that interfacial modulation of InP/ZnSe QDs results in similar decay dynamics on the ns timescale, suggesting that changes in PL QY can be attributed to new defect-related pathways related to hole trapping on the ps timescale promoting non-radiative recombination. Further insight into the effects of surface stoichiometry

of InP/ZnSe core/shell QDs was gained from analogous shelling experiments starting with purified Zn-treated InP QDs, which exhibited no notable differences from starting with In-rich InP QDs in the final PL traces, suggesting the role of Zn in the QD core in the final heterostructures is relatively insignificant compared to the immediate interface the core surface forms with the shell layer. The dynamics in all of these systems were found to be remarkably similar, and low temperature PL data supports the prevalence of trap-mediated non-radiative recombination process. The decreased PL QYs also suggest the presence of a population of dark, non-emissive QDs in the ensemble bearing a shifted interface stoichiometry. Density functional theory (DFT) results indicate that modification of the stoichiometric composition at the core/shell interface can lead to the appearance of shallow hole traps dependent on the identity of the anion. These results highlight the role of the atomic composition of the QD core/shell interface and motivates further exploration of complex material systems fabricated through atomistic reaction chemistry.

2.2 Results and Discussion

2.2.1 *Anion-rich InP core QDs*

First, In-rich, carboxylate-capped InP core QDs were synthesized from atomically precise $In_{37}P_{20}(O_2R)_{51}$ (R = $C_{18}H_{33}$; oleate) clusters and purified to make a stock solution with a known In concentration. These InP cores were dried and redissolved in trioctylamine. Trioctylamine has recently gained traction in the synthesis of highly emissive InP-based quantum dots for its high boiling point (365-367 °C) and ease of removal with alcohol-based anti-solvents.[5,8] In this reaction, it serves a double duty of maintaining the colloidal stability of the quantum dots upon surface treatment while circumventing surface etching that is observed with primary amines (**Figure 2.1**).

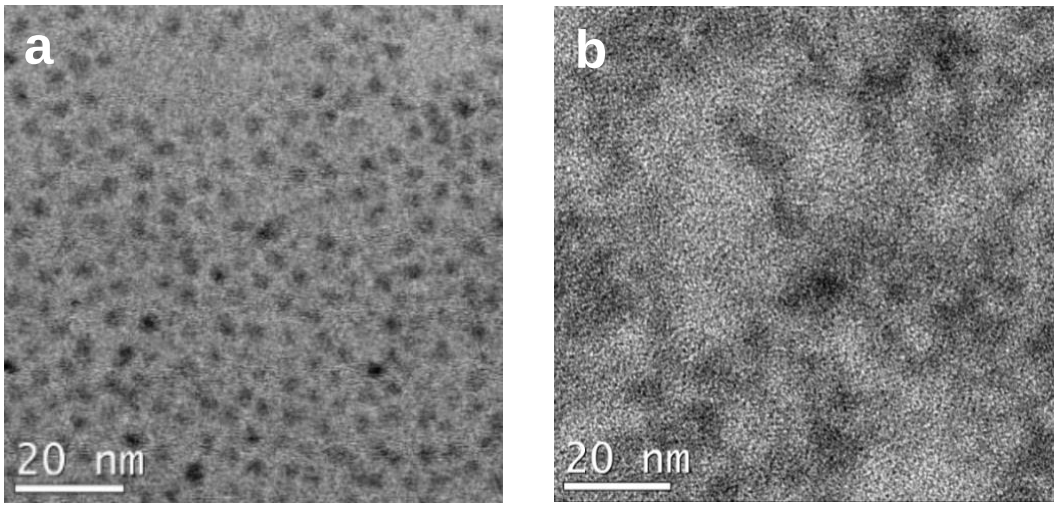

Figure 2.1. TEM images of InP QDs obtained after reacting with 0.5 eq of $P(SiMe_3)_3$ to In a) with and b) without trioctylamine as the coordinating solvent.

Reactive trimethylsilyl ($SiMe_3$, TMS) reagents containing the desired pnictide (P, As) or chalcogenide (S, Se) anion was suspended in trioctylamine. Half an equivalent of anion relative to In was used to yield InP cores with a maximally modified surface stoichiometry (**Table 2.1**). The addition of $P(SiMe_3)_3$ yielded particles that were still In-rich, but had a shifted stoichiometry of 1:0.8 In to P ratio, a 33% increase from the starting 1:0.6 ratio of InP QDs. An upper limit of 1:1.4 for the In:P ratio for a P-rich InP core that originally has a 3.1 nm diameter was extrapolated from QD modelling by Kulik et al.[34] by adding an equivalent anion excess relative to the number of excess In ions (calculations shown in **2.4.8**). For TMS arsenide, sulfide, and selenide, the surface reaction resulted in nanocrystals that exhibited a decrease in P content relative to In, while the added anions were present at a ratio that is almost equivalent to In, and an overall cation to anion ratio of 1:1.3 to 1:1.4.

Table 2.1. ICP-OES results showing In:P:E (E = As, S, Se) ratio of as-synthesized and surface anion-treated InP QDs normalized to In.

	In	P	As	S	Se	In:anion
InP	1	0.6				1:0.6
InP+P	1	0.8				1:0.8
InP+As	1	0.5	0.9			1:1.4
InP+S	1	0.4		0.9		1:1.3
InP+Se	1	0.4			0.9	1:1.3

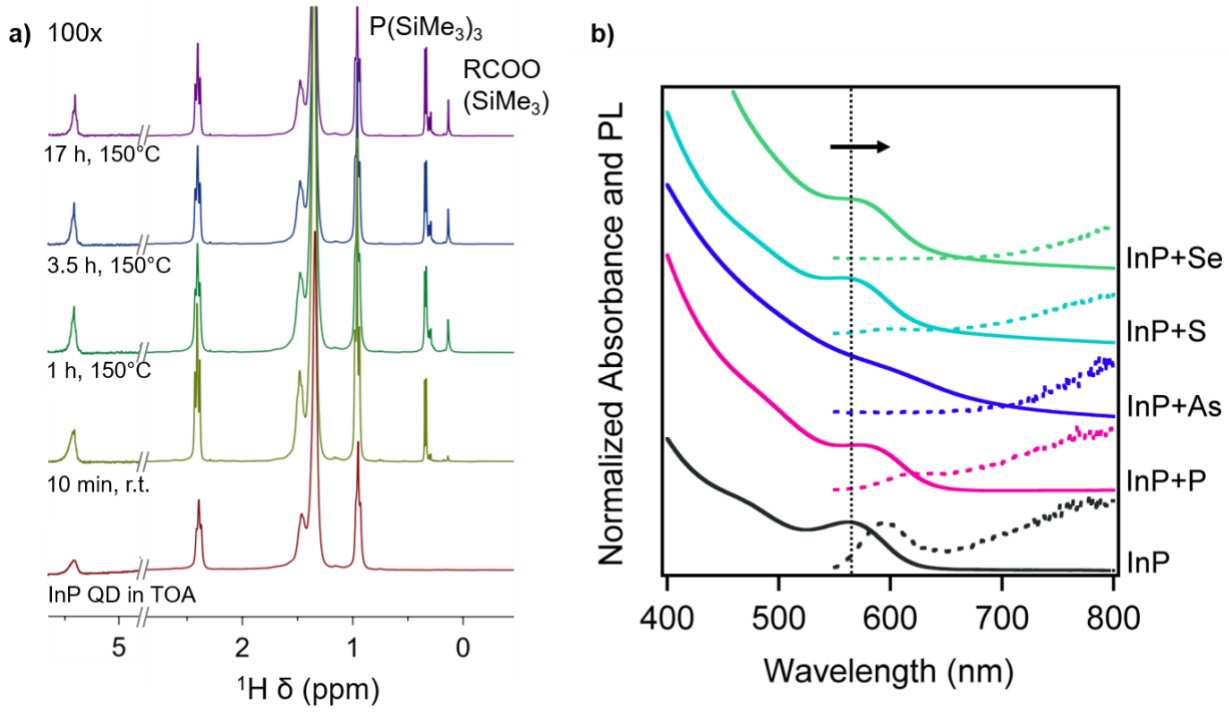

Figure 2.2. InP QD surface treatment with TMS anion reagents. a) ^{1}H NMR spectra showing the evolution of the reaction of carboxylate-capped InP QD with $P(SiMe_3)_3$ obtained (300 MHz, C_6D_6, 298 K, delay time of 20s). The oleate peak centered around 5.5 ppm was amplified by 100x for visibility. b) UV-Vis (solid) and PL (dotted) spectra of native (black), P (pink), As (navy), S (teal),

and Se-treated (green) InP QDs. The vertical dotted line indicates the absorbance max of native InP QD to guide the eye for redshifted absorbance of anion-treated InP QDs.

Using ^{1}H NMR spectroscopy, the reaction at the InP surface was further probed (**Figure 2.2a**). As-synthesized InP QDs can most simply be described as a stoichiometric core and an In-rich surface, capped by long chain carboxylate as the native ligand that is available for surface-limited reaction with the TMS reagent (**Figure 2.3**). In this set-up, the reaction is expected to stop when all of the surface carboxylates (i.e., possible reaction sites) are consumed, eliminating further formation of TMS ester that drives the reaction forward. A stock of InP QDs was further purified by gel-permeation chromatography (x2) to ensure the removal of any excess ligands. The presence of a broad peak (δ=5.6~6.0 ppm) indicating bound oleate was confirmed. This peak shifts to approximately 5.3-5.6 ppm in the presence of trioctylamine. The reaction of purified InP QDs with $P(SiMe_3)_3$ shows growth of TMS ester over the course of the reaction with a concurrent decrease of the phosphine precursor peak, demonstrating that the reaction is occurring between surface bound In carboxylate and $P(SiMe_3)_3$. Additionally, $HP(SiMe_3)_2$ is a known protonolysis product of $P(SiMe_3)_3$ and has been previously reported to be involved in competing precursor conversion pathways in the growth of InP quantum dots.[35] Even when all excess acids are removed from the InP QDs during purification, carboxylic acids are able to remain bound to the surface through L-type coordination as has been evidenced by a detailed NMR studies.[36,37] While the reaction hardly proceeds at room temperature, after one hour at 150 °C, the reaction is mostly complete. The reaction of surface carboxylates and TMS phosphine proceeds and halts before all of the phosphine precursor is consumed, confirming that the reaction of $P(SiMe_3)_3$ remains limited to the QD surface. The reaction yield of TMS ester is approximately 40%, while 45% of the $P(SiMe_3)_3$ remains unreacted, which is in good agreement with the ICP-OES results. Additional evidence for

the removal of the native carboxylate ligands is the evolution of a multimodal resonance that includes a sharp component in the alkene region as the ligand becomes unbound from the nanocrystal surface and forms TMS ester. Similarly, the reaction of purified InP QDs with $Se(SiMe_3)_2$ was monitored by ^1H NMR spectroscopy. The conversion yield of TMS selenide was calculated to be 65%, which is significantly higher than that of $P(SiMe_3)_3$ and is consistent with the high ratio of Se incorporated in the surface-modified InP QDs from the ICP results (**Table 2.1**).

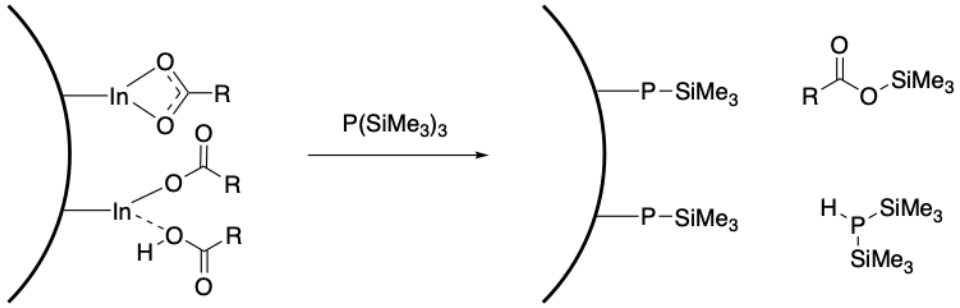

Figure 2.3. Proposed surface reactions between carboxylate/carboxylic acid-capped InP QDs and $P(SiMe_3)_3$.

The observed optical properties from UV-vis and PL spectroscopy reveal a redshift by 17 nm with the addition of $P(SiMe_3)_3$ (**Figure 2.2b**), which can be attributed to the growth of the InP core as previously reported in the literature.[9] The excitonic PL intensity was diminished without significantly perturbing the broad, redshifted trap PL. This characteristic trap PL feature of InP QDs has previously been ascribed to the emission from hole trap states arising from surface P dangling bonds.[15] The addition of $As(SiMe_3)_3$ to the InP core resulted in a similar redshifted absorbance and quenching of excitonic PL while trap PL persisted, although the absorbance peak appeared qualitatively much less defined. This broadened absorbance can be attributed to alloying of the phosphorus and arsenic anions and reflects the ease of arsenic incorporation in the InP core QD as has been previously reported.[38]

The addition of bis(trimethylsilyl) sulfide (or selenide) afforded S- (or Se-) treated, anion-rich InP cores. The formation of InP cores with these chalcogenides coating the surface is of interest as they are commonly used as a component of the wide band gap shell material, including Zn and Cd chalcogenides. Both S- and Se-treated InP cores exhibited a redshift in the absorbance, while the excitonic PL was significantly diminished (**Figure 2.2b**). The broad, redshifted trap PL persisted for both, remaining as a notable feature of these core QDs with anion-rich surfaces.

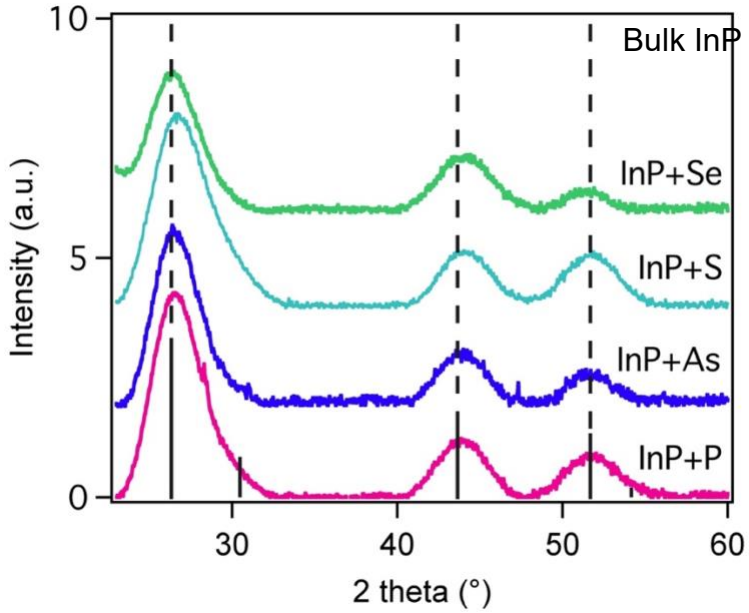

Figure 2.4. XRD pattern of surface-treated InP core QDs.

Structural characterization of the surface-modified InP cores by powder X-ray diffraction (XRD, **Figure 2.4**) confirms that these core QDs retain the zinc blende InP structure with no observable change in FWHM. It is worth noting the (111) plane of the S-treated core shifts to higher 2θ by 0.4° suggestive of a contracted lattice due to the surface strain by the smaller S atoms. TEM (transmission electron microscopy) images corroborate no notable changes in the size of the nanocrystals from the original 3.1 nm diameter (**Figure 2.5**).

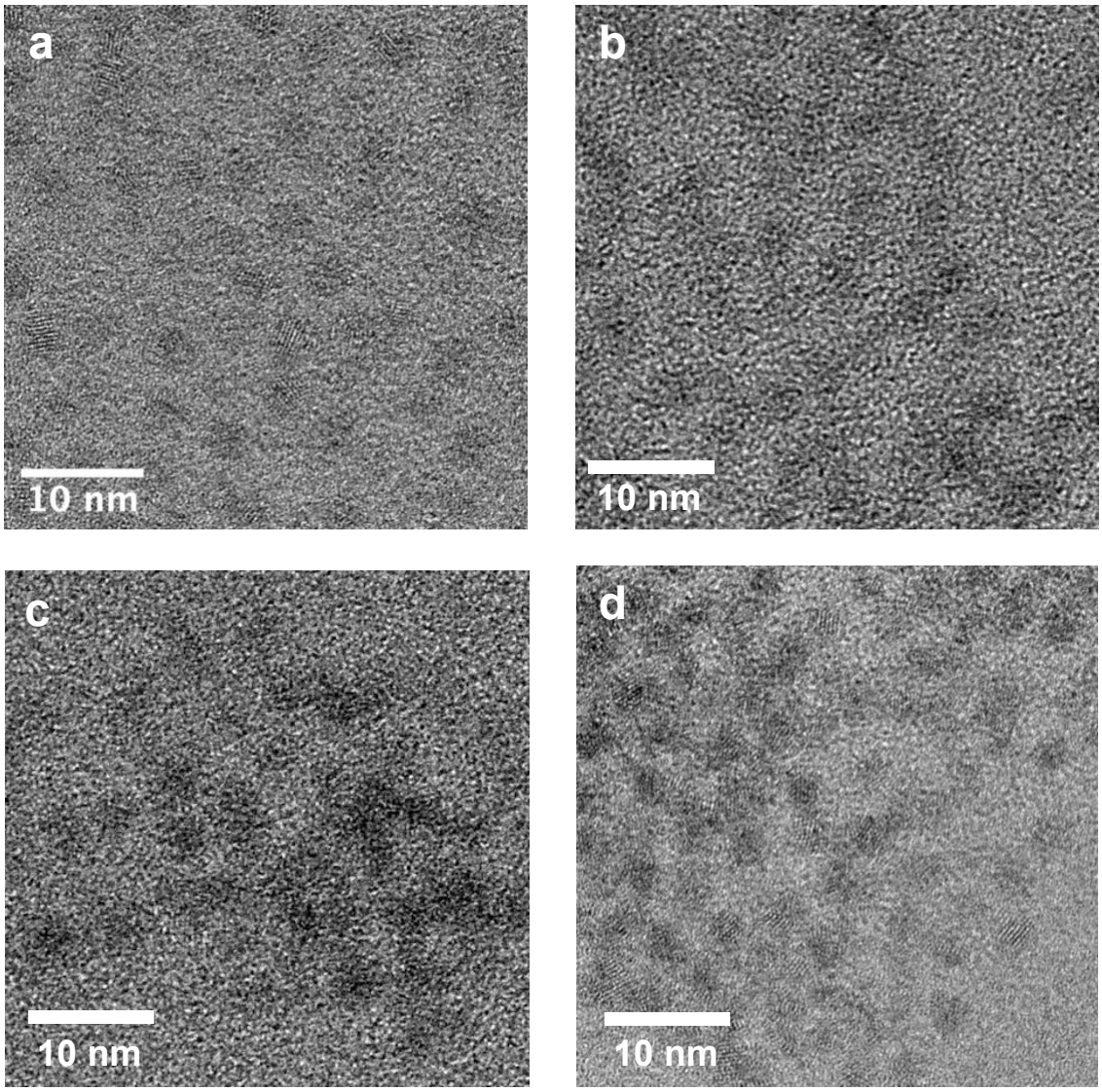

Figure 2.5. TEM images of surface-treated InP core QDs reacted with a) P; 3.1 nm +/- 0.3 nm, b) As; 3.0 nm +/- 0.3 nm, c) S; 3.2 nm +/- 0.3 nm, and d) Se; 3.0 nm +/- 0.4 nm. Size analysis was performed on ImageJ software with which >300 QDs were measured per sample. Aggregates were observed among individual QDs for those treated with As, S, and Se. This is likely due to the removal of a large fraction of the native carboxylate ligands from the QD core, with colloidal stability relying on relatively weak L-type trioctylamine coordination.

With the knowledge that the surface anion treatment did not change the size, morphology, or the crystal structure of the InP QDs to any significant degree, the observation of the redshift in the absorbance can be attributed to a change in the electronic structure as a result of the shifted stoichiometry. More specifically, the redshift suggests a quasi-Type II band structure, where delocalization of the charge carrier wavefunction results in relatively softer confinement of the exciton in the core. This is consistent with theoretical investigations by Califano et al.,[32] who concluded that P-rich InP QDs have delocalized electrons and localized holes, resulting in an overall decreased wavefunction overlap. Similar phenomena have been reported by Brutchey et al. where the observed redshifts with chalcogenol ligands installed on the surface of CdSe QDs were attributed to relaxed quantum confinement resulting from the coupling between the HOMO of the chalcogenol and the QD hole wavefunction.[39] It was proposed that chalcogenol ligands attract the hole and localize hole density at the surface. Where this observation becomes more nuanced is that such separation of the electron and hole simultaneously results in a reduction of the Coulombic interaction. The decreased exciton binding energy is expected to cause a blueshift. Recently, the effect of accounting for this Coulombic interaction between the electron and the hole to calculate the band gaps of II-VI QD heterostructures was demonstrated using Poisson's equation in an effective mass approximation.[40] With this, we note that III-V semiconductor materials typically exhibit small effective masses, which means that the Coulombic energy accounts for only a small fraction of the band gap energy.[41] Because spatial separation of the exciton would result in a reduction of exciton wavefunction overlap, the quenching of excitonic PL is expected, and we propose this as a reasonable explanation for the PL quenching we observe in the anion-treated InP cores.

2.2.2 *Anion-rich interface in core/shell QDs*

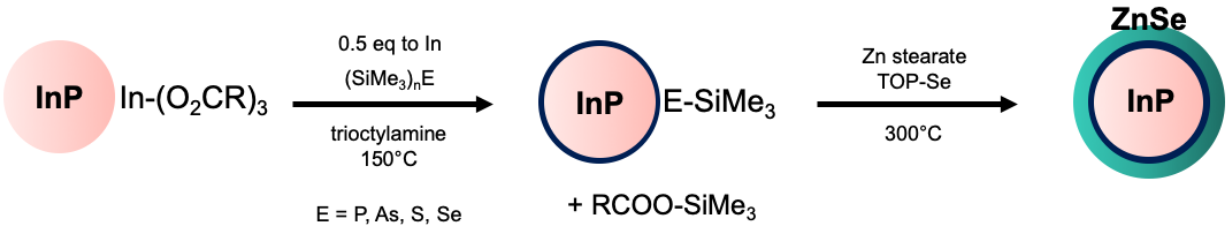

Figure 2.6. Shelling scheme of interface controlled InP/ZnSe QDs.

In situ shelling of the anion-rich InP QDs was performed to investigate the effects of the modified interfaces on the luminescence and photophysical properties of the core/shell QDs. A wider band gap ZnSe shell for type-I band alignment (confinement of exciton to the core) with InP was chosen to standardize the shelling procedure, for structural simplicity, and a better lattice match with the InP core compared to ZnS (3.4% vs. 7.7%). Shelling was carried out (**Figure 2.6)** by first taking purified InP QDs dissolved in trioctylamine and slowly injecting 0.5 eq. (vs. In) of the reactive silyl reagent containing P, As, Se, or S at 150 °C for an hour. A ZnSe shell was grown on the surface-modified cores using temporally separated slow injection of Zn and Se precursors, each at 220 °C and 300 °C, respectively. The excitonic PL was recovered for all samples upon the addition of Zn and continued to increase in intensity throughout the growth of the ZnSe shell. The observation of increased PL intensity upon the addition of Zn can be attributed to the passivation of the surface anion sites that serve as hole traps as has been seen previously in both II-VI and III-V systems.[14,42]

The resultant InP/ZnSe core/shell QDs exhibited varying PL efficiencies and a range of absorption and PL wavelengths. The highest PL QY of 41% straight out of synthesis was achieved by the control sample where no interfacial anion was added prior to shelling. The PL QY was improved to 75% upon initial purification, likely due to removal of a population of unshelled InP

QDs. Initial purification involved centrifuging the concentrated sample from vacuum distillation diluted with toluene to remove the insoluble fraction. The supernatant was then flushed with acetonitrile and was centrifuged once more to remove any remaining reaction byproducts. This procedure effectively separates the aggregated, oxidized, and otherwise scattering materials which has the net effect of improving the ensemble quality and the quantum yield. This PL QY was reduced to 15% upon size-selective precipitation that narrowed the emission linewidth. While repeated centrifugation-precipitation-redissolution cycles can strip off the surface ligands and lower the PL QY, size-selective precipitation was necessary to proceed with further characterization of these samples to probe the impact of interfacial stoichiometry in a homogeneous population. The change in emission linewidth following size-selective precipitation was most pronounced in the control sample, suggesting heterogeneous shell growth that results in the broadening of the linewidth. The normalized PL spectra of all samples before and after size-selective precipitation are shown in **Figure 2.7a**. Notably, the PL linewidth and the line shape showed minimal change after size-selective precipitation for the As, S, and Se-rich interface core/shell QDs, suggesting a more controlled and uniform growth upon synthesis compared to the traditional shelling approach.

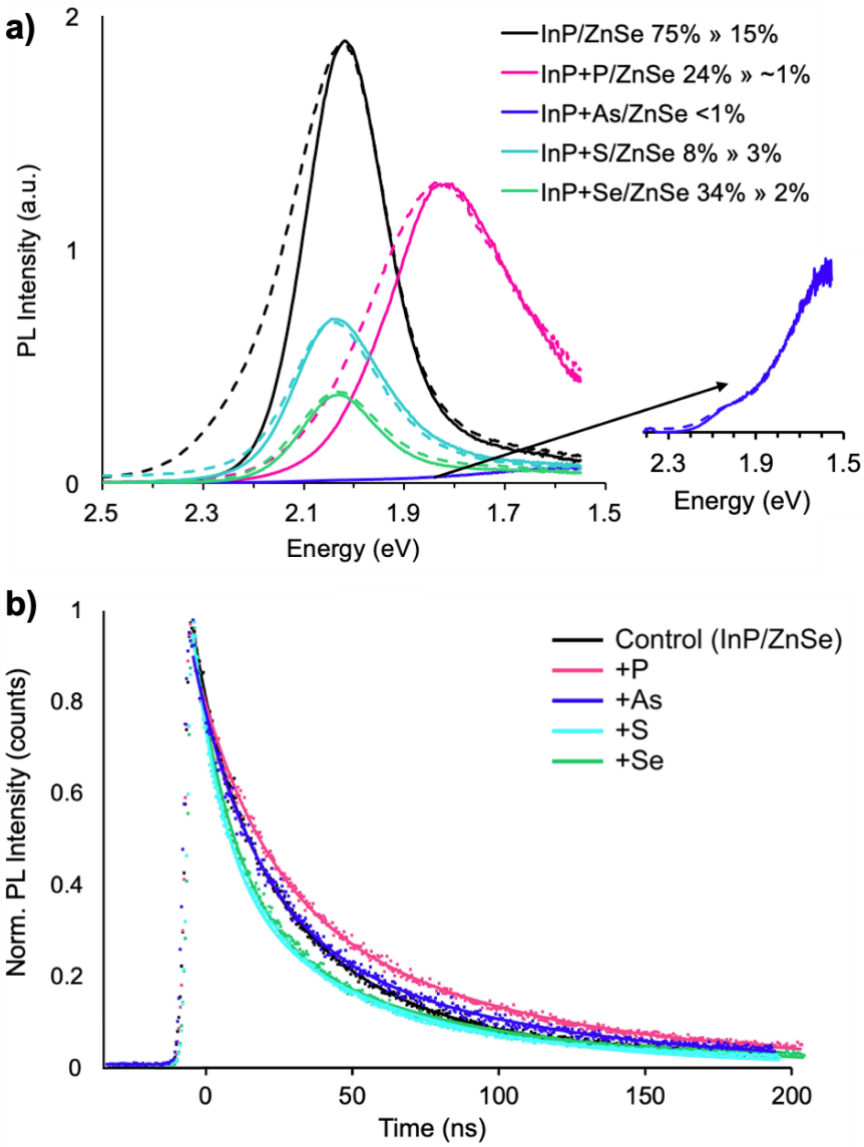

Figure 2.7. a) PL spectra of InP/ZnSe QDs with anion-rich interface before size-selective precipitation (dotted, normalized to solid trace) and after (solid) size-selective precipitation. Quantum yields before and after size-selective precipitation are noted in the legend. InP+P/ZnSe sample quickly oxidized upon exposure to air precluding accurate measurement. b) Excitonic PL decay dynamics of InP/ZnSe QDs with modulated interfaces measured at room temperature. Transient PL spectra were obtained by integrating streak camera data over 200 ns between 2.14-1.97 eV (black, navy, teal, green traces) or 1.91-1.77 eV (pink trace).

Further insight was gained from elemental and structural analysis of the shelled particles purified by size-selective precipitation. Elemental analysis by ICP-OES indicated retention of the anions that were post-synthetically added to the purified InP QD surface (**Table 2.2**). The P-treated interface resulted in an In:P ratio of 1:1. It is evident from the atomic ratios that the anions employed in core surface treatment were incorporated in the final core/shell structure, with the ratio of the shelling layer representative of a 1-2 monolayer shell. The expected core/shell structure is corroborated by powder XRD (**Figure 2.8a**), where the zinc blende InP/ZnSe QD structure is observed across all samples, with the InP reflections exhibiting shifts toward bulk ZnSe, indicating successful shelling and reliably homogeneous populations following size-selective precipitation. For the sample with a P-rich interface, the asymmetry of the peaks at 43.6° (220) and 51.7° (311) may be attributed to stacking disorder within the nanocrystal.[43,44] We propose that inhomogeneous strain due to uneven compositional distribution or alloying can give rise to defect-related nonradiative recombination. TEM analysis shows nanocrystals of sizes between 7.0-7.5 nm in diameter and highly crystalline lattices despite their irregular morphology (**Figure 2.8b-f**).

Table 2.2. The atomic compositions of InP/ZnSe QDs with anion-modulated interfaces obtained from ICP-OES. The molar ratios are normalized to moles of In.

	In	**P**	**As**	**S**	**Se**	**Zn**
InP/ZnSe	1.0	0.3			6.8	7.1
InP+P/ZnSe	1.0	1.0			5.2	5.8
InP+As/ZnSe	1.0	0.3	2.7		5.6	5.0
InP+S/ZnSe	1.0	0.5		1.0	3.8	4.6
InP+Se/ZnSe	1.0	0.4			9.1	8.6

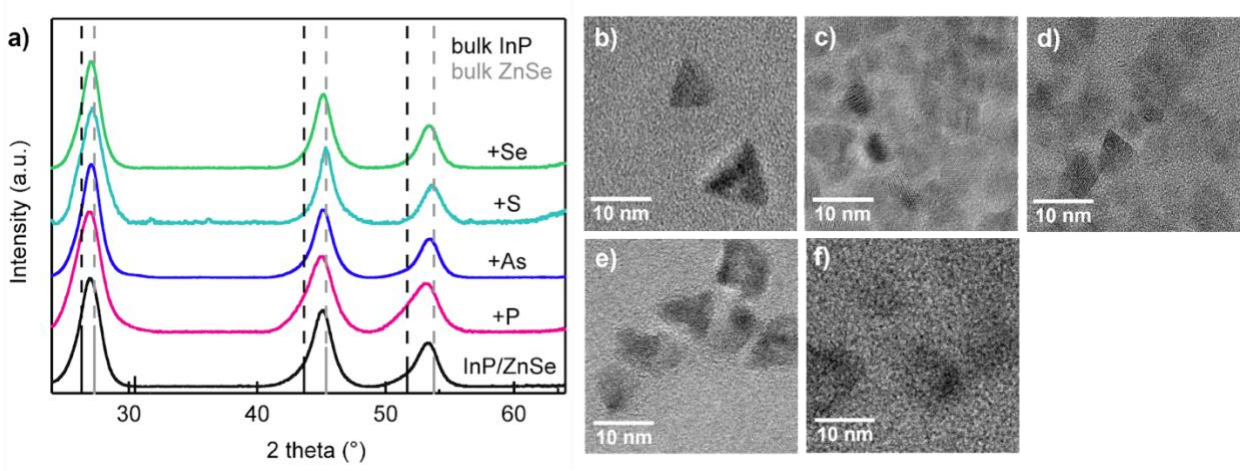

Figure 2.8. a) Powder XRD patterns of InP/ZnSe QDs with anion-rich interface compared with traditional InP/ZnSe QDs exhibiting a shift from InP (PDF #01-070-2513) toward ZnSe (PDF #04-001-6858), and b-f) TEM images of InP/ZnSe control, P, As, S, and Se-interface core/shell QDs.

These samples were further probed by time-resolved photoluminescence spectroscopy (TR PL) to study the effects of the modified interfaces on the charge carrier dynamics (**Figure 2.7b, Table 2.3**). The PL decay data were collected over a 200 ns window and were each fit with biexponential functions. Notably, the samples with S- and Se-rich interfaces showed a decreased lifetime in the faster component when compared to control InP/ZnSe QDs. The As-rich interface sample exhibited very similar decay dynamics to the control InP/ZnSe QDs, while the P-rich interface sample showed a relatively larger magnitude of the slower time component, increasing the weighted lifetime. The decreased lifetime of the faster component observed for the chalcogenide-rich interfaces may suggest the emergence of new processes such as trapping at chalcogen-derived defect states. Lower PL QYs for samples with modified interfaces support the creation of new pathways that facilitate non-radiative recombination. While steady-state and time-resolved PL offer insight that a shifted atomic composition at the core/shell interface, even with submonolayer coverage, can alter the optical and photophysical properties in the ns timescale, the

differences in the weighted lifetimes are small overall and show no change in the longer timescale. PL quenching evident in the overall low QY of the samples suggests behavior of the charge carriers not reflected in the observed lifetime and leads us to speculate that the ensembles contain populations of QDs that are non-luminescent. The creation of a permanently dark fraction upon shifting the stoichiometry at the core/shell interface is considered, given that such a shift could give rise to negatively charged QDs upon interstitial defect incorporation into the nanocrystal lattice. In doped QDs, the PL has been shown to be quenched by nonradiative Auger processes that are a few orders of magnitude faster than radiative recombination.[45,46] Given that the overall ensemble quantum yield is determined more dominantly by the dark fraction, this could also explain the low QY of the anion-treated samples.[47] In light of recent NMR studies of Cd-treated InP QDs,[48] where the presence of a mixture of surface species including surface phosphates was confirmed, it seems that this approach to surface modification on an already defective core further reinforces the defect-ridden interface, resulting in poor optical properties. Removal of oxidized surface defects with HF and subsequent addition of anions was attempted and resulted in similar final PL QYs (**Figure 2.9**), necessitating further exploration of the surface chemistry needed to form an ideal interface.

Table 2.3. Parameters fit to biexponential function for excitonic PL decay dynamics measured at room temperature.

Sample	$\mathbf{A_1}$	$\boldsymbol{\tau_1}$ **(ns)**	$\mathbf{A_2}$	$\boldsymbol{\tau_2}$ **(ns)**	$\boldsymbol{\tau_{weighted}}$ **(ns)**
InP/ZnSe	0.61	19	0.35	67	37
InP+P/ZnSe	0.48	20	0.44	78	48
InP+As/ZnSe	0.55	19	0.36	76	38
InP+S/ZnSe	0.56	10	0.41	55	28
InP+Se/ZnSe	0.63	13	0.33	68	32

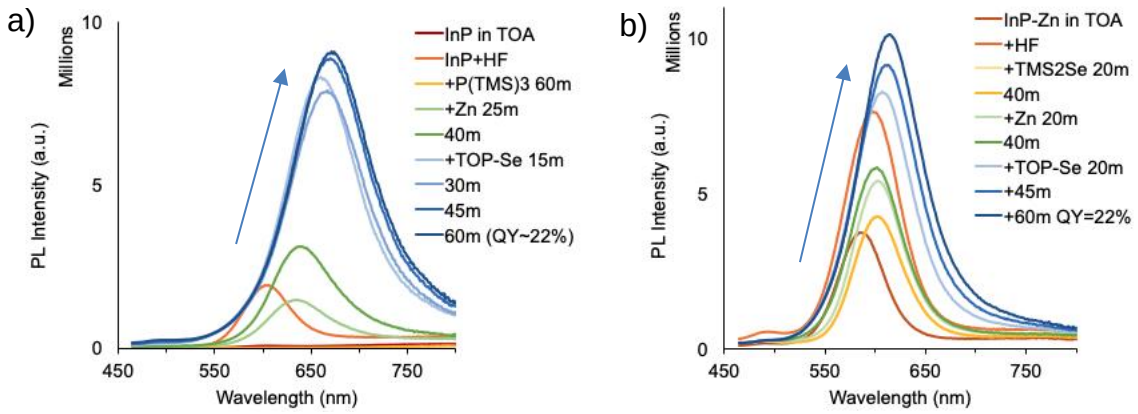

Figure 2.9. PL spectra of HF treated InP cores that were subsequently treated with a) $P(TMS)_3$ or b) $Se(TMS)_2$ prior to ZnSe shelling. The effects of removing the oxidative defects by HF prior to surface anion deposition did not result in improvement of the final PL QY.

To better understand the nature of the trap states and the charge carrier dynamics, we measured the PL spectra at low temperature (77 K) to compare to room temperature PL (**Figure 2.10**). Generally, it is evident that when the temperature is decreased, the excitonic PL blueshifts as expected from the Varshni relation.[49] For the samples with modulated interface compositions, the overall PL intensities tend to increase. Qualitatively, the relative increase of trap PL is higher than that of excitonic PL. This suggests a thermally mediated de-trapping mechanism at room temperature, which has been previously reported with InP cores with implication for defects from dangling bonds either from In or P surface atoms.[15] The anion-derived trap PL we observed in the surface modified InP cores is suppressed at room temperature upon shelling, but these electronic defects are evident in the low temperature spectra.

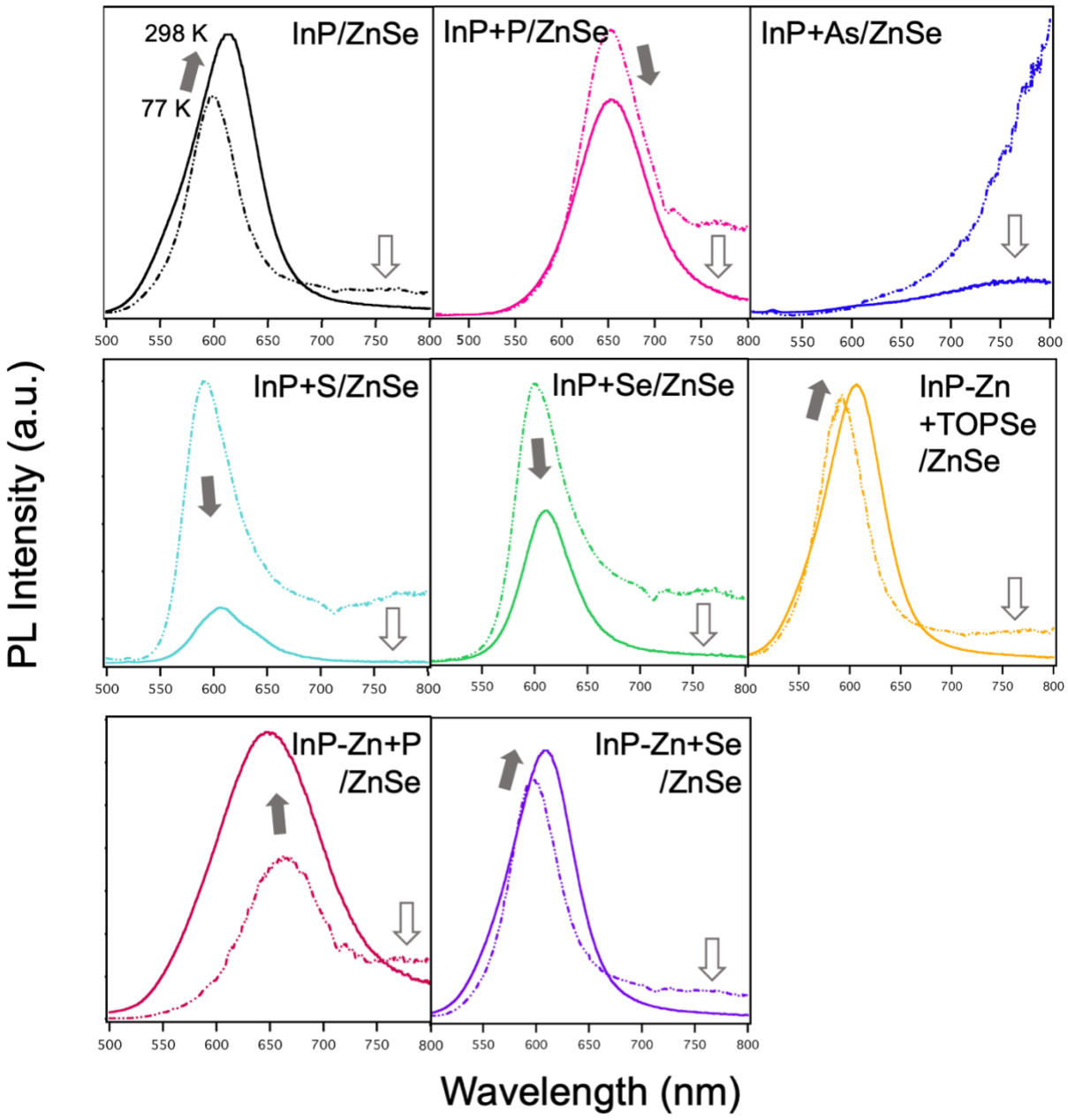

Figure 2.10. Low temperature PL of all shelled samples. The arrows indicate the change in intensity (grey, excitonic; white, trap) as the temperature increases from 77 K to 298 K.

2.2.3 *Tuning surface anion composition of optically bright, Zn-rich InP cores*

We extended the sample set to include Zn-rich InP cores exhibiting 20% PL QY as the starting material for interface tuning and shelling. Zn-rich InP cores are best described as stoichiometric InP cores with Zn carboxylates as surface ligands. In this set of experiments, TMS phosphine and selenide were specifically chosen to modulate the interfacial stoichiometry. Additionally, as an analogue to $Se(SiMe_3)_2$, TOP-Se was used for comparison. Upon introduction of the anion precursor, the absorption peak was redshifted across all samples accompanied by an increase in the PL intensity. With each subsequent addition of the shelling precursors, the absorption and PL maxima continued to redshift. The final absorption and PL wavelengths for these interface modified InP/ZnSe QDs were strikingly similar between In-rich and Zn-rich InP cores (**Figure 2.11a**). P-treated InP-Zn core QDs displayed the largest redshift overall, while surface treatment with $Se(SiMe_3)_2$ or TOP-Se resulted in PL maxima similar to what is observed for InP/ZnSe without surface anion treatment, with the overall PL profiles nearly overlapping. Starting with bright core QDs achieved with Zn treatment led to higher PL QYs in the final core/shell QDs overall and less loss of PL QY upon size-selective precipitation, suggesting that the emissive quality of the starting core material is critical to the final optical properties and photostability.

Elemental analysis by ICP-OES demonstrates that both P and Se introduced by the reactive silyl precursors were successfully incorporated into the final core/shell QDs (**Table 2.4**). In both cases, an overall anion-rich stoichiometry was obtained. Interestingly, there was a difference in the atomic ratios between the $Se(SiMe_3)_2$ and TOP-Se treated samples resulting in a reversed cation to anion ratio. This indicates that the reactive silyl precursor that targets direct reaction with surface carboxylates renders a different surface chemistry and atomic composition that persists

after the shell growth. The expected zinc blende structure of the final core/shell QDs and the size and morphology of the particles were corroborated by the powder XRD patterns and TEM.

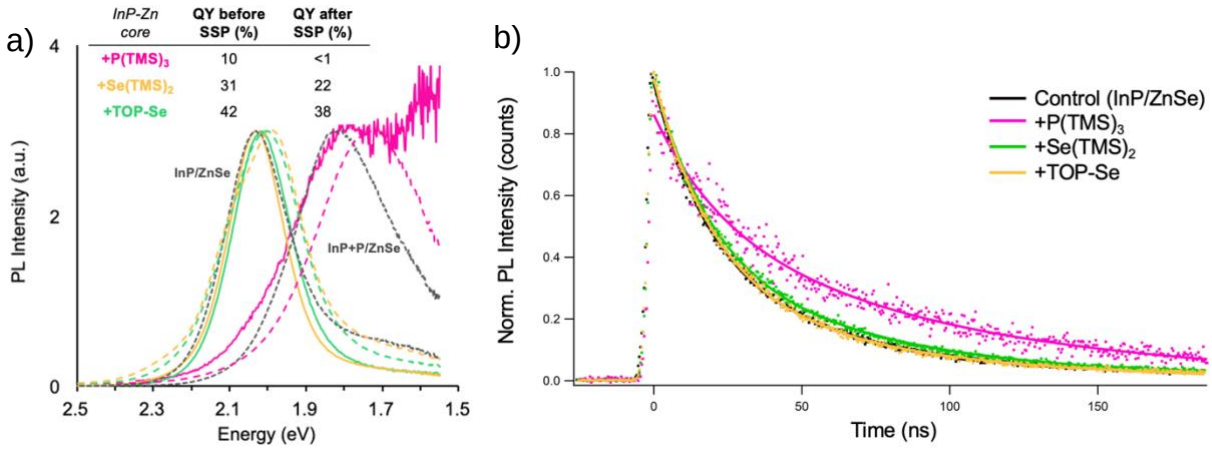

Figure 2.11. InP/ZnSe QDs synthesized with Zn-rich InP cores and modulated interfacial composition. a) PL spectra of anion-rich interface after size-selective precipitation made with Zn-rich InP core and with In-rich InP core (dotted grey, normalized to solid traces). Colored dashed traces indicate PL spectra prior to size-selective precipitation. Quantum yields before and after size-selective precipitation are noted in table inset. b) Excitonic PL decay dynamics of InP/ZnSe QDs with modulated interfaces measured at room temperature. Transient PL spectra were obtained by integrating streak camera data over 200 ns between 2.14-1.97 eV (black, green, and yellow traces) or 1.84-1.71 eV (pink trace).

Table 2.4. The atomic composition of InP/ZnSe QDs synthesized with Zn-rich InP cores and anion-modulated interfaces obtained from ICP-OES. The molar ratios are normalized to moles of In.

	In	**P**	**Zn**	**Se**
InP-Zn +$P(SiMe_3)_3$/ZnSe	1.0	1.1	6.8	5.7
InP-Zn +$Se(SiMe_3)_2$/ZnSe	1.0	0.4	5.3	6.2
InP-Zn +TOP-Se/ZnSe	1.0	0.5	6.1	5.8

Table 2.5. Parameters fit to biexponential function for excitonic PL decay dynamics measured at room temperature.

Sample	A_1	τ_1 (ns)	A_2	τ_2 (ns)	$\tau_{weighted}$ (ns)
InP/ZnSe	0.61	19	0.35	67	37
InP-Zn +$P(SiMe_3)_3$/ZnSe	0.33	22	0.53	92	65
InP-Zn +$Se(SiMe_3)_2$/ZnSe	0.57	19	0.41	69	40
InP-Zn +TOP-Se/ZnSe	0.67	20	0.31	71	36

The excitonic PL decay dynamics of the InP/ZnSe QDs made from Zn-treated InP cores were investigated (**Figure 2.11b, Table 2.5**). Compared to the control InP/ZnSe sample, P-rich interface core/shell QDs showed a reduction in the amplitude of the short time component and a relative increase of the slower time component with an extended lifetime, similar to the decay dynamics when the In-rich InP core was shelled. The samples modified with Se precursors, however, exhibited very similar excitonic PL dynamics where the decay curve overlaps with that of the control InP/ZnSe sample. Here, the shift in stoichiometry of the cation to anion ratio induced by the different Se precursors evident in ICP-OES results does not have any observable changes in this timescale, suggesting the loss in PL QY can again be attributed to hole-associated trapping on a faster timescale and the creation of non-radiative decay pathways and/or dark fractions. This also suggests that the immediate interface formed with the InP core (i.e., with Zn carboxylate) is more influential to the photophysics of heterostructure QDs. The dynamics in all of these systems remain remarkably similar. The low temperature PL of these samples (**Figure 2.10**) shows a notably different trend from the samples made from In-rich InP cores. At lower temperature, the excitonic PL intensity decreased while the trap PL intensity increased. This is consistent with the observation of the InP/ZnSe control sample, supporting the importance of immediate interfacial structure (surface anion vs cation) at the core/shell interface. Interestingly, InP-Zn+P/ZnSe sample

showed a redshift upon lowering the temperature, which to our knowledge has not previously been observed in shelled InP literature and is a surprising result given the Varshni relation. While less common, an increase in band gap with increasing temperature has been previously observed for Pb chalcogenide QDs and has been attributed to an unconventional trapped exciton state[50] or exciton dark-bright state splitting.[51]

2.2.4 *Cluster-models of core and core/shell InP QDs*

In order to gain further insight into the electronic structure of the surface modified core and core/shell QDs, we turned to density functional theory. Calculations were conducted using the Gaussian software package (G16.B01)[52] using the Perdew, Burke, and Ernzerhof hybrid functional (PBE0)[53–55]. Quasi-spherical InP QD, $In_{77}P_{77}$ (diameter ~2 nm) was constructed using the bulk zinc blende crystal structure. The pure InP structure conformed to a C_{3v} symmetry before optimization. Core/shell structures were built from the InP core by exchanging surface In with Zn and P with Se to form $In_{x-y}P_{x-y}/Zn_ySe_y$ (d ~2 nm for $In_{10}P_{10}/Zn_{67}Se_{67}$). In order to generate the anion-rich models ($In_{10}P_{10-y}E_y/Zn_{67}Se_{67}$, E = As, S, and Se), the previously optimized $In_{10}P_{10}/Zn_{67}Se_{67}$ core/shell model had the interfacial P atoms replaced. Surface dangling bonds were terminated using a pseudo-hydrogen capping scheme to compensate surface ions (±1/3 for the non-shelled InP systems) resulting in $(InP)_{77}H_{108}$ structure for the non-shelled system. The calculated band gaps of the $(InP)_{77}H_{108}$ and the $(InP)_{10}/(ZnSe)_{67}H_{108}$ structures were 3.89 eV and 3.77 eV, respectively.

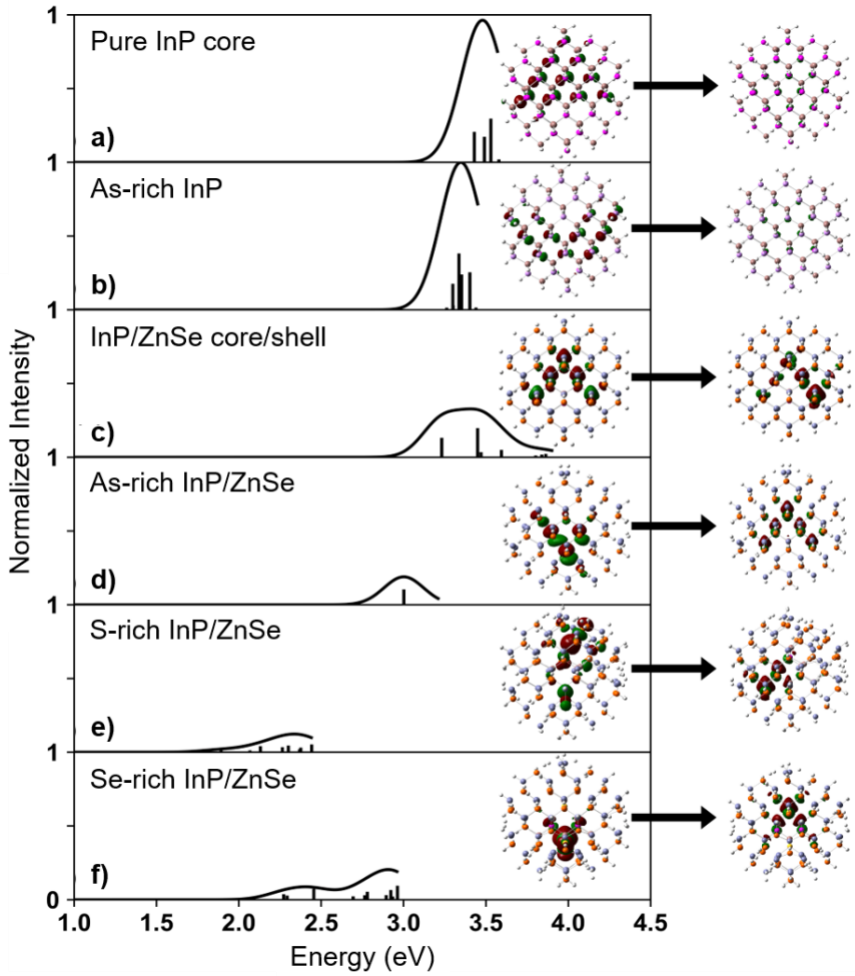

Figure 2.12. The TD-DFT absorption spectra for (a) the stoichiometric $In_{77}P_{77}$ QD, (b) the As-rich $In_{77}P_{23}As_{54}$ QD, (c) the $In_{10}P_{10}/Zn_{67}Se_{67}$ core/shell QD, (d) the As-rich $In_{10}P_3As_7/Zn_{67}Se_{67}$ QD, (e) the S-rich $In_{10}P_4S_6/Zn_{67}Se_{67}$ QD, and (f) the Se-rich $In_{10}P_4Se_6/Zn_{67}Se_{67}$ QD. A smoothing function has been applied to the TD-DFT roots (shown as black vertical bars) of 0.12 eV, and the resulting spectrum shown as the black line. Atoms are represented as balls with the In atoms in brown, the P atoms in pink, the S atoms in yellow, the Se atoms in orange, the As atoms in purple, the Zn atoms in gray, and the pseudo H as white. The leaving and arriving orbitals for the first bright transition ($f > 0.01$) for each system are plotted with an isovalue of 0.02 inset into the spectra.

Table 2.6. The diameters, band gaps, and first bright absorption response (f > 0.01) of the InP cluster models. The MOs contributing to each transition listed are plotted in **Figure 2.14** of main text.

Formula	Diameter (nm)	Band Gap (eV)	Absorption (eV)	Absorption (nm)
$In_{77}P_{77}$	1.96	3.89	3.43	361
$In_{77}P_{23}As_{54}$	2.00	3.73	3.30	376
$In_{10}P_{10}/(ZnSe)_{67}$	1.93	3.77	3.23	384
$In_{10}P_3As_7/(ZnSe)_{67}$	1.93	3.55	3.00	413
$In_{10}P_4S_6/(ZnSe)_{67}$	1.94	2.15	1.89	546
$In_{10}P_4Se_6/(ZnSe)_{67}$	1.91	2.75	2.27	656

Surface modified core structures were constructed by replacing surface P atoms with As atoms resulting in an $In_{77}P_{23}As_{54}$ structure. The addition of the surface As atoms resulted in a decrease in the band gap (by 0.16 eV) in comparison to the $In_{77}P_{77}$ structure (**Figure 2.12, Table 2.6)**. This resulted in a redshift in the TD-DFT absorption spectrum (by 0.13 eV), which is consistent with the experimental data. It is important to note that the models investigated are generally blue shifted in relation to the experimental systems as they are more quantum confined. Looking at the molecular orbitals (MOs) responsible for the transition for the As-rich system (**Figure 2.12, Figure 2.13**), it is worth noting that there is little density at the surface where the replaced anions are located for either the HOMO or the LUMO, which is a possible explanation for why the observed redshift is minimal. In order to examine if additional localization can be achieved by the interfacial anion layer at the core/shell interface, the anion-modified models were shelled with ZnSe.

Upon the addition of ZnSe shell to the InP system (going from $In_{77}P_{77}$ to $In_{10}P_{10}/Zn_{67}Se_{67}$) the band gap for the system decreases (by 0.12 eV), as anticipated due to the ability for the

wavefunction to diffuse into the shell. The addition of the anions to the core/shell structure results in an observable red shift of the TD-DFT absorption spectrum (**Figure 2.12**). This corresponds to a reduction of the band gaps due to the presence of the additional anions observed in all shelled structures (**Figure 2.14, Table 2.6**). Examination of the density of states (DOS) plot for the $In_{10}P_{10}/Zn_{67}Se_{67}$ structure **(Figure 2.14)** shows that the states around the band gap are comprised predominantly of P in the valence band and In in the conduction bands as expected for InP systems. However, due to the presence of the ZnSe shell, there are significant contributions by Se in the valence band and Zn in the conduction band, showing that the wavefunction is able to diffuse into the shell. The addition of As to the core/shell interface gives rise to As contributions in the valence band. These contributions work to reduce the band gap (by 0.22 eV) from the $In_{10}P_{10}/Zn_{67}Se_{67}$ structure. This reduction in the band gap is apparent in the computed TD-DFT absorption spectrum as a redshift (by 0.23 eV) similar to the process noted experimentally.

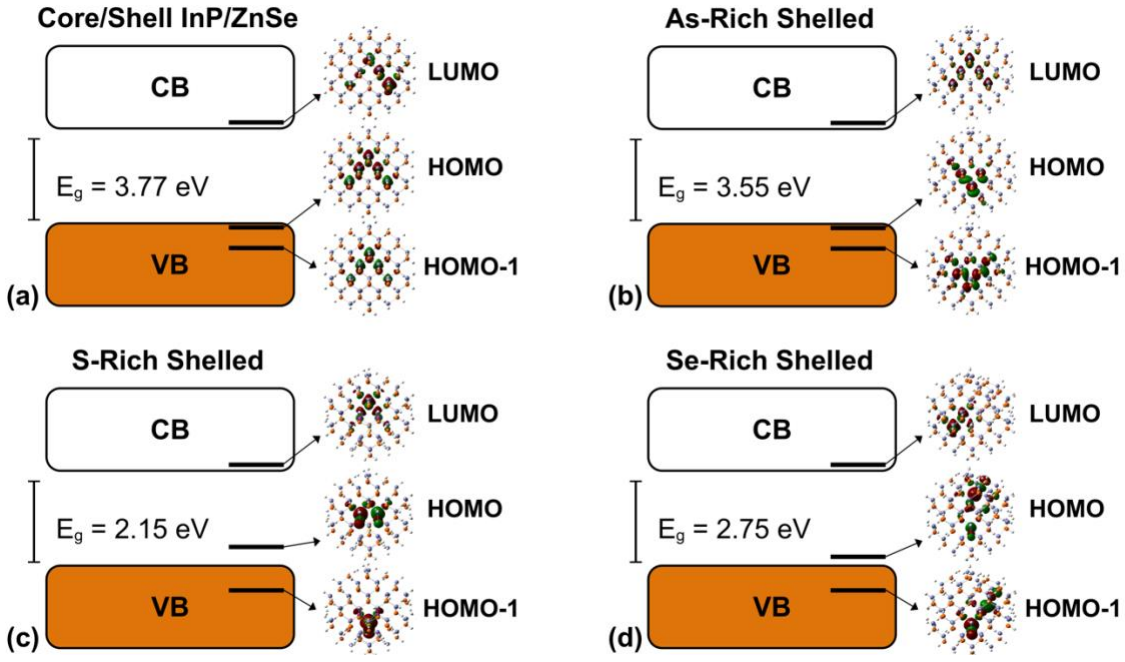

Figure 2.13. Energetic MO diagram (not to scale) for the (a) the $In_{10}P_{10}/Zn_{67}Se_{67}$ core/shell QD, (b) the As-rich $In_{10}P_3As_7/Zn_{67}Se_{67}$ QD, (c) the S-rich $In_{10}P_4S_6/Zn_{67}Se_{67}$ QD, and (d) the Se-rich $In_{10}P_4Se_6/Zn_{67}Se_{67}$ QD. Atoms are represented as balls with the In atoms in brown, the P atoms in pink, the S atoms in yellow, the Se atoms in orange, the As atoms in purple, the Zn atoms in gray, and the pseudo H as white. The frontier MOs are plotted in the same orientation as in Figure 5 of main text with an isovalue of 0.02.

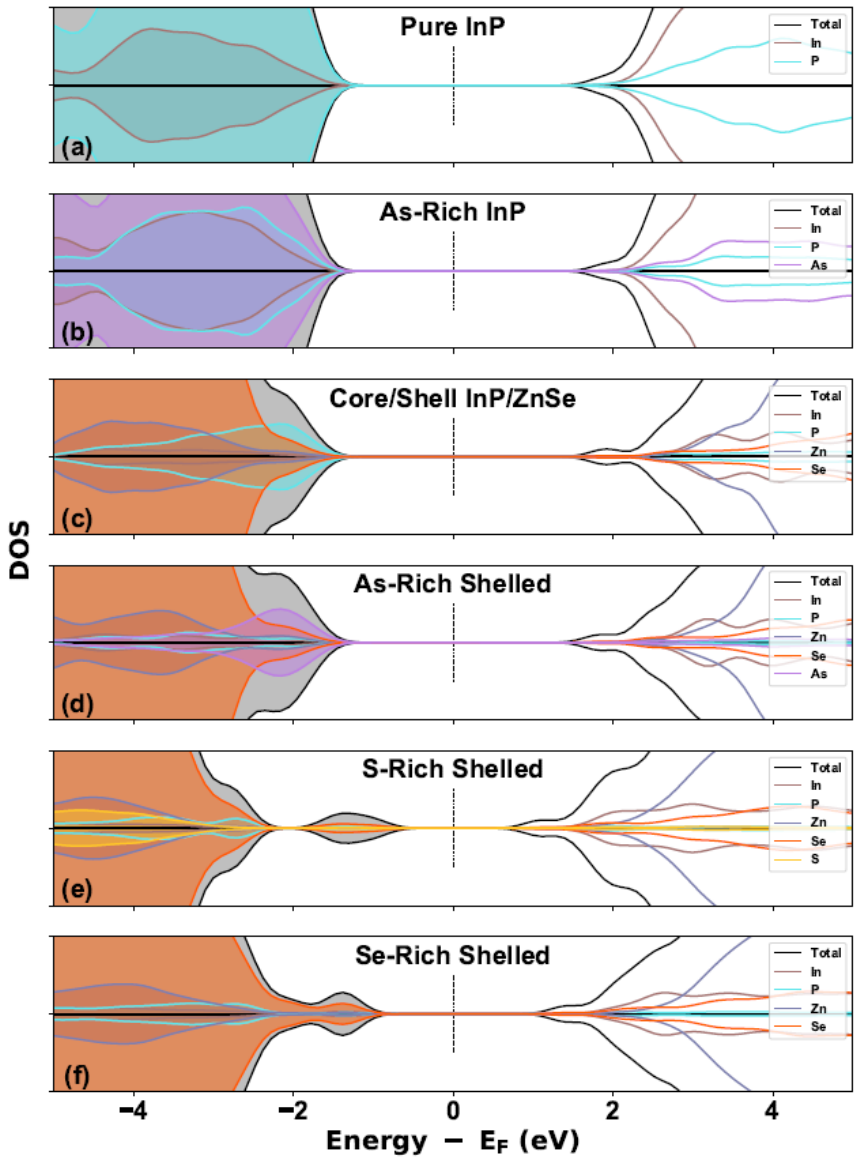

Figure 2.14. The density of states plots for (a) the stoichiometric $In_{77}P_{77}$ QD, (b) the As-rich $In_{77}P_{23}As_{54}$ QD, (c) the $In_{10}P_{10}/Zn_{67}Se_{67}$ core/shell QD, (d) the As-rich $In_{10}P_3As_7/Zn_{67}Se_{67}$ QD, (e) the S-rich $In_{10}P_4S_6/Zn_{67}Se_{67}$ QD, and (f) the Se-rich $In_{10}P_4Se_6/Zn_{67}Se_{67}$ QD. The atomic P-orbital contributions by each atomic species is noted in color as contributing to the total density of states (in black). The DOS plots have had a gaussian smoothing of 0.2 eV applied. Positive and negative values correspond to spin up and down, respectively.

The addition of Se into the interface between the core and shell reduces the band gap even further (by 1.02 eV) from the $In_{10}P_{10}/Zn_{67}Se_{67}$ structure. As shown in **Figure 2.14**, the Se contributes to states that begin to separate from the edge of the valence band and begin to form shallow hole-trap states resulting in the TD-DFT absorption spectrum being significantly redshifted (by 0.96 eV) from the $In_{10}P_{10}/Zn_{67}Se_{67}$ structure. The addition of S in the core/shell interface leads to a similar result, though the shifts are more pronounced (band gap is redshifted by 1.62 eV, absorption is redshifted by 1.34 eV) as the states introduced to the band edge are further separated from the conduction band. It is important to note that similar band-edge states have been noted to form in computational InP cluster models before.[56] In this case, however, these states arose due to the surfaces of the InP models giving rise to spin densities localized to surface metal centers leading to high-spin ground states. To ensure this was not occurring, the energies of several (singlet, S=0, through nonet, S=8/2) were computed (**Figure 2.15**), and it was found that the singlet configuration is the most stable. This is expected for these systems and indicates that there is a different mechanism for the appearance of these states.

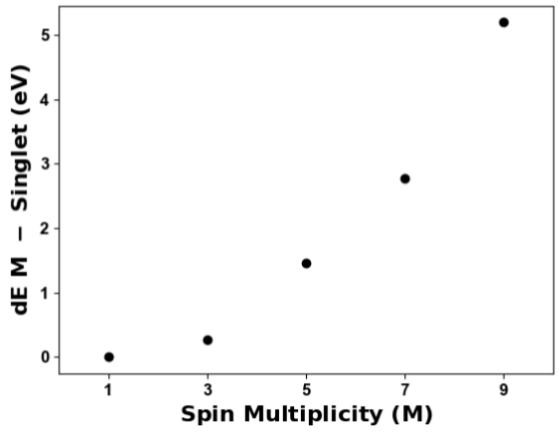

Figure 2.15. The self-consistent field (SCF) energies for the $In_{10}P_4S_6/Zn_{67}Se_{67}$ QD optimized with various spin configurations. Optimization was performed against the displacement (maximum and Root Mean Squared, RMS, values of 0.0018 and 0.0012 Bohr, respectively) and force (maximum

and RMS values of 0.00045 and 0.00030 Hartree/Bohr, respectively) as was done in the main text. The reported energy (in eV) is the difference between the multiplet (S=n/2, n=2, 4, 6, 8) and the singlet (S=0) systems. The lower the energy, the more stable the configuration.

Localization of the band-edge MOs to the anions was observed in the core/shell structures (**Figure 2.13**). This localization introduces unique states in the doped systems that are dependent on the atomic composition of the core/shell interface. In the case of the As-rich system, these states are still within the conduction band, however for the Se- and S-rich systems these introduced states are above the conduction band resulting in a significant red-shift of the absorption spectrum, and thus the appearance of hole-trap states that have been experimentally noted.

2.3 CONCLUSIONS

To summarize, we have synthesized a series of InP and InP/ZnSe QDs with anion-rich interfaces using reactive trimethylsilyl reagents and confirmed successful modification using NMR spectroscopy and elemental analysis. We have correlated these surface chemistry modifications with the resulting steady state and time-resolved PL properties of the QDs. UV-Vis and steady-state PL indicate that anion treatment of the InP cores induces delocalization of the exciton wavefunction and relaxation of core confinement. InP/ZnSe QDs prepared with modulated interfaces result in similar PL decay dynamics on the ns timescale, while the relatively low in PL QYs suggest the creation of new hole traps or non-radiative recombination channels, likely resulting in a permanently dark fraction. Although the standardized ZnSe shelling procedure did not result in improved PL properties for anion-doped InP QDs, we have successfully demonstrated surface-limited reaction chemistry with trimethylsilyl anion reagents as a method to deposit submonolayer inorganic shells and obtain a degree of control over shell growth and final

absorption and PL profiles. These results introduce a useful method for interfacial control and show that the dynamics are not dramatically impacted at the ns timescale; but PL QYs are still highly sensitive to interfacial composition. DFT calculations show that shallow hole traps are introduced that depend on the atomic composition of the core/shell interface. With increasing complexity and high applicability of QD materials, this work opens doors to atomistic control of the surface and interfaces of nanoscale materials.

2.4 EXPERIMENTAL

2.4.1 *General considerations and materials*

All glassware was dried in a 160 °C oven overnight prior to use. All reactions, unless otherwise noted, were performed under an inert atmosphere of nitrogen using a glovebox or using standard Schlenk techniques. Indium acetate (99.99%), anhydrous oleic acid (≥99%), anhydrous acetonitrile, anhydrous ethanol, anhydrous trioctylphosphine (TOP, 97%), bis(trimethylsilylmethyl) sulfide ($(TMS)_2S$) (≥98%), zinc stearate, and selenium powder (99.99%) were purchased from MilliporeSigma and used without further purification. Sulfur powder (99.5% sublimed) was purchased from Acros Organics and used without further purification. Toluene was purchased from MilliporeSigma, collected from a solvent still and stored over activated 3 Å molecular sieves in a glovebox. 1-Octadecene (1-ODE, 90%) and trioctylamine (TOA, 98%) were purchased from MilliporeSigma, dried over CaH_2, distilled, and stored over activated 3 Å molecular sieves in a nitrogen atmosphere glovebox. C_6D_6 was purchased from Cambridge Isotope Laboratories and was similarly dried and stored. Bio-Beads S-X1 for gel permeation chromatography were purchased from Bio-Rad Laboratories and dried under vacuum at elevated temperature before being stored in a glovebox. Omni Trace nitric acid was purchased from MilliporeSigma and used without further purification. 18 MΩ water was collected from

MilliporeSigma water purification system. $P(SiMe_3)_3$ was prepared by modifying a literature procedure in which sodium naphthalene was used in place of Na/K alloy.[35] $As(SiMe_3)_3$ was prepared by adapting the same procedure and substituting metallic arsenic for red phosphorus. *Caution: Both $P(SiMe_3)_3$ and $As(SiMe_3)_3$ are toxic and highly pyrophoric liquids that may form toxic phosphine or arsine gas upon reaction with air or water. Arsenic is toxic and capable of bioaccumulation.* $Se(SiMe_3)_2$ was prepared by following a literature method.[57]

2.4.2 *Synthesis of InP QDs*

Oleate-capped InP QDs were synthesized from oleate-capped InP magic-sized clusters following a modified preparation.[58,59] Briefly, InP clusters (234 mg, 0.012 mmol) were dissolved in 5 mL of 1-ODE and hot-injected into a flask containing 35 mL of 1-ODE at 300 °C. The growth of the nanocrystals was monitored by UV-vis spectroscopy until the absorbance maximum no longer redshifted and was halted between 40-60 min. Once the reaction was complete, the heating mantle was removed to cool down the solution flask. To start purification, 1-ODE was removed by vacuum distillation, and the resulting nanocrystal paste was transferred into a glovebox for precipitation/redissolution cycles using toluene and acetonitrile as solvent and anti-solvent, respectively. Purified InP QDs were dissolved in ~10 mL of toluene and stored as a stock solution in a glovebox. The absorbance value for 100 µL in 3 mL toluene was found to be 0.197 for 7 mL of stock solution containing 0.04 mmol In and used to calculate QD stock concentration.

2.4.3 *Synthesis of anion-rich InP QDs*

From a stock solution of InP QDs, a volume containing 0.1 mmol In was transferred to a vial and dried under reduced pressure. The quantum dot solids were redissolved in 1 mL of trioctylamine (TOA) and transferred into a Schlenk tube containing a stir bar. To 1 mL of TOA in

a separate vial, 6 µL of $P(SiMe_3)_3$ (0.05 mmol) was added. The mixture was transferred to the Schlenk tube and taken out of the glovebox to heat at 150 °C for 1 hour in an oil bath with stirring. $P(SiMe_3)_3$ was replaced with $As(SiMe_3)_3$, $S(SiMe_3)_2$, and $Se(SiMe_3)_2$ for As, S, and Se-treated QD surfaces, respectively.

2.4.4 *Synthesis of InP/ZnSe QDs*

From a stock solution of InP QDs, a volume containing 0.1 mmol In was transferred to a vial and dried under reduced pressure. The QD solids were redissolved in 4 mL of TOA, injected into an evacuated flask, and brought up to 150 °C while stirring. After 60 min, the temperature was raised to 220 °C and zinc stearate (316 mg, 0.5 mmol, suspended in 3 mL of 1-ODE) was injected slowly (0.15 mL/min). 40 min after injection, TOP-Se (0.5 mmol, from 1 M solution, suspended in 1 mL 1-ODE) was added slowly (0.075 mL/min) and the reaction temperature was raised to 300 °C. The reaction was monitored by UV-Vis and PL spectroscopy and halted after 60 min. After the reaction flask was cooled to room temperature, 1-ODE was removed by vacuum distillation. The reaction flask was transferred into a glovebox for precipitation/redissolution cycles using toluene and acetonitrile (or ethanol) as solvent and anti-solvent, respectively. For size selective precipitation, several drops of ethanol were added to the nanocrystals suspended in ~0.5 mL toluene. The mixture was centrifuged at 5000 rpm for 5 minutes. After separating out the supernatant, the procedure was repeated 2 more times.

2.4.5 *Synthesis of InP/ZnSe QDs with anion-rich interface*

InP/ZnSe QDs with anion-rich interfaces were prepared following the same steps for making InP/ZnSe QDs, except the QD solids were redissolved in 3 mL of TOA at the start and $P(SiMe_3)_3$ (0.05 mmol in 1 mL of TOA) was slowly injected (0.1 mL/min) to a solution of QD

stirring at 150 °C. $P(SiMe_3)_3$ was replaced with $As(SiMe_3)_3$, $S(SiMe_3)_2$, and $Se(SiMe_3)_2$ for As, S, and Se-treated QD surfaces, respectively. After 60 minutes, the temperature was raised to 220 °C and ZnSe shelling was proceeded as described above.

2.4.6 *Characterization techniques*

^{1}H NMR spectra were collected on a 300 MHz Bruker Avance spectrometer. UV−vis spectra were collected on a Cary 5000 spectrophotometer from Agilent. Fluorescence and absolute quantum yield measurements were taken on a Horiba Jobin Yvon FluoroMax-4 fluorescence spectrophotometer with the QuantaPhi integrating sphere accessory. Powder X-ray diffraction spectra were collected on solid films drop-cast onto a Si wafer using a Bruker D8 Discover diffractometer. QD solids were digested with H_2O_2 and nitric acid overnight and diluted with 18 MΩ water to prepare ICP samples with which ICP-OES was performed using a PerkinElmer Optima 8300. All samples were purified by size-selective purification prior to the analysis and analyzed once except for as-synthesized InP QDs, for which the In:P ratio has been very consistent across at least 10 samples prepared at varying concentrations. Transmission electron microscopy (TEM) images were collected on an FEI Tecnai G2 F20 microscope at 200 kV. TEM samples were prepared by spotting 3 µL of a dilute solution of QDs dispersed in toluene onto an ultrathin carbon on holey carbon support film purchased from Ted Pella. Size distribution analysis was performed on >300 individual NCs per sample. Room temperature time-resolved photoluminescence (TR PL) measurements were performed by exciting colloidal NCs with 430 nm light via a Coherent Inc/Light Source OPerA optical parametric amplifier, power measured at ~30uW; spectra were collected via a Hamamatsu streak camera using a slow scan unit.

2.4.7 *Theory: choice of basis and method*

Calculations were conducted using the Gaussian software package G16.B01[52] using the Perdew, Burke, and Ernzerhof hybrid functional (PBE0)[53–55] to compute the Kohn-Sham ground-state electronic structure. The Los Alamos National Lab 2-Double Zeta (LANL2DZ) pseudopotential and associated basis sets[60–63] was used. This combination is able to fairly accurately reproduce the experimentally-observed 3.7 eV band gap[15] (computational gap is 3.89 eV, +5% in relation to experiment). The electronic structures of excited states were calculated using time-dependent DFT (TD-DFT) within the linear-response framework.[64–66] The structures were considered optimized when both the forces (maximum and root-mean-square (rms) of the force 0.000450 and 0.000300 Hartree/Bohr, respectively) and displacement (maximum and rms displacement 0.0018 and 0.0012 Bohr, respectively) values were below the threshold criteria.

2.4.8 *Calculation of In:P ratio in P-rich InP*

Zhao and Kulik presented models of In-rich spherical zinc blende InP nanocrystals cut from the bulk (supercells) between sizes 2.44 nm to 3.26 nm.[34] In the presented QD framework, a linear relationship is established between the number of surface In atoms (i.e. N(Surf. In)) and the number of InP units (i.e. N(InP units)) which also tracks linearly with the increase in QD diameter. The In:P ratio of these models can be calculated to be between 1 to 0.6-0.7, decreasing with the particle diameter (Table S21 from ref. 34).

The In:P ratio of In-rich, as-synthesized InP QDs (3.1 nm diameter from TEM) used as the starting material in our work was determined to be 1:0.6 by ICP-OES, comparable to the bulk models in this work. While there are other methods and previous studies done to estimate the number of surface indium atoms and the In:P ratio, consistency of the Zhao and Kulik model with the ICP results of our as-synthesized InP QD sample leads us to refer to their detailed study. From

the models developed by Zhao and Kulik, the number of In and P atoms assumes a linear relationship. This allows for estimation of number of In and P atoms for a certain size of the nanocrystal in this size regime. By assuming bulk structure (and bond distance) and simply adding an equivalent anion excess as In excess, zinc blende lattice of P-rich spherical InP QDs was found to have an In:P ratio of 1:1.4.

2.5 REFERENCES

(1) Park, N.; Eagle, F. W.; DeLarme, A. J.; Monahan, M.; LoCurto, T.; Beck, R.; Li, X.; Cossairt, B. M. Tuning the Interfacial Stoichiometry of InP Core and InP/ZnSe Core/Shell Quantum Dots. *J. Chem. Phys.* **2021**, *155* (8), 084701.

(2) Ippen, C.; Guo, W.; Zehnder, D.; Kim, D.; Manders, J.; Barrera, D.; Newmeyer, B.; Hamilton, D.; Wang, C.; Hotz, C.; Ma, R.; Bin, J.-K.; Kim, B.; Kim, K.; Jang, K.; Park, J.; Lee, T.; Kim, W.-Y.; Lee, J. High Efficiency Heavy Metal Free QD-LEDs for next Generation Displays. *J. Soc. Inf. Disp.* **2019**, *27* (6), 338–346.

(3) Jo, J.-H.; Kim, J.-H.; Lee, K.-H.; Han, C.-Y.; Jang, E.-P.; Do, Y. R.; Yang, H. High-Efficiency Red Electroluminescent Device Based on Multishelled InP Quantum Dots. *Opt. Lett.* **2016**, *41* (17), 3984.

(4) Lim, J.; Park, M.; Bae, W. K.; Lee, D.; Lee, S.; Lee, C.; Char, K. Highly Efficient Cadmium-Free Quantum Dot Light-Emitting Diodes Enabled by the Direct Formation of Excitons within InP@ZnSeS Quantum Dots. *ACS Nano* **2013**, *7* (10), 9019–9026.

(5) Kim, Y.; Ham, S.; Jang, H.; Min, J. H.; Chung, H.; Lee, J.; Kim, D.; Jang, E. Bright and Uniform Green Light Emitting InP/ZnSe/ZnS Quantum Dots for Wide Color Gamut Displays. *ACS Appl. Nano Mater.* **2019**, *2* (3), 1496–1504.

(6) Zhang, H.; Ma, X.; Lin, Q.; Zeng, Z.; Wang, H.; Li, L. S.; Shen, H.; Jia, Y.; Du, Z. High-Brightness Blue InP Quantum Dot-Based Electroluminescent Devices: The Role of Shell Thickness. *J. Phys. Chem. Lett.* **2020**, *11* (3), 960–967.

(7) Lee, T.; Hahm, D.; Kim, K.; Bae, W. K.; Lee, C.; Kwak, J. Highly Efficient and Bright Inverted Top-Emitting InP Quantum Dot Light-Emitting Diodes Introducing a Hole-Suppressing Interlayer. *Small* **2019**, *15* (50), 1905162.

(8) Won, Y.-H.; Cho, O.; Kim, T.; Chung, D.-Y.; Kim, T.; Chung, H.; Jang, H.; Lee, J.; Kim, D.; Jang, E. Highly Efficient and Stable InP/ZnSe/ZnS Quantum Dot Light-Emitting Diodes. *Nature* **2019**, *575* (7784), 634–638.

(9) Li, Y.; Hou, X.; Dai, X.; Yao, Z.; Lv, L.; Jin, Y.; Peng, X. Stoichiometry-Controlled InP-Based Quantum Dots: Synthesis, Photoluminescence, and Electroluminescence. *J. Am. Chem. Soc.* **2019**, *141* (16), 6448–6452.

(10) Fu, H.; Zunger, A. InP Quantum Dots: Electronic Structure, Surface Effects, and the Redshifted Emission. *Physical Review B* **1997**, *56* (3), 1496.

(11) Adam, S.; Talapin, D. V.; Borchert, H.; Lobo, A.; McGinley, C.; de Castro, A. R. B.; Haase, M.; Weller, H.; Möller, T. The Effect of Nanocrystal Surface Structure on the Luminescence

Properties: Photoemission Study of HF-Etched InP Nanocrystals. *J. Chem. Phys.* **2005**, *123* (8), 084706.
(12) Kilina, S. V.; Tamukong, P. K.; Kilin, D. S. Surface Chemistry of Semiconducting Quantum Dots: Theoretical Perspectives. *Acc. Chem. Res.* **2016**, *49* (10), 2127–2135.
(13) Giansante, C.; Infante, I. Surface Traps in Colloidal Quantum Dots: A Combined Experimental and Theoretical Perspective. *J. Phys. Chem. Lett.* **2017**, *8* (20), 5209–5215.
(14) Houtepen, A. J.; Hens, Z.; Owen, J. S.; Infante, I. On the Origin of Surface Traps in Colloidal II–VI Semiconductor Nanocrystals. *Chem. Mater.* **2017**, *29* (2), 752–761.
(15) Cho, E.; Kim, T.; Choi, S.; Jang, H.; Min, K.; Jang, E. Optical Characteristics of the Surface Defects in InP Colloidal Quantum Dots for Highly Efficient Light-Emitting Applications. *ACS Appl. Nano Mater.* **2018**, *1* (12), 7106–7114.
(16) Kovalenko, M. V.; Scheele, M.; Talapin, D. V. Colloidal Nanocrystals with Molecular Metal Chalcogenide Surface Ligands. *Science* **2009**, *324* (5933), 1417–1420.
(17) Frederick, M. T.; Weiss, E. A. Relaxation of Exciton Confinement in CdSe Quantum Dots by Modification with a Conjugated Dithiocarbamate Ligand. *ACS Nano* **2010**, *4* (6), 3195–3200.
(18) Cossairt, B. M.; Juhas, P.; Billinge, S. J. L.; Owen, J. S. Tuning the Surface Structure and Optical Properties of CdSe Clusters Using Coordination Chemistry. *J. Phys. Chem. Lett.* **2011**, *2* (24), 3075–3080.
(19) Jin, S.; Harris, R. D.; Lau, B.; Aruda, K. O.; Amin, V. A.; Weiss, E. A. Enhanced Rate of Radiative Decay in CdSe Quantum Dots upon Adsorption of an Exciton-Delocalizing Ligand. *Nano Lett.* **2014**, *14* (9), 5323–5328.
(20) Kim, J.-Y.; Kotov, N. A. Charge Transport Dilemma of Solution-Processed Nanomaterials. *Chem. Mater.* **2014**, *26* (1), 134–152.
(21) Boles, M. A.; Ling, D.; Hyeon, T.; Talapin, D. V. The Surface Science of Nanocrystals. *Nature Materials* **2016**, *15* (2), 141–153.
(22) Stein, J. L.; Mader, E. A.; Cossairt, B. M. Luminescent InP Quantum Dots with Tunable Emission by Post-Synthetic Modification with Lewis Acids. *J. Phys. Chem. Lett.* **2016**, *7* (7), 1315–1320.
(23) Kim, T.-G.; Zherebetskyy, D.; Bekenstein, Y.; Oh, M. H.; Wang, L.-W.; Jang, E.; Alivisatos, A. P. Trap Passivation in Indium-Based Quantum Dots through Surface Fluorination: Mechanism and Applications. *ACS Nano* **2018**, *12* (11), 11529–11540.
(24) Hughes, K. E.; Stein, J. L.; Friedfeld, M. R.; Cossairt, B. M.; Gamelin, D. R. Effects of Surface Chemistry on the Photophysics of Colloidal InP Nanocrystals. *ACS Nano* **2019**, *13* (12), 14198–14207.
(25) Toufanian, R.; Piryatinski, A.; Mahler, A. H.; Iyer, R.; Hollingsworth, J. A.; Dennis, A. M. Bandgap Engineering of Indium Phosphide-Based Core/Shell Heterostructures Through Shell Composition and Thickness. *Front Chem* **2018**, *6*.
(26) Jang, E.; Kim, Y.; Won, Y.-H.; Jang, H.; Choi, S.-M. Environmentally Friendly InP-Based Quantum Dots for Efficient Wide Color Gamut Displays. *ACS Energy Lett.* **2020**, *5* (4), 1316–1327.
(27) Cao, F.; Wang, S.; Wang, F.; Wu, Q.; Zhao, D.; Yang, X. A Layer-by-Layer Growth Strategy for Large-Size InP/ZnSe/ZnS Core–Shell Quantum Dots Enabling High-Efficiency Light-Emitting Diodes. *Chem. Mater.* **2018**, *30* (21), 8002–8007.
(28) Pietra, F.; De Trizio, L.; Hoekstra, A. W.; Renaud, N.; Prato, M.; Grozema, F. C.; Baesjou, P. J.; Koole, R.; Manna, L.; Houtepen, A. J. Tuning the Lattice Parameter of In_xZn_yP for Highly Luminescent Lattice-Matched Core/Shell Quantum Dots. *ACS Nano* **2016**, *10* (4), 4754–4762.

(29) Mulder, J. T.; Kirkwood, N.; De Trizio, L.; Li, C.; Bals, S.; Manna, L.; Houtepen, A. J. Developing Lattice Matched ZnMgSe Shells on InZnP Quantum Dots for Phosphor Applications. *ACS Appl. Nano Mater.* **2020**, *3* (4), 3859-3867.
(30) Park, Y.-S.; Bae, W. K.; Padilha, L. A.; Pietryga, J. M.; Klimov, V. I. Effect of the Core/Shell Interface on Auger Recombination Evaluated by Single-Quantum-Dot Spectroscopy. *Nano Lett.* **2014**, *14* (2), 396–402.
(31) Freymeyer, N. J.; Click, S. M.; Reid, K. R.; Chisholm, M. F.; Bradsher, C. E.; McBride, J. R.; Rosenthal, S. J. Effect of Indium Alloying on the Charge Carrier Dynamics of Thick-Shell InP/ZnSe Quantum Dots. *J. Chem. Phys.* **2020**, *152* (16), 161104.
(32) Rodosthenous, P.; Gómez-Campos, F. M.; Califano, M. Tuning the Radiative Lifetime in InP Colloidal Quantum Dots by Controlling the Surface Stoichiometry. *J. Phys. Chem. Lett.* **2020**, *11* (23), 10124–10130.
(33) Rusishvili, M.; Wippermann, S.; Talapin, D. V.; Galli, G. Stoichiometry of the Core Determines the Electronic Structure of Core–Shell III–V/II–VI Nanoparticles. *Chem. Mater.* **2020**, *32* (22), 9798–9804.
(34) Zhao, Q.; Kulik, H. J. Electronic Structure Origins of Surface-Dependent Growth in III–V Quantum Dots. *Chem. Mater.* **2018**, *30* (20), 7154–7165.
(35) Gary, D. C.; Cossairt, B. M. Role of Acid in Precursor Conversion During InP Quantum Dot Synthesis. *Chem. Mater.* **2013**, *25* (12), 2463–2469.
(36) Chen, P. E.; Anderson, N. C.; Norman, Z. M.; Owen, J. S. Tight Binding of Carboxylate, Phosphonate, and Carbamate Anions to Stoichiometric CdSe Nanocrystals. *J. Am. Chem. Soc.* **2017**, *139* (8), 3227–3236.
(37) Ritchhart, A.; Cossairt, B. M. Quantifying Ligand Exchange on InP Using an Atomically Precise Cluster Platform. *Inorg. Chem.* **2019**, *58* (4), 2840–2847.
(38) Kim, S.-W.; Zimmer, J. P.; Ohnishi, S.; Tracy, J. B.; Frangioni, J. V.; Bawendi, M. G. Engineering $InAs_xP_{1-x}$/InP/ZnSe III−V Alloyed Core/Shell Quantum Dots for the Near-Infrared. *J. Am. Chem. Soc.* **2005**, *127* (30), 10526–10532.
(39) Buckley, J. J.; Couderc, E.; Greaney, M. J.; Munteanu, J.; Riche, C. T.; Bradforth, S. E.; Brutchey, R. L. Chalcogenol Ligand Toolbox for CdSe Nanocrystals and Their Influence on Exciton Relaxation Pathways. *ACS Nano* **2014**, *8* (3), 2512–2521.
(40) Gentle, C. M.; Wang, Y.; Haddock, T. N.; Dykstra, C. P.; van der Veen, R. M. Internal Atomic-Scale Structure Determination and Band Alignment of II–VI Quantum Dot Heterostructures. *J. Phys. Chem. C* **2020**, *124* (6), 3895–3904.
(41) Ramvall, P.; Tanaka, S.; Nomura, S.; Riblet, P.; Aoyagi, Y. Observation of Confinement-Dependent Exciton Binding Energy of GaN Quantum Dots. *Appl. Phys. Lett.* **1998**, *73* (8), 1104–1106.
(42) Monchen, J. O. V.; Crisp, R. W.; Grimaldi, G.; Bergstein, H. A. C.; du Fossé, I.; van der Stam, W.; Infante, I.; Houtepen, A. J. Finding and Fixing Traps in II–VI and III–V Colloidal Quantum Dots: The Importance of Z-Type Ligand Passivation. *J. Am. Chem. Soc.* **2018**, *140* (46), 15712-15723.
(43) Holder, C. F.; Schaak, R. E. Tutorial on Powder X-Ray Diffraction for Characterizing Nanoscale Materials. *ACS Nano* **2019**, *13* (7), 7359–7365.
(44) Sarkar, A.; Mukherjee, P.; Barat, P. X-Ray Diffraction Studies on Asymmetrically Broadened Peaks of Heavily Deformed Zirconium-Based Alloys. *Mater. Sci. Eng. A* **2008**, *485* (1), 176–181.
(45) Efros, Al. L.; Rosen, M. Random Telegraph Signal in the Photoluminescence Intensity of a Single Quantum Dot. *Phys. Rev. Lett.* **1997**, *78* (6), 1110–1113.

(46) Frantsuzov, P. A.; Marcus, R. A. Explanation of Quantum Dot Blinking without the Long-Lived Trap Hypothesis. *Phys. Rev. B* **2005**, *72* (15), 155321.
(47) Heyes, C. D.; Kobitski, A. Yu.; Breus, V. V.; Nienhaus, G. U. Effect of the Shell on the Blinking Statistics of Core-Shell Quantum Dots: A Single-Particle Fluorescence Study. *Phys. Rev. B* **2007**, *75* (12), 125431.
(48) Hanrahan, M. P.; Stein, J. L.; Park, N.; Cossairt, B. M.; Rossini, A. J. Elucidating the Location of Cd^{2+} in Post-Synthetically Treated InP Quantum Dots Using Dynamic Nuclear Polarization ^{31}P and ^{113}Cd Solid-State NMR Spectroscopy. *J. Phys. Chem. C* **2021**, *125* (5), 2956-2965.
(49) Vainshtein, I. A.; Zatsepin, A. F.; Kortov, V. S. Applicability of the Empirical Varshni Relation for the Temperature Dependence of the Width of the Band Gap. *Phys. Solid State* **1999**, *41* (6), 905–908.
(50) Lewis, J. E.; Wu, S.; Jiang, X. J. Unconventional Gap State of Trapped Exciton in Lead Sulfide Quantum Dots. *Nanotechnology* **2010**, *21* (45), 455402.
(51) Gaponenko, M. S.; Tolstik, N. A.; Lutich, A. A.; Onushchenko, A. A.; Yumashev, K. V. Temperature-Dependent Photoluminescence Stokes Shift in PbS Quantum Dots. *Physica E: Low Dimens. Syst. Nanostruct.* **2013**, *53*, 63–65.
(52) M. J. Frisch, G. W. Trucks, H. B. Schlegel, G. E. Scuseria, M. A. Robb, J. R. Cheeseman, G. Scalmani, V. Barone, G. A. Petersson, H. Nakatsuji, X. Li, M. Caricato, A. V. Marenich, J. Bloino, B. G. Janesko, R. Gomperts, B. Mennucci, H. P. Hratchian, J. V. Ortiz, A. F. Izmaylov, J. L. Sonnenberg, D. Williams-Young, F. Ding, F. Lipparini, F. Egidi, J. Goings, B. Peng, A. Petrone, T. Henderson, D. Ranasinghe, V. G. Zakrzewski, J. Gao, N. Rega, G. Zheng, W. Liang, M. Hada, M. Ehara, K. Toyota, R. Fukuda, J. Hasegawa, M. Ishida, T. Nakajima, Y. Honda, O. Kitao, H. Nakai, T. Vreven, K. Throssell, J. A. Montgomery, Jr., J. E. Peralta, F. Ogliaro, M. J. Bearpark, J. J. Heyd, E. N. Brothers, K. N. Kudin, V. N. Staroverov, T. A. Keith, R. Kobayashi, J. Normand, K. Raghavachari, A. P. Rendell, J. C. Burant, S. S. Iyengar, J. Tomasi, M. Cossi, J. M. Millam, M. Klene, C. Adamo, R. Cammi, J. W. Ochterski, R. L. Martin, K. Morokuma, O. Farkas,; J. B. Foresman, and D. J. Fox. Gaussian 16, Revision B.01, 2016.
(53) Perdew, J. P.; Burke, K.; Ernzerhof, M. Generalized Gradient Approximation Made Simple. *Phys. Rev. Lett.* **1997**, *78* (7), 1396–1396.
(54) Ernzerhof, M.; Scuseria, G. E. Assessment of the Perdew–Burke–Ernzerhof Exchange-Correlation Functional. *J. Chem. Phys.* **1999**, *110* (11), 5029–5036.
(55) Adamo, C.; Barone, V. Toward Reliable Density Functional Methods without Adjustable Parameters: The PBE0 Model. *J. Chem. Phys.* **1999**, *110* (13), 6158–6170.
(56) Snee, P. T. DFT Calculations of InP Quantum Dots: Model Chemistries, Surface Passivation, and Open-Shell Singlet Ground States. *J. Phys. Chem. C* **2021**, *125* (21), 11765-11772.
(57) Detty, M. R.; Seidler, M. D. Bis(Trialkylsilyl) Chalcogenides. 1. Preparation and Reduction of Group VIA Oxides. *J. Org. Chem.* **1982**, *47* (7), 1354–1356.
(58) Gary, D. C.; Terban, M. W.; Billinge, S. J. L.; Cossairt, B. M. Two-Step Nucleation and Growth of InP Quantum Dots via Magic-Sized Cluster Intermediates. *Chem. Mater.* **2015**, *27* (4), 1432–1441.
(59) Park, N.; Monahan, M.; Ritchhart, A.; Friedfeld, M. R.; Cossairt, B. M. Synthesis of $In_{37}P_{20}(O_2CR)_{51}$ Clusters and Their Conversion to InP Quantum Dots. *J. Vis. Exp.* **2019**, 147. doi: 10.3791/59425.
(60) Dunning Jr., T. H; Hay, P. J. *Methods of Electronic Structure Theory*, *Ed. H. F. Schaefer III*; Plenum Press: New York, 1977; Vol. 3.
(61) Hay, P. J.; Wadt, W. R. Ab Initio Effective Core Potentials for Molecular Calculations. Potentials for the Transition Metal Atoms Sc to Hg. *J. Chem. Phys.* **1985**, *82* (1), 270–283.

(62) Hay, P. J.; Wadt, W. R. Ab Initio Effective Core Potentials for Molecular Calculations. Potentials for K to Au Including the Outermost Core Orbitals. *J. Chem. Phys.* **1985**, *82* (1), 299–310..
(63) Wadt, W. R.; Hay, P. J. Ab Initio Effective Core Potentials for Molecular Calculations. Potentials for Main Group Elements Na to Bi. *J. Chem. Phys.* **1985**, *82* (1), 284–298.
(64) Casida, M. E. *Recent Advances in Density Functional Methods: Part I, Ed. D. P. Chong*; World Scientific: Singapore, 1995; Vol. 1.
(65) Dreuw, A.; Head-Gordon, M. Single-Reference Ab Initio Methods for the Calculation of Excited States of Large Molecules. *Chem. Rev.* **2005**, *105* (11), 4009–4037.
(66) Stratmann, R. E.; Scuseria, G. E.; Frisch, M. J. An Efficient Implementation of Time-Dependent Density-Functional Theory for the Calculation of Excitation Energies of Large Molecules. *J. Chem. Phys.* **1998**, *109* (19), 8218–8224.

Chapter 3. Colloidal, Room Temperature Growth of Metal Oxide Shell on InP Quantum Dots

3.1 INTRODUCTION

The utility of colloidal quantum dots, or solution-processed semiconducting nanocrystals, has expanded significantly in the past decade to lead the development of modern optoelectronics.[1–4] Innovations in materials synthesis, control over complex hybrid and heterostructured interfaces, and understanding the multifaceted and nuanced relationships between structure and function are at the core of this advancement. Indium phosphide quantum dots (InP QDs) have risen to a place of prominence and competitiveness especially as highly bright and stable emitters for display and LED technologies.[5–7] Recent innovations in InP-based quantum dot emitters have incorporated strategies such as surface oxide removal by HF treatment prior to wider band gap shelling[6,8], elimination of indium defects in the shell through extra purification steps prior to shell growth[7], and careful engineering of core/shell band alignment through tuning the core size and shell thickness[3,5,9], and the composition of core and inner and outer shell layers.[10–13]

Surface oxide defects must be considered in the design of bright and narrow InP QD emitters. Many studies have reported both detriments and advantages associated with oxidative species at the core/shell interface.[6,14,15] Oxidation of InP quantum dot surfaces is an inherent byproduct of commonly used synthetic methods.[16–18] It is therefore interesting to consider how to turn this limitation into a desirable feature. In fact, it has been demonstrated that surface oxidation can be exploited to develop some of the best performing emitters. Some studies of interfacial surface oxides have attributed ensuing high photoluminescence quantum yield (PL QY) to alleviating lattice strain and removing interfacial defects or dangling bonds, resulting in an epitaxial core/shell interface.[3,14,15,19,20] In recent work reporting near unity PL QY, water was

injected with HF during synthesis, in addition to the use of highly polar, “wet” anti-solvents such as ethanol and acetone during post-synthesis purification.[6]

There is increasing consensus in the literature about the potential beneficial role of the surface phosphate layer on InP regarding its enhancement of PL QY, leading to procedures that directly introduce phosphate, water, or both, to achieve control over the core/shell interface.[21] However, oxidative defects have simultaneously been thought to limit the PL QY in certain cases and broaden linewidths, hurting the efficiency and color purity in devices.[22,23] Single particle spectroscopy results have demonstrated that InP linewidths are not inherently broader than CdSe, suggesting sample polydispersity needs to be controlled synthetically by not only a focus on reliable, size-controlled core growth, but also uniform surface passivation and well-controlled shelling.[24] Computational work has also shown that exciton-phonon coupling can also contribute to linewidth broadening,[25] and this is exacerbated by incomplete surface passivation and the structural disorder caused by defects.[22]

Complementary to investigating atomically precise control over the surface structure and stoichiometry, there has been growing interest in the field to explore layer-by-layer growth of heterostructures.[5,26–29] Talapin et al. have demonstrated the synthesis of “digital” nano-heterostructures through colloidal atomic layer deposition (c-ALD), inspired by the conventional method of solid film deposition.[26,27] While conventional ALD leverages alternating cycles of two self-limiting reactions in vapor phase and purge steps in between to remove excess reagents to formulate conformal and uniform layer-by-layer growth on a nanostructure substrate, c-ALD relies on the phase change of nanomaterials in liquids and requires preservation of colloidal stability between transfers.[27] Using similar motifs, Klimov et al. have shown formulation of interlayers

between core/shells to achieve monolayer control.[30] Like ALD, they demonstrated using evacuation steps between each addition to remove excess precursors.

Here, we demonstrate a facile, room temperature procedure for colloidal metal oxide shelling of InP nanocrystals. First, we show using theoretical modeling that surface oxides on InP QDs are detrimental to bright and narrow linewidth PL, since they introduce nonradiative recombination pathways. We then compare these structures with other monolayer metal oxide shells on InP QD (M = Zn, Cd, Ga, Al) and find that ZnO and CdO shells, unlike GaO and AlO shells, reduce nonradiative rate and result in a density of states near the valence band maximum (VBM) that looks similar to that of defect-free, stoichiometric InP QDs. Inspired by these results, we employed reagents commonly used for atomic layer deposition of metal oxides to systematically grow metal oxide shells on InP QDs. The colloidal, layer-by-layer shelling approach is generalizable to many metal oxides (M = Zn, Cd, Ga, Al). The presence of a thin metal oxide shell is evident from the first precursor addition step by powder X-ray diffraction (pXRD) and extended X-ray absorption fine structure spectroscopy (EXAFS). Repeated cycles of precursor addition promote continued growth without changing the InP core stoichiometry. To investigate the impact of the metal oxide interfaces on the PL properties, we have synthesized and compared the resultant PL of bright InP/ZnSe core/shells with metal oxide interfaces where enhancement in the PL QY was observed and the narrowing of the linewidth was attributed to the reduction of oxidized P fraction probed by X-ray emission spectroscopy (XES) and larger kinetic barrier for ions to diffuse across the shell layer. These results present a facile and versatile strategy to finely tune and leverage the oxidic defects at the core/shell interface as we gain more understanding of the design principles for improved emission properties of QD materials.

3.2 Results and Discussion

3.2.1 *Investigation of the effects of surface oxide through computational modeling*

The prevalence of oxidic surface species in InP quantum dots and their impact on the optoelectronic properties have generated many empirical studies probing and controlling the average extent of P oxidation, typically measured by solid-state ^{31}P NMR spectroscopy[16,17], with the goal of improving optical properties. While a mixture of oxidic species such as phosphate, polyphosphate, hydroxide, and oxide may be present at the InP surface, it is not clear that they are all detrimental to PL QY when present at the core/shell interface. An attempt at modeling this system would mean making some critical assumptions, such as randomly distributing the oxides both spatially and in terms of their speciation at the InP QD surface. Computational studies have thus far focused on InP cores and epitaxial core/shells assessing the effects of stoichiometry or incorporation of GaP interlayers[31–33], besides one study that reported on the use of slab geometry of stoichiometry $In_8P_8O_4$ to show reduced lattice constant and a smaller band gap as a result of InP QD surface oxidation.[34]

We constructed $In_{31}P_{31}/In_{46}O_{46}$ as an exaggerated oxidized InP core that is fully passivated by a monolayer indium oxide shell (optimized structure are shown in **3.4.8**). In this structure, surface P atoms of an $In_{77}P_{77}$ core were replaced with O atoms. Realistically, oxide coverage in as-synthesized InP QDs is far less than a complete shell (12% phosphate species measured by Chaudret et al.[16] using ss-NMR) and for our samples synthesized from InP magic-sized clusters, we measured 16% oxidized phosphorus after synthesis by P X-ray emission spectroscopy (XES, **Figure 3.5b**), indicating the presence of phosphate that is not explicitly accounted for in this model.

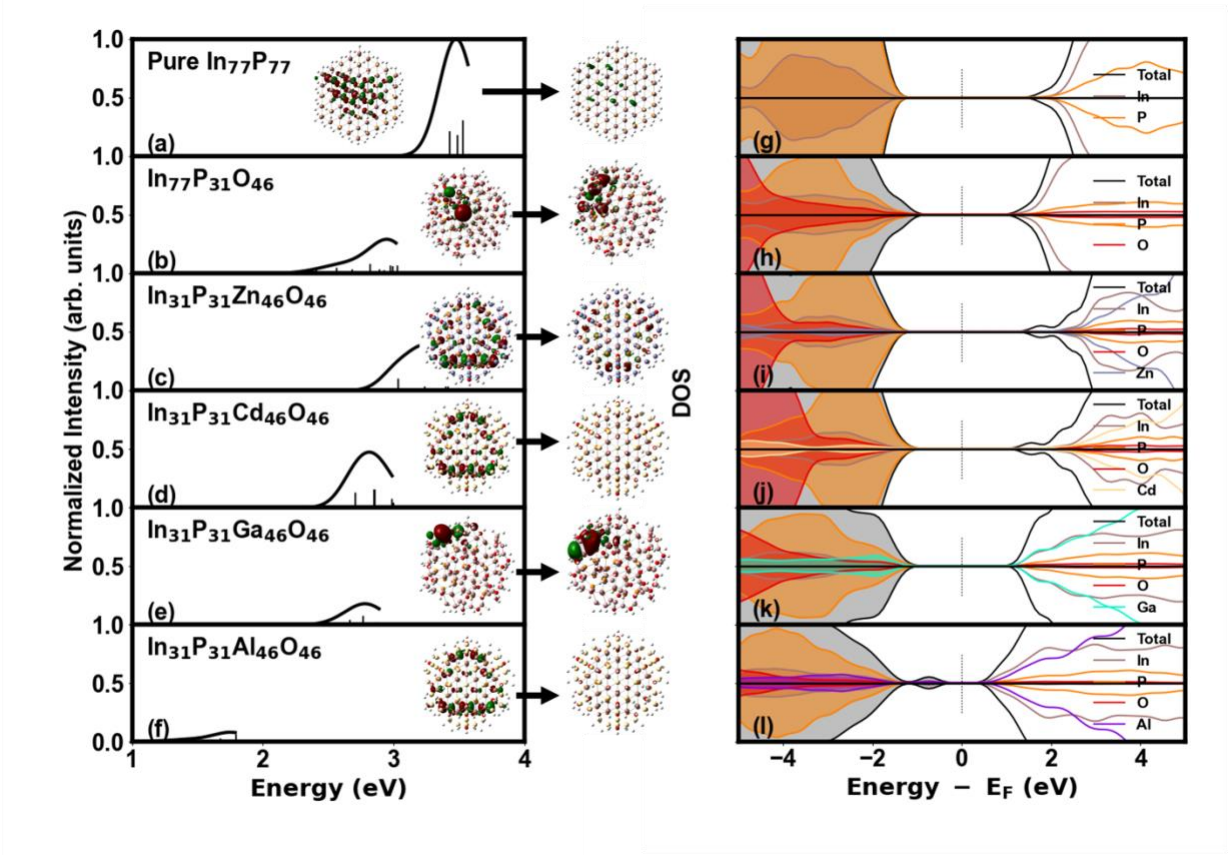

Figure 3.1. Linear response absorption plots for the (a) pure InP, and (b-f) metal oxide shelled InP (M = In, Zn, Cd, Al, Ga) quantum dots. (Inset: leaving (left) and arriving (right) natural transition orbitals for the first bright (f > 0.001) excited state for each quantum dot, shown with an isovalue of 0.02. The projected density of states plots is shown for each system in the same order (g-l), indicating contribution from In (brown), P (orange), O (red), and total (black outline shaded in grey). Band reduction from pure InP and introduction of band edge states are observed with the addition of metal oxide shells.

When compared to the stoichiometric, defect-free $In_{77}P_{77}$ core which shows a clean band gap and strong absorbance at 3.4 eV (**Figure 3.1a, g**), $In_{31}P_{31}/In_{46}O_{46}$ exhibits a reduced band gap and emergence of dark states near the band edges (**Figure 3.1b, h**). From the natural transition

orbitals (NTOs), it can be seen that the monolayer of indium oxide shell localizes the charge density at the InP/InO interface (**Figure 3.1b inset**). The projected density of states plot for the InP/InO system shows the contribution of P and O to the valence band, which indicates that at the band edge, the phosphorus component dominates while the oxygen component appears more prominently deeper into the valence band, which is consistent with oxygen being more electronegative (**Figure 3.1h**). There is some contribution near the VBM from indium, which could be attributed to covalent mixing of In and O giving rise to the dark absorption states ($f < 0.001$). Dark states near the band edges have been associated with unfavorable phenomena such as PL blinking and linewidth broadening.[22,35–37] In order to quantify the impact of the dark states on the optical properties of the modeled systems, the ratio of the magnitude of the first order nonadiabatic coupling between the ground and first excited states, $|d|$, for each of the systems was examined (**Figure 3.2**). The rate of nonradiative relaxation will be proportional to $|d|^2$,[38–40] and thus in the case of InP/InO, it can be determined that the rate of nonradiative decay is large in comparison to that of pure InP core. Therefore, InP core with a natively oxidized surface is expected to be a poor starting material for fabricating bright and narrow emitters and motivates us to eliminate these defects or otherwise leverage them to form a more favorable interface.

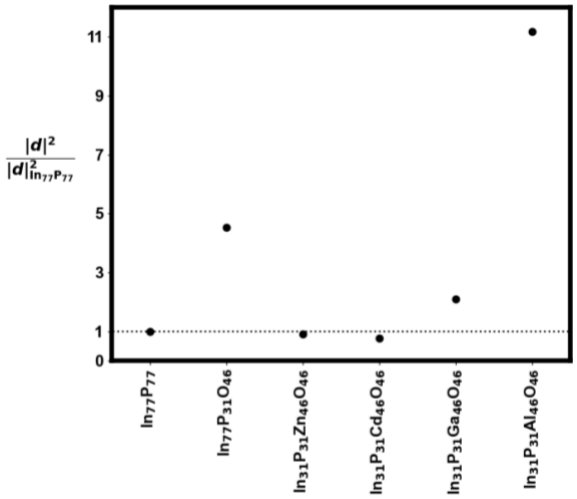

Figure 3.2. Ratio of the magnitude of the nonadiabatic coupling for each $In_{31}P_{31}/M_{46}O_{46}$ to that of $In_{77}P_{77}$. The rate of nonradiative relaxation is proportional to $|d|^2$. Larger ratio indicates how much worse the material is expected to perform for PL applications compared to $In_{77}P_{77}$.

Additional metal oxide shelled structures were constructed by replacing the surface In with a divalent or trivalent metal (M = Zn, Cd, Ga, Al) and the surface phosphorus with oxygen (optimized structures are shown in **3.4.8**). The resulting models had a general formula of $In_{31}P_{31}/M_{46}O_{46}$. Regardless of the bulk stoichiometry of the metal oxides, the metal to oxygen ratio was 1:1. Pseudohydrogens were used to charge balance at the surface in order to achieve neutrally charged models. The divalent metal oxide shells on InP (i.e. ZnO and CdO) exhibit a reduced band gap, and thus a redshifted absorption (3.0 eV and 2.7 eV, respectively) (**Figure 3.1c, d, i, j**) compared to the pure InP core of the same size (3.4 eV). Unlike InP/InO, both ZnO and CdO shells give rise to high density of states near VBM with strong P contribution much like those of pure InP. This effect is accompanied by a reduction of the nonradiative rate compared to both InP/InO and pure InP core (**Figure 3.2**). In both the InP/ZnO and InP/CdO structures, new states can be seen to emerge in the density of states near the edge of the conduction band (**Figure 3.1i, j**). The states arising from the CdO shell extend further into the band gap than in the case of a ZnO shell,

which can be explained by the contribution of the Cd 3d states that lie lower in energy than Zn orbitals. Based on these results, ZnO and CdO shells on InP are promising candidates to replace indium oxide surfaces for improving the optical properties of bright InP-based core/shell QDs. Interestingly, these findings may be related to the PL enhancement of InP QDs upon Zn or Cd carboxylate treatment, as the surface environment of Zn or Cd carboxylate-capped InP QDs are expected to be analogous to that of metal oxide in the first coordination shell.

For InP shelled with either gallium or aluminum oxide, the change in the density of states from the stoichiometric, defect-free $In_{77}P_{77}$ core is seen more prominently at the VBM **(Figure 3.1k, l)**. This was also the case for $In_{31}P_{31}/In_{46}O_{46}$ as previously discussed. The GaO and AlO shelled structures show surface localized states near the VBM that have reduced contribution from P at the band edge and a relative increase in the contribution from the added metal and oxygen. Both InP/GaO and InP/AlO are expected to exhibit faster nonradiative decay (**Figure 3.2**), given the presence the band edge defect states caused by the oxide layer**.** The first bright states in these systems are calculated to be at 2.6 eV for GaO and 1.1 eV for AlO **(Figure 3.1e, f)**, indicating a redshifted absorption compared to $In_{77}P_{77}$, like all metal oxide shells examined here. The natural transition orbitals (NTOs) for the transitions for all systems are shown in **Figure 3.1a-f insets**. The InP/InO, InP/GaO, and InP/AlO systems have localized defect-like states near their surface when compared to the pure InP, InP/CdO, and InP/ZnO systems. The localized defect-like surface states result in a much higher ratio of the nonradiative rates and are not expected to yield well-performing emitters.

Additionally, we have explored $In_{31}P_{77}M_{46}$ (M = Zn, Cd, Ga, Al) structures, where only the surface In atoms are replaced by other metals without the oxides. Examining the electronic structure of these systems reveals that the impact on the absorption features and nonadiabatic

coupling is stronger when there is oxide layer present than with any of the metals by themselves (**Figure 3.3**). We observed clean band gaps for all structures with an increased band gap for $In_{31}P_{77}Ga_{46}$ and $In_{31}P_{77}Al_{46}$ and a reduced band gap for $In_{31}P_{77}Zn_{46}$ and $In_{31}P_{77}Cd_{46}$. These results highlight that the surface oxides play an influential role in the electronic structure and the resultant optical properties and should be considered together with their interaction with the identity of the metal on the surface of the core QDs.

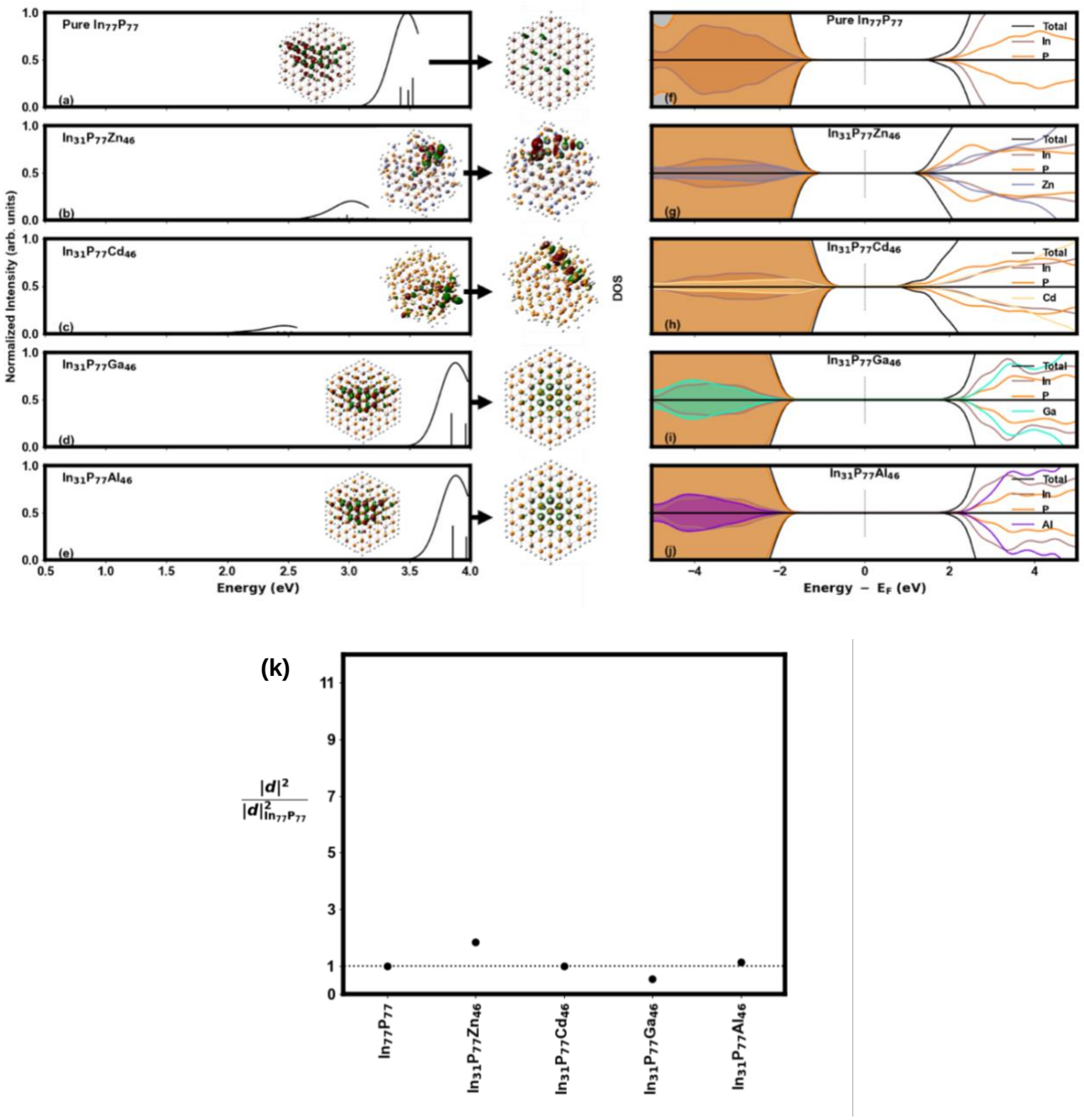

Figure 3.3. (a-e) Calculated absorbance and (f-j) electronic structure of optimized $In_{31}P_{77}M_{46}$ (M = Zn, Cd, Ga, Al) structures. (k) Ratio of the magnitude of the nonadiabatic coupling for each $In_{31}P_{77}M_{46}$ to that of $In_{77}P_{77}$. Compared to metal oxide shelled structures, the overall impact on nonadiabatic coupling is weaker when the surface of InP QD is doped only with metals.

3.2.2 *Growth of metal oxide shells on InP QDs*

3.2.2.1 Synthesis and surface chemistry

The colloidal growth of metal oxide shells on InP QDs starts with the addition of alkyl metal to the QD solution and continues through alternating additions of alkyl metal and water with vacuum purge and redissolution steps in between (**Figure 3.4**). InP QDs were prepared from carboxylate-capped InP magic-sized clusters used as a single source precursor.[41,42] The resulting InP QDs were purified multiple precipitation-centrifugation-redissolution cycles followed by size-selective gel-permeation chromatography.[43,44] An InP QD stock solution was then prepared in toluene with an In concentration of 0.051 mmol/mL.

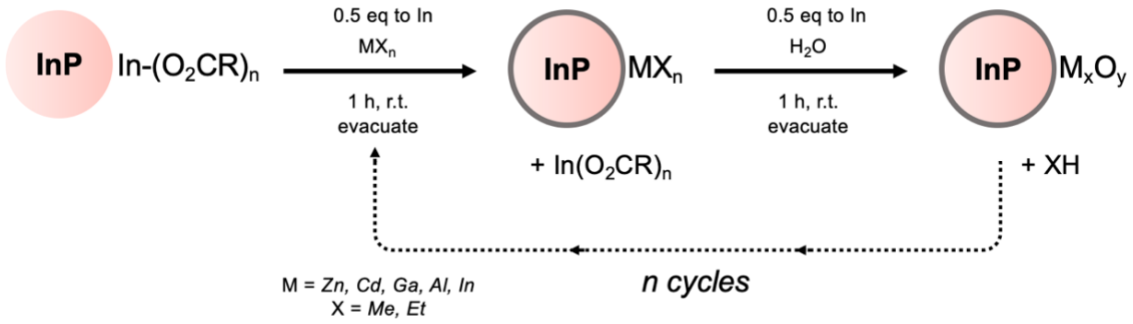

Figure 3.4. Colloidal growth scheme of metal oxide shell on carboxylate-capped InP QDs.

To a solution of InP QDs, alkyl metal (M = Zn, Cd, Ga, Al, In) was added at half equivalent to the total mmol of In. This approximately corresponds to the mmol of surface In present in the QD solution. While striving toward full characterization of all resultant metal oxide shelled QDs, we chose to follow the growth of the ZnO shelled structure more closely as a representative system throughout this work for more detailed understanding of the surface chemistry. At room temperature, alkyl metal can replace indium carboxylate at the surface and form metastable surface metal-alkyl bonds (broad resonance from ethyl group centered around δ =0.2 ppm) or react with

carboxylic acid adsorbed to the InP surface to produce ethane (δ = 0.8 ppm) and desorbed metal carboxylate (sharp oleate resonance $\delta \sim 5.5$ ppm). (**Figure 3.5a**) Previous studies with CdSe QDs used $CdMe_2$ and $ZnEt_2$ to remove excess carboxylic acid and other acidic impurities and reported surface bound methyl groups along with free metal carboxylates and methane or ethane.[45] There is no change in the ^1H NMR spectra after the first spectrum is taken at 10 minutes, indicating the reaction has gone to completion by that time. Addition of $ZnEt_2$ up to 2 equivalents of total mmol of In (i.e. in excess of available surface sites) shows a combination of free $ZnEt_2$ and bound alkyl features around 0.2 ppm (**Figure 3.6**). This indicates that the reaction is self-limiting, a characteristic feature of half-reactions in ALD. After all the surface sites are consumed in the reaction with alkyl metal, the reaction no longer proceeds. When the reaction is completed, InP QDs remain colloidally stable in toluene and can be redissolved in other nonpolar solvents such as 1-octadecene. In order to remove any excess alkyl metal, the system was evacuated to complete dryness. At this step, it is important to note for safety that the cold traps should be removed with care and quenched appropriately.

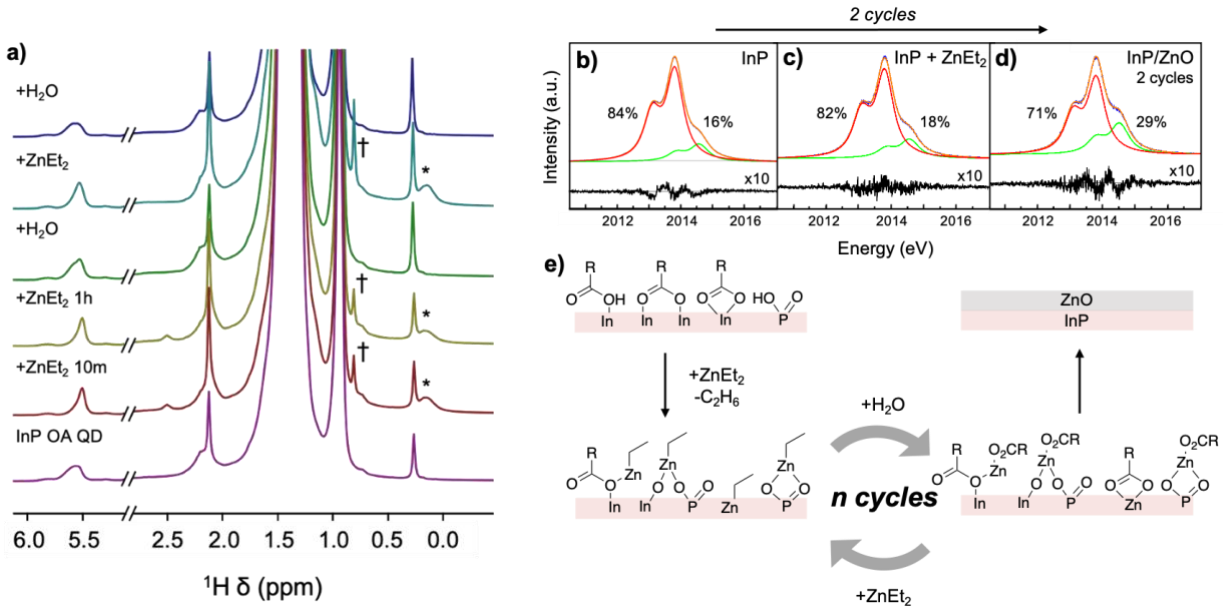

Figure 3.5. a) ^{1}H NMR showing the broad resonance of metastable surface bound ethyl groups (*) and the evolution of ethane (†) upon the self-limited reaction of $ZnEt_2$ with InP QD surface. The sharpening of alkene peak of oleate (δ ~ 5.6 ppm) indicates desorption of oleate which re-coordinates upon the addition of H_2O. b-d) Phosphorus XES spectra of InP QDs b) as-synthesized, c) after $ZnEt_2$ addition, and d) after one cycle of $ZnEt_2$ and H_2O addition, fit with a linear combination (orange) of phosphide (red) and phosphate (green) components with the percentage for each P oxidation state noted. The residual signal x10 trace after fitting is shown in black. e) Proposed scheme of the surface chemistry upon $ZnEt_2$ and H_2O addition cycles to InP QD surface for ZnO shell growth.

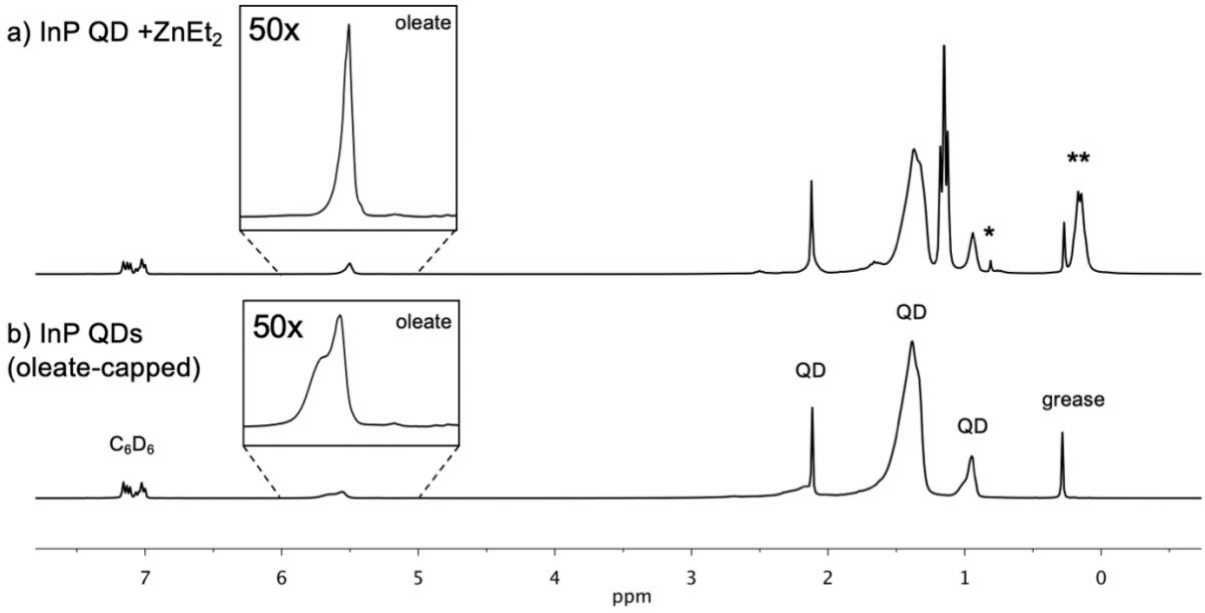

Figure 3.6. ^{1}H NMR spectra showing a) InP QD + 2 eq $ZnEt_2$ to total mmol of In (excess of available surface reaction sites) compared to b) native oleate-capped InP QDs. The addition of excess $ZnEt_2$ results in the evolution of ethane (*) and resonance that represents a combination of free $ZnEt_2$ and surface bound ethyl group around 0.2 ppm (**). Surface oleate ligands are also shown to be mostly unbound from the surface.

Upon re-dissolution of the surface-treated QDs in toluene, water was injected in the same molar equivalent as the alkyl metal and stirred at room temperature. To facilitate the injection of the sub µL volume, water was mixed with acetone and delivered in the desired amount via dilution. At this step, we no longer observed features associated with $ZnEt_2$ or the surface bound ethyl groups by ^{1}H NMR spectroscopy. Instead, the alkene region from oleate showed the presence of both bound oleate and unbound In or Zn carboxylate (bimodal peak between 5.4-5.7 ppm, **Figure 3.5a**). This trend in the alkene region was consistent throughout two cycles, where upon $ZnEt_2$ addition, metal carboxylates dissociate from the QD surface and become "free", while the addition of water partially re-coordinates the carboxylates back to the QD surface (**Figure 3.5a**). We

hypothesize that the re-coordination of oleate is due to the dynamic exchange and replacement from surface hydroxide which forms upon the reaction of surface alkyl and water. Upon completion of the reaction, evacuation and redissolution steps can be repeated to restart and continue the metal oxide shell growth cycles or the reaction can be halted at 1 cycle.

We probed the local environment of phosphorus in the metal oxide shelled InP QDs using Kα and Kβ P X-ray emission spectroscopy (XES). P XES is an especially useful tool for observing and quantifying P speciation and has been reported with InP-based QD systems.[18] P Kα XES shows that the addition of $ZnEt_2$ results in no change in P oxidation (**Figure 3.5b, c)**. After 2 cycles, the bulk fraction of oxidized P increases by 13% for ZnO (**Figure 3.5d**) Similar results were observed for CdO and GaO_x shells, where the addition of alkyl metal had negligible change in the P oxidation level and the addition of water to complete the cycle led to an increase in P oxidation (**Figure 3.7a-d**). The phosphate fingerprint in the Kβ at 2124 eV was consistently observed for all samples in agreement with the Kα data (**Figure 3.7e**) There is no oxidant present for P upon the addition of alkyl metal, resulting in no increase in the phosphate fraction. However, with the induction of shell growth using water, we start to observe an increase in P oxidation. Photooxidation from water on InP QD surface was previously reported to originate from O^{2-} forming interstitial defects in the lattice.[22]

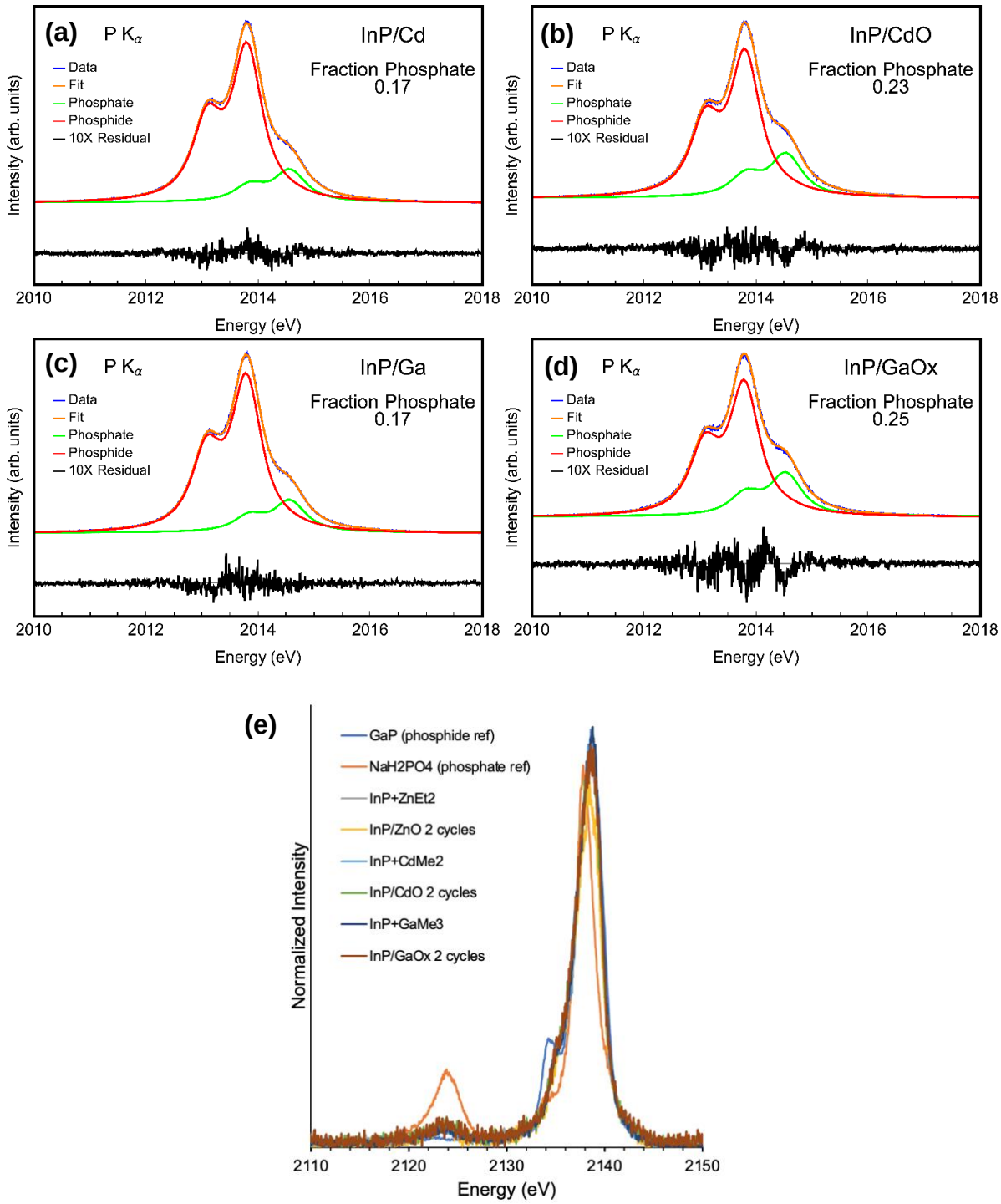

Figure 3.7. P Kα XES of InP QDs after a) $CdMe_2$ addition, b) one cycle of $CdMe_2$ and water addition, c) $GaMe_3$ addition, and d) one cycle of $GaMe_3$ and water addition. e) An overlay of Kβ XES of InP QDs shelled with ZnO, CdO, GaO_x showing the characteristic phosphate fingerprint at 2124 eV.

Figure 3.5e illustrates the representative scheme of the surface chemistry throughout the ALD-like reaction cycles for layer-by-layer growth of ZnO on the colloidal InP QD surface. The native surface of InP QDs is composed of In carboxylate ligands coordinated in a mixture of bridging, bidentate, and monodentate binding modes.[46,47] Some phosphate species are also expected to be present at the surface. The addition of $ZnEt_2$ strips off some of the bound oleate species from the surface shown by the ^1H NMR spectrum (**Figure 3.5a**) simultaneously as the surface bound ethyl groups appear. Zn ethyl species are proposed to be coordinating to surface P by replacing In carboxylate or to the surface phosphate, surface oxides or carboxylates coordinated to In. The proposed surface coordination environment is consistent with that previously elucidated for InP treated with divalent cation like Cd using solid-state dynamic nuclear polarization (DNP) NMR spectroscopy.[48] Free carboxylic acids that are not removed by purification and are in dynamic exchange with the surface bound carboxylates will also react with $ZnEt_2$ to evolve ethane and produce Zn ethyl carboxylate species that can coordinate to the InP QD surface. The addition of water shows evidence for re-coordination of oleate ligands and the desorption of the surface bound ethyl groups. This indicates that the oleates are now re-bound to the surface In or Zn by replacing the ethyl group and evolving ethane. We propose that repeating these cycles leads to colloidal layer-by-layer growth of metal oxide using InP QD surface as the substrate.

The evacuation steps between reagent additions are crucial for preventing independent nucleation of metal oxide and to ensure that the reaction is limited to the surface of the InP QDs. A significant excess of either reagent involved in the metal oxide growth can also result in the loss of colloidal stability and degradation of the QDs. At elevated temperature, grey precipitates formed which were confirmed to be Zn^0 particles by XRD (**Figure 3.8**). Therefore, rather than using precursors in excess and relying on the purging steps to remove excess throughout the continued

cycles, judicious amounts are employed at each addition as in successive ionic layer adsorption and reactions (SILAR). Furthermore, an attempt to grow thicker ZnO shells eventually crashed out the QDs after the addition of 6.2 eq ZnO (equivalent to 2 unit cell monolayer of ZnO on 3 nm diameter InP QD, refer to SI for details). The aggregates exhibited wurtzite phase ZnO with 6.4 nm diameter by Scherrer analysis and 4.3 nm by TEM (**Figure 3.9**). The loss of the zinc blende InP pattern suggests that a thicker ZnO shell has grown on the InP QDs, but these data do not explicitly rule out independent nucleation of wurtzite ZnO nanoparticles. This growth procedure for a thicker shell could be further optimized by adding extra ligands as previously demonstrated with $AlMe_3$ on wide range of NC systems.[28,29]

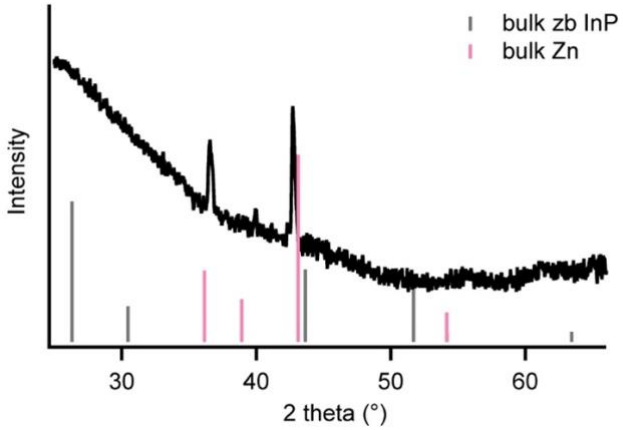

Figure 3.8. XRD pattern of the Zn^0 precipitates that formed upon heating up the reaction of InP QDs and excess $ZnEt_2$ to 200°C.

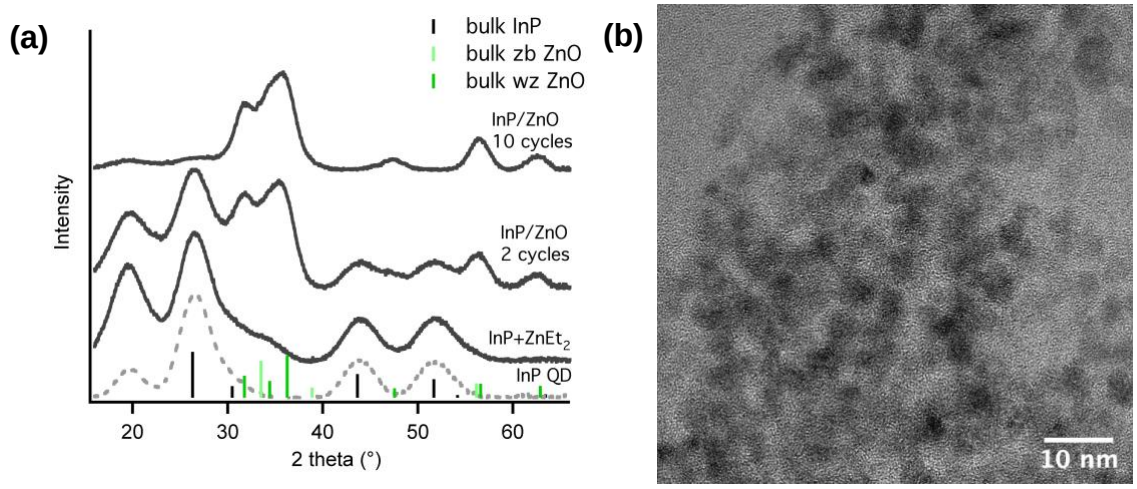

Figure 3.9. a) Stacked XRD patterns of InP QD core, InP QD + $ZnEt_2$, InP/ZnO after 2 cycles (1 eq ZnO to In), and InP/ZnO after 10 cycles (6.2 eq ZnO to In, expected to form ~1 ML ZnO shell). The particle size for InP/ZnO QD sample after 10 cycles was estimated to be 6.4 nm by Scherrer analysis. b) TEM image of InP/ZnO QD sample after 10 cycles. The particle size was measured to be 4.3 nm +/- 0.5 nm (152 particles). Formation of aggregates are evident from the TEM image which could be prevented by adding more carboxylic acid ligands to improve the colloidal stability.[29] InP (PDF #00-032-0452), zinc blende ZnO (PDF #03-065-2880), wurtzite ZnO (PDF #00-036-1451).

3.2.2.2 Bulk structural characterization

Typically for core/shell nanocrystals, the growth of the shell is evidenced in powder XRD by changes in the peak linewidth and shifts based on the weighted contribution of the core and shell lattice structures (taking into account scattering factors, where materials with smaller scattering factor contribute more weakly).[49] With a thin, one or sub-monolayer shell, peak broadening and minimal shifting toward the bulk pattern of the shell structure are expected. As the shell grows thicker, sharpening of the peaks and a shift towards the bulk pattern peak positions of the shell material prevail.

The powder XRD patterns were simulated using the DebyeByPy simulation package developed by Trigg.[50] The same optimized models of InP ($In_{77}P_{77}$) and metal oxide shelled InP structures ($In_{31}P_{31}/M_{46}O_{46}$, M = Zn, Cd, Ga, Al) (**Figure 3.10a**) from the DFT calculations were used. The simulated XRD pattern of $In_{77}P_{77}$ showed the characteristic (111), (220), and (311) peaks of bulk zinc blende InP with small shifts to lower angles for all peaks compared to the bulk pattern. With the metal oxide shell, all peaks generally appear to broaden, decrease in intensity, and shift to higher angles. The simulated patterns for metal oxide shelled InP QDs show distinct patterns from each other, and the new features and peak broadening for each case are consistent with zinc blende or cubic patterns of the respective metal oxide. Notably, these observations from $In_{31}P_{31}/M_{46}O_{46}$ structures were different from those shown by the $In_{31}M_{46}P_{77}$ structures, where only shifts in the peaks were observed towards higher angles as expected based on the smaller size of the metal cations, which result in lattice contraction (**Figure 3.11**).

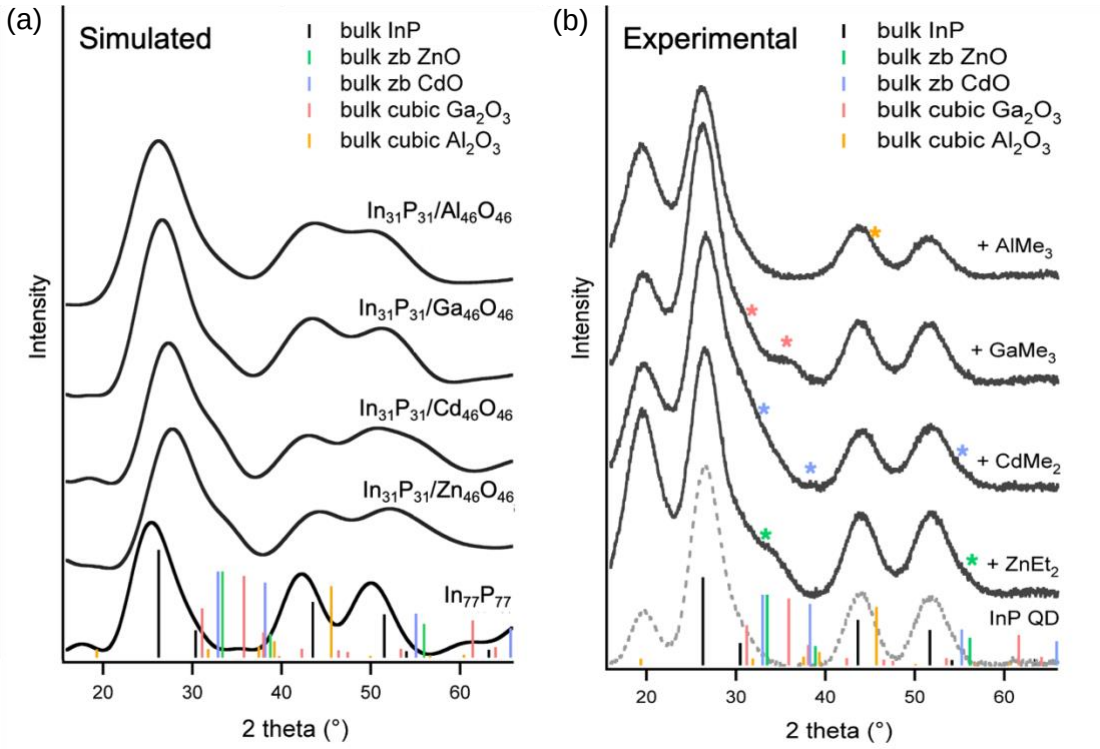

Figure 3.10. a) Simulated and b) experimental XRD of $In_{31}P_{31}/M_{46}O_{46}$ structures and InP QDs treated with alkyl metal, respectively. The simulated patterns show appearance of new broad features that are consistent with the zinc blende or cubic lattice patterns of the metal oxide and with the experimental data. The relevant peak positions from each of the bulk metal oxide pattern is indicated with the asterisks (*) over the experimental XRD data. InP (PDF #00-032-0452), ZnO (PDF #03-065-2880), CdO (PDF #00-005-0640), Ga_2O_3 (PDF #00-006-0529), Al_2O_3 (PDF #00-050-0741).

Thin metal oxide shells on InP QDs generally exhibited the cubic phase of the metal oxide, which appeared as broad peaks in the powder XRD patterns (**Figure 3.10b**). Besides the zinc blende InP pattern from the core, additional peaks corresponding to cubic phase metal oxide arose as early as the first addition of the alkyl metal where no change in the particle size was observed by TEM (**Figure 3.12**). These peaks are notable at 34° for $ZnEt_2$ treatment, 33° for $CdMe_2$, and

31° and 36° for $GaMe_3$. In addition to the new peaks, peak broadening and increased intensity for zinc blende InP peaks at 44° and 52° for (220) and (311) facets were also observed. For example, after 2 cycles of CdO shell growth, the peak centered around 52° for (311) facet of zinc blende InP was observed to broaden and increase in relative peak intensity coinciding with the zinc blende CdO (220) facet peak at 55° (**Figure 3.13a**). Similarly, after two cycles of AlO_x, the peak centered around 44° showed relative broadening and increase in intensity which may be attributable to the (400) facet in the bulk aluminum oxide pattern at 46°. However, due to the loss of colloidal stability of the QDs after 2 AlO_x cycles (**Figure 3.12h, Figure 3.13c**), it is difficult to discern from the acquired spectra or to attempt to gain more information by continuing the shelling process. It is still notable however that additional peaks that arise for other thin shells of metal oxides are not present for AlO_x shell where no high intensity peaks other than at 46° are expected. The broad peak around 20° that appears for all samples is indicative for the surface organic ligands, with density, ordering, and ligand length all contributing to the peak intensity and linewidth.[52] The observation of bulk metal oxide patterns emerging as early as the first addition of alkyl metal as evidence for thin metal oxide shelling suggests that the native surface oxides of InP QDs are involved and necessary component in the formation of the metal oxide.

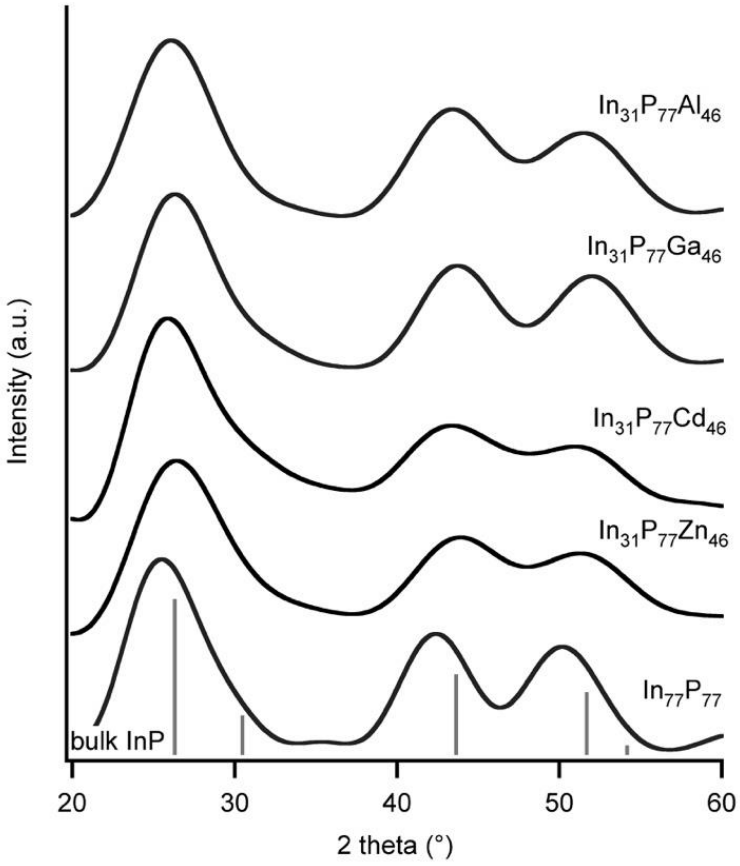

Figure 3.11. Simulated XRD patterns of optimized $In_{31}P_{77}M_{46}$ structures.

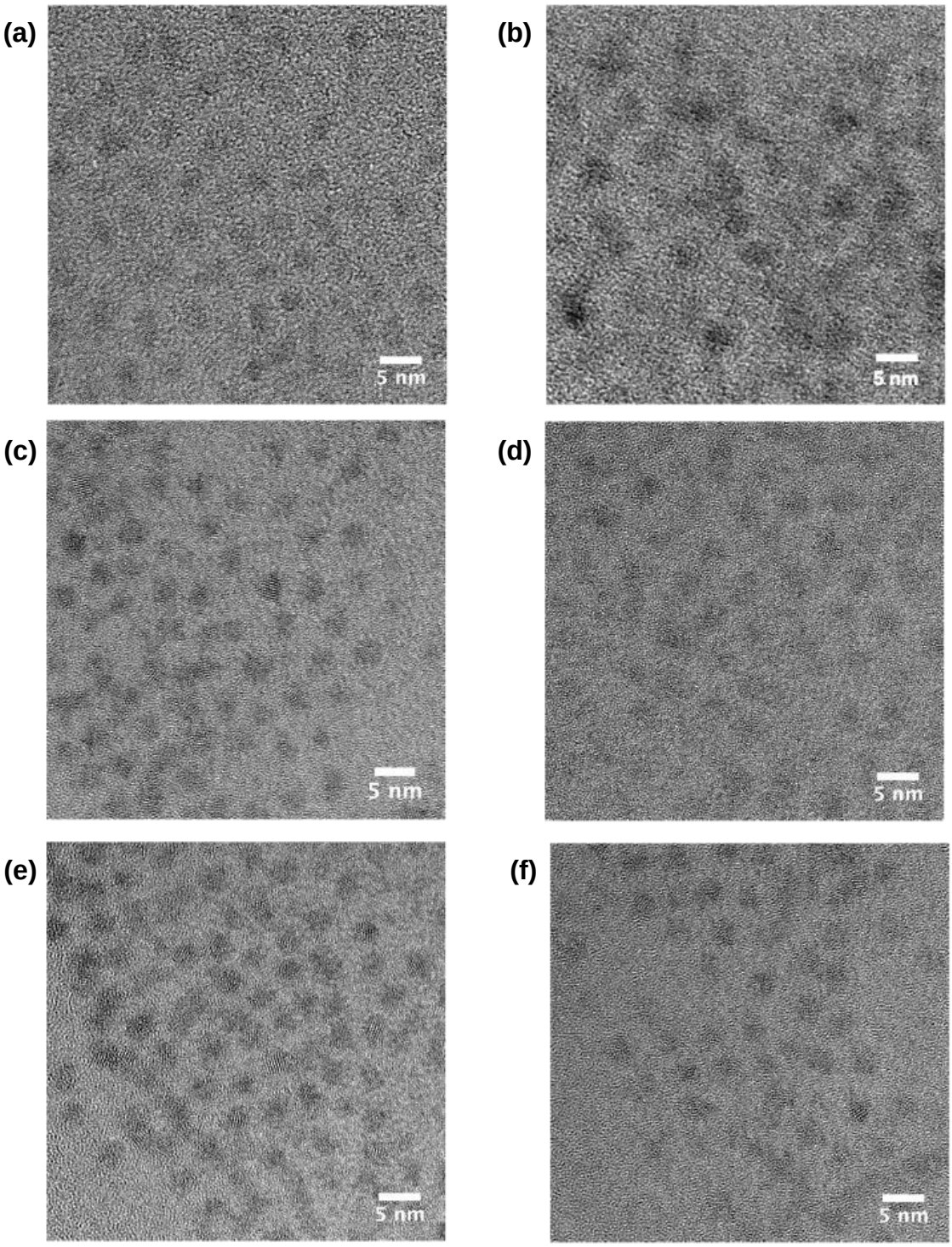
(a)
5 nm
(b)
5 nm
(c)
5 nm
(d)
5 nm
(e)
5 nm
(f)
5 nm

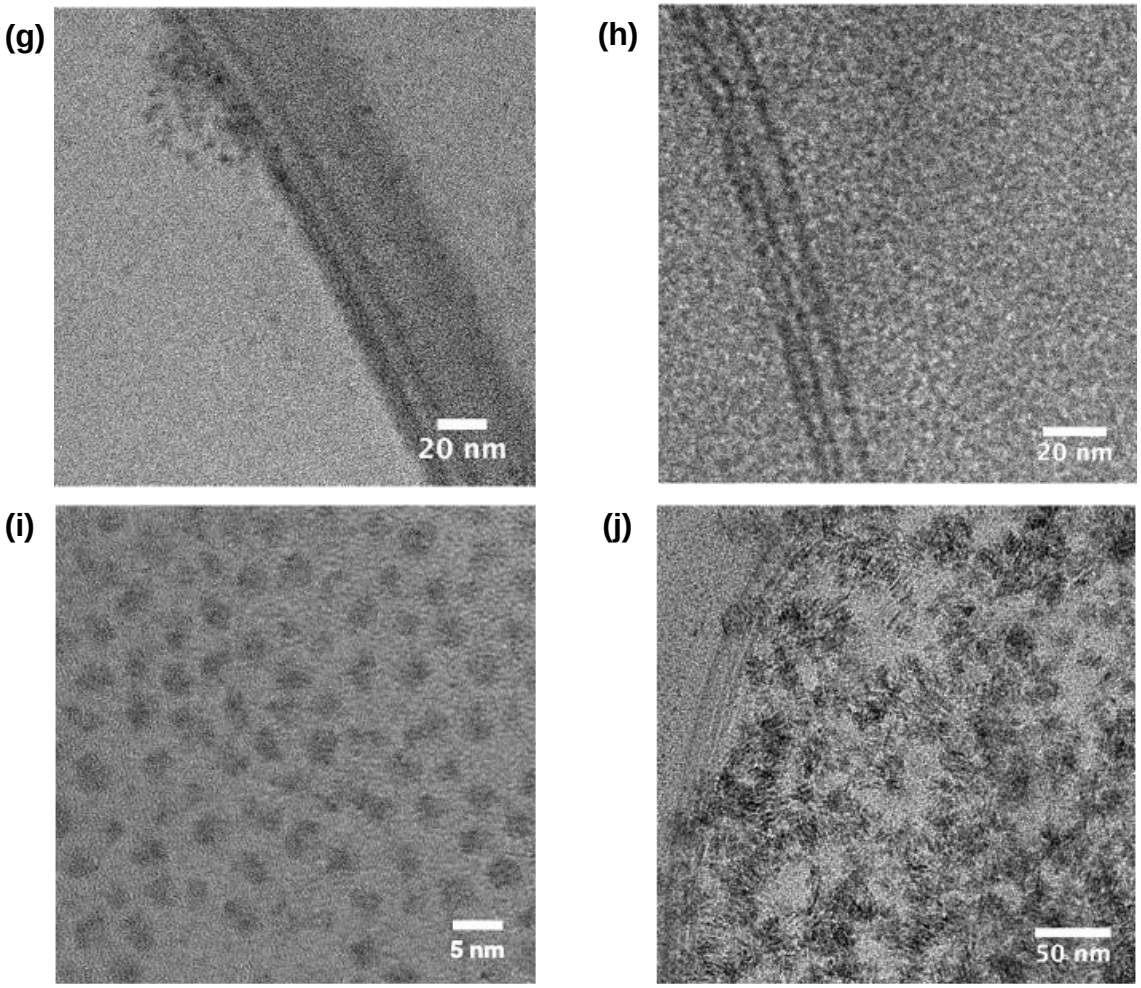

Figure 3.12. TEM images of a) InP + $ZnEt_2$ (3.0 nm +/- 0.4 nm), b) InP/ZnO 2 cycles (3.7 nm +/- 0.5 nm), c) InP + $CdMe_2$ (3.0 nm +/- 0.4 nm), d) InP/CdO 2 cycles (3.4 nm +/- 0.4 nm), e) InP + $GaMe_3$ (3.0 nm +/- 0.3 nm), f) InP/GaO_x 2 cycles (3.6 nm +/- 0.5 nm), g) InP + $AlMe_3$, h) InP/AlO_x 2 cycles, i) InP + $InMe_3$ (3.2 nm +/- 0.5 nm), and j) InP/InO_x 2 cycles. For AlO_x samples, insufficient number of particles were able to be imaged due to aggregates from the reaction. InP/InO_x sample after 2 cycles formed different crystalline structures that appeared to be more dominant phase besides ~3 nm nanocrystals.

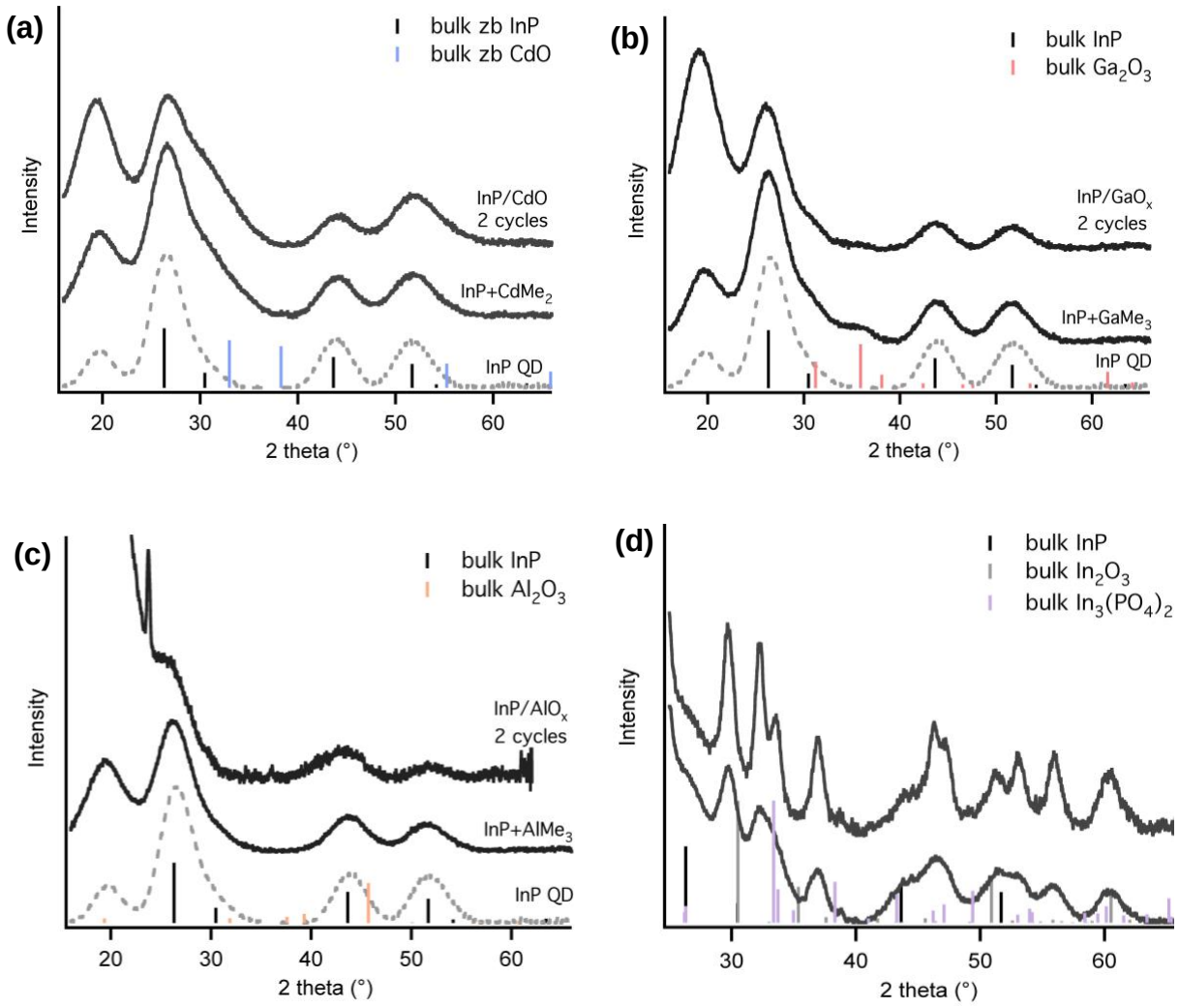

Figure 3.13. XRD patterns comparing InP QD, after alkyl metal addition, and after 2 cycles of alkyl metal and water addition for a) Cd, b) Ga, c) Al, and d) In. InP (PDF #00-032-0452), CdO (PDF #00-005-0640), Ga_2O_3 (PDF #00-006-0529), Al_2O_3 (PDF #00-050-0741), $In_3(PO_4)_2$ (PDF #04-010-1920).

Indication of metal oxide shell growth is observed between the first alkyl metal addition and after 2 cycles of alkyl metal and water additions for CdO and GaO_x shelled InP QDs (**Figure 3.13a, b)**. The changes in the XRD pattern suggesting growth were consistent with the increased

particle size observed by TEM (**Figure 3.12c-f**). The increase in the QD size was measured to be around 0.7 nm after two cycles for ZnO, 0.4 nm for CdO, and 0.6 nm for GaO_x accounting for approximately 0.5 unit cell monolayers. The increase in size is observed without change in the QD morphology or core stoichiometry (**Table 3.7**). As expected, the ratio of metal introduced by alkyl metal relative to In increases between the first and the second cycle. Across all the samples, the cation (In, M) to anion (P) ratio was between 2.4 to 5.3, suggesting that oxidic species are incorporated in the structure.

Table 3.7. The elemental compositions of InP and InP/MO_x QDs obtained from ICP-OES. The molar ratios are normalized to moles of P. The ratio of total metal atoms to P is noted.

	In	P	Zn	Cd	Ga	Al	M:P
InP QD	**1.5**	**1**					
+$ZnEt_2$	**1.6**	**1**	**1.1**				**2.7**
ZnO x2	**1.6**	**1**	**3.5**				**5.1**
+$CdMe_2$	**1.7**	**1**		**0.7**			**2.4**
CdO x2	**1.7**	**1**		**1.6**			**3.3**
+$GaMe_3$	**1.6**	**1**			**1.2**		**2.8**
GaO_x x2	**1.7**	**1**			**2.5**		**4.2**
+$AlMe_3$	**1.3**	**1**				**1.9**	**3.2**
AlO_x x2	**1.5**	**1**				**3.8**	**5.3**
+$InMe_3$	**3.2**	**1**					**3.2**
InO_x x2	**5.1**	**1**					**5.1**

What's interesting to note about the growth of cubic phase gallium oxide is that while various polymorphs of gallium oxide are known such as rhombohedral (α), monoclinic (ß), defective spinel (γ), or orthorhombic (ε), growth of cubic (δ) phase Ga_2O_3 thin film has yet to be

reported.[52] Given that substrate lattice and growth temperature are the most important in determining the formation of a particular gallium oxide polymorph[52], we hypothesize that the zinc blende InP core served as a template for cubic phase metal oxide growth at monolayer to submonolayer shell thickness. Similar phenomena have been previously reported in QD systems where the crystal structure of HgS interlayer and the outer CdS shell was dictated by the wurtzite CdSe core in layer-by-layer shell growth.[30] Preferential growth in one facet over the others in XRD may additionally explain why not all peaks are represented in the thin metal oxide shelled InP QDs.

In the case of the ZnO shell on InP QDs, the growth of zinc blende ZnO peaks is evident in the XRD upon the first addition of diethyl zinc. After two cycles of ZnO deposition, the wurtzite phase ZnO pattern appears, which is the more accessible and thermodynamically favored phase of ZnO (**Figure 3.9a**). Similar to cubic phase Ga_2O_3, the growth of zinc blende ZnO is instigated using the zinc blende InP core as a template for growth, after which the wurtzite lattice prevails. Unlike the CdO and GaO_x shells where a more gradual increase in peak intensity and broadening were observed, the appearance of more distinct and sharper peaks of wurtzite phase ZnO suggests independent nucleation of ZnO nanoparticles in addition to ZnO shell growth on InP QDs.

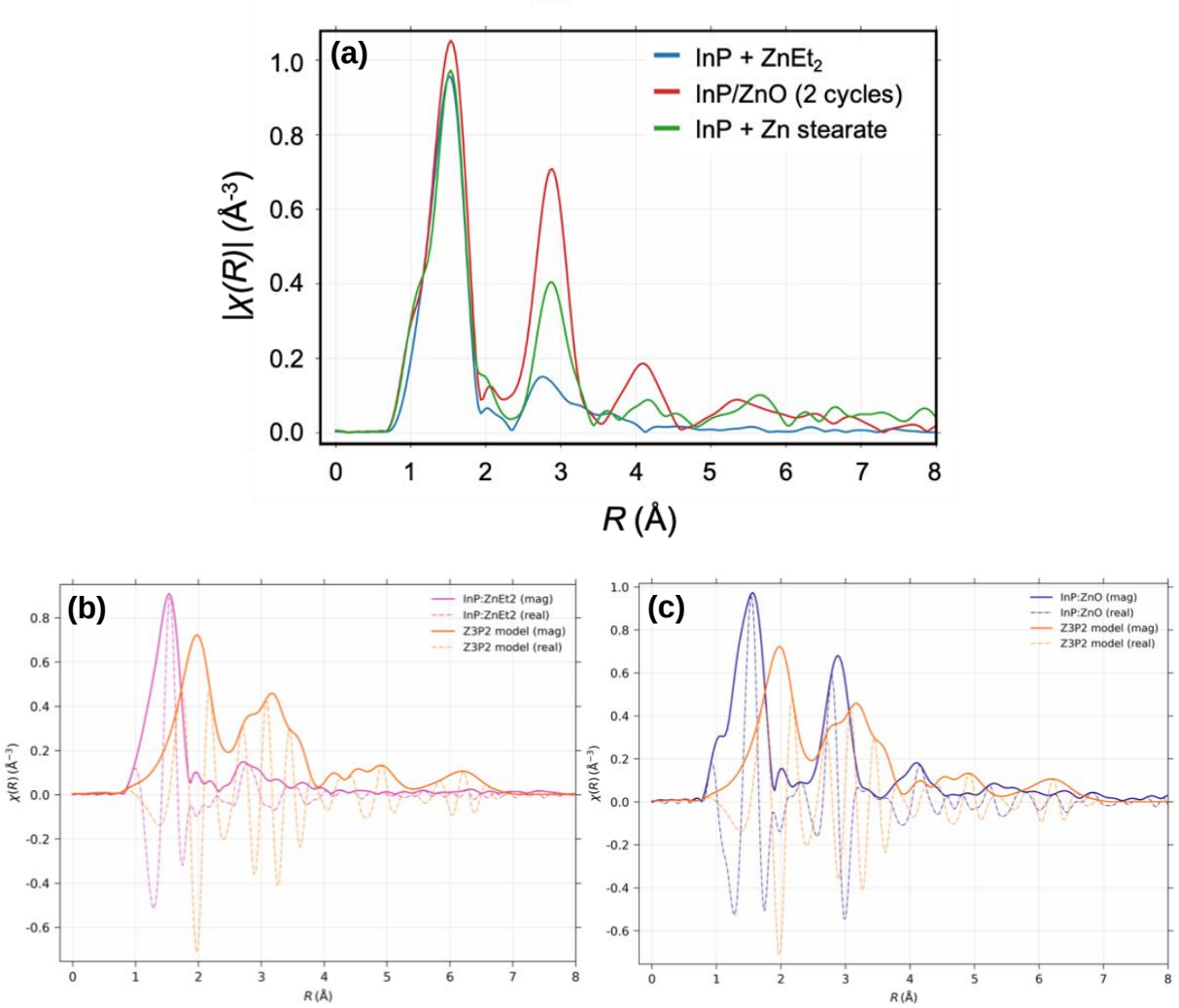

Figure 3.14. a) Zn K-edge EXAFS showing Zn-O environment around R ~1.3 Å for all InP+$ZnEt_2$, InP/ZnO after 2 cycles, and InP treated with Zn stearate. The difference in peak amplitude for the second coordination shell around R ~2.9 Å suggests higher uniformity and/or narrow distribution of bond lengths for the InP/ZnO (2 cycles) sample, and low amplitude for InP+$ZnEt_2$, with the InP+Zn stearate sample coming in in between. Zn K-edge fitting with Zn-P for b) InP QDs treated with ZnEt2 and c) ZnO shelled InP QDs.

We further probed the local Zn bonding environment using Zn K-edge extended X-ray absorption fine structure spectroscopy (EXAFS). From the first addition step of diethyl zinc, the

presence of Zn-O bond is evident around R ~1.3 Å from fitting the bulk ZnO in the real space which is consistent with our conclusion that the alkyl metal treatment alone instigates the deposition of a thin metal oxide shell on InP QDs (**Figure 3.14a**). The same peak is present in both InP/ZnO QD sample after two cycles and InP QD sample treated with Zn stearate showing good overlap with the Zn-O peak from InP treated with $ZnEt_2$. There is no direct evidence of Zn-P bonding from the EXAFS data as the best fit was observed for the Zn-O only model rather than a model incorporating a combination of Zn-O and Zn-P, suggesting that the Zn-P bond environment represents less than 10% (detection limit for this measurement) of the total Zn primary coordination sphere (**Figure 3.14b, c**). This is consistent with the overall picture emerging across the data and captured schematically in **Figure 3.5e**.

The second coordination shell (R ~2.9 Å) does not provide a good fit with Zn-Zn scattering path by itself and is difficult to fit with confidence without prior knowledge of the scattering path that is present. The clear differences in peak amplitudes that emerge between the different samples allow for quantitative understanding from the knowledge that the amplitudes of the Fourier transformed EXAFS are correlated to the coordination number of Zn atoms and the bond length distribution. After two cycles, the Zn atoms have, on average, more second shell neighbors compared to when only $ZnEt_2$ is added, implicated by the greater peak amplitude. Also suggested from this sample about the Zn atoms in the second coordination shell is that they may have higher uniformity and/or a narrower distribution of bond lengths, resulting in a more well-defined peak with a greater amplitude. Upon comparing these structures with Zn carboxylate capped-InP QDs, we found that the coordination shells of Zn carboxylate capped-InP QDs display Zn coordination environments somewhere in between the other two samples. If the surface environment and passivation provided by Zn carboxylate are effective at PL increase but easily removed by further

surface manipulations, our approach of layer-by-layer deposition of metal oxide may provide a solution for epitaxial growth and careful control of the surface and electronic structure. The composition of these QDs were also investigated by energy dispersive X-ray spectroscopy (EDX) where co-localization of In and Zn was observed. For this, it was important due to the instability of the particles under intense electron beam that the particles were shelled with silica for stable imaging conditions (**Figure 3.15**). Whether wurtzite ZnO nanoparticles were independently nucleated or deposited on InP QDs as a highly crystalline shell remains inconclusive, and this data may suggest both processes are occurring simultaneously.

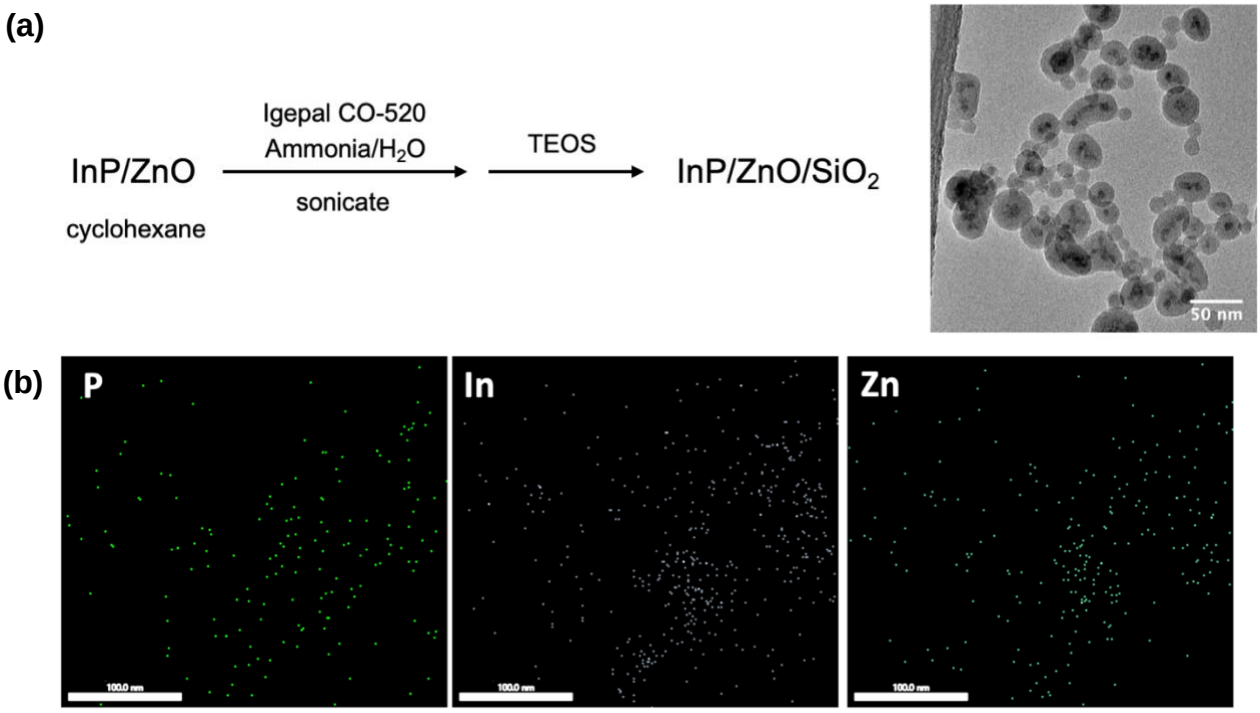

Figure 3.15. a) Reaction scheme for silica shelling of InP/ZnO QDs. b) EDS mapping of InP/ZnO QDs shelled with silica which shows co-localization of In and Zn.

Anomalous results were observed from an attempt to shell InP QDs using $InMe_3$ with a thin, conformal layer of indium oxide. Unlike other alkyl metals, the addition of $InMe_3$ resulted in

the appearance of sharp and distinct peaks immediately in the powder XRD pattern (**Figure 3.13d).** Some peaks conceivably correspond to $In_3(PO_4)_2$, suggesting a surface that can be described as oxyphosphate or polyphosphate. Other reagents should be explored for layer-by-layer shelling of In_2O_3. Furthermore, sharp peaks from the crystal pattern of long chain hydrocarbon (paraffin) were evident in samples that were not purified by gel permeation chromatography (**Figure 3.16**). This could simply be avoided by purification via gel permeation chromatography for the removal of ODE and other impurities. Adventitious crystallization of long chain carboxylates is likely affecting the surface chemistry and embedding in the ligand shell.

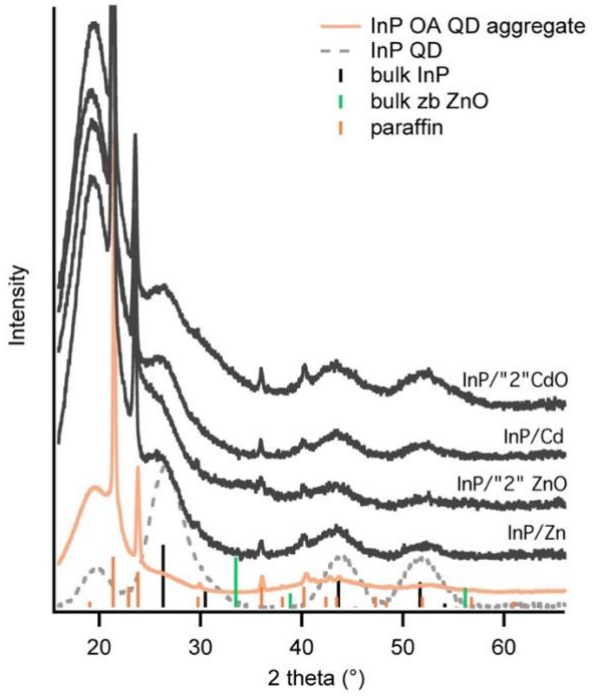

Figure 3.16. XRD pattern showing patterns of paraffin in the resultant QDs when the InP QDs are insufficiently purified (gel permeation chromatography step absent) prior to the reaction with alkyl metal or subsequent cycles of metal oxide shelling.

3.2.2.3 Optical properties

Changes in the optical properties were observed at each step of layer-by-layer shelling of metal oxide on InP QDs. While the absorption feature remains fixed or shows changes of a few nm throughout the addition cycles, modest increases in the PL or PL quenching are observed with the first alkyl metal addition step (**Figure 3.17**). Following the PL intensity throughout 2 addition cycles of ZnO, we correlated quenching of PL with the carboxylate being stripped off from the InP QD surface and recovery of PL with the re-coordination of the carboxylate in tandem with the ^{1}H NMR results discussed earlier. Literature precedent for conventional ALD on InP QD films reported quenching of PL with alkyl metal and then recovery of PL upon addition of water.[53] At the completion of the second cycle, significant quenching was observed for both ZnO and CdO shelled InP QDs, while the sample treated with $GaMe_3$ and water maintained higher PL intensity than the original InP QD sample. The lattice mismatch between the metal oxide shell and InP core may be an important factor to consider here (a = 0.463 nm for zinc blende ZnO, 0.470 nm for zinc blende CdO, and 0.587 nm for zinc blende InP). Previous studies examining the reaction of alkyl metal reagents with CdSe QDs have reported on the effect of photoinduced absorption bleach as a signature for n-doping by alkyl radicals.[45,54] In our case, we did not observe photoinduced doping, but instead under ambient light, the surface alkyl groups were intact and likely in dynamic exchange with the free carboxylates.

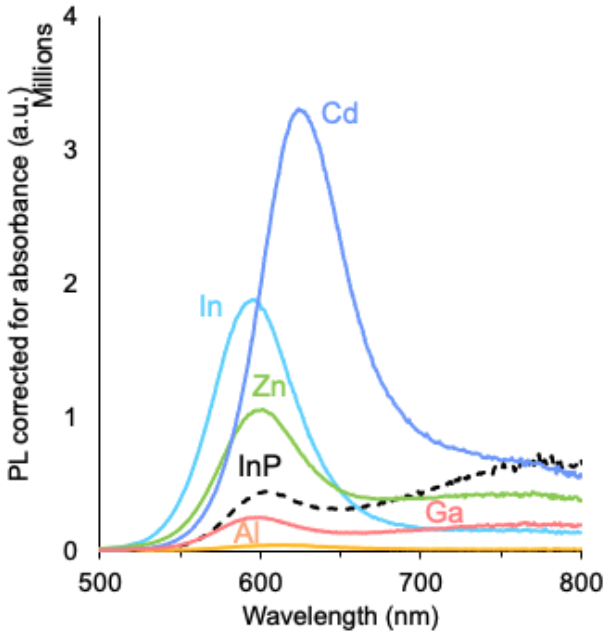

Figure 3.17. PL of InP QD treated with alkyl metals (M = Zn, Cd, Ga, Al, In)

3.2.3 *Effect of MO_x interface in InP/ZnSe core/shells*

Next, we explored the impact of these controlled metal oxide interfaces on the optoelectronic properties of InP/ZnSe core/shell QDs. We were interested in ZnO and GaO_x shells in particular for their PL properties after the treatment with alkyl metal and previous studies on various Zn- and Ga-based interlayers in InP/Zn(S,Se) core/shell systems.[10,55,56] A thin shell of ZnSe was applied at 1.5 eq Zn and 0.8 eq Se to mmol In on InP QD cores treated with diethyl zinc or trimethyl gallium. Previously, a thin shell of ZnSe was shown to increase the QY of InP significantly, which was then isolated for purification and reconstituted for subsequent thicker shell growth that resulted in near-unity QY InP-based QDs.[7] In the case of thin ZnSe-shelled InP QDs with ZnO or GaO_x interlayers, we observed improved linewidths from 230 meV to 215 meV for the GaO_x interface system, while an increase in PL QY was observed for the ZnO interface QDs (**Figure 3.18a**) from 22% to 33% when compared to the control InP/ZnSe QD sample. While

InP/ZnO/ZnSe QDs showed fixed PL max compared to InP/ZnSe, InP/GaO_x/ZnSe QDs was redshifted by 21 nm. To further probe these systems, we measured P oxidation by P XES (**Figure 3.19, Figure 3.20**). ODE-Se was used as the Se precursor in the synthesis to avoid convolution from additional P oxidation from TOP-Se. It is interesting here to note that the increase in PL QY in InP/ZnO/ZnSe QDs is accompanied by a minimal decrease in the P oxidation (8% vs. InP/ZnSe) but the reduction in the linewidth of 15 meV shown by InP/GaO_x/ZnSe QD sample is accompanied by a more significant decrease in the P oxidation by 18%. This may suggest that while the oxidative species are having a beneficial role in electronic confinement of the InP core, resulting in increased PL QY, effective control of P oxidation during shell growth is needed to minimize linewidth broadening. We hypothesize that the observed improvement in P oxidation in the case of the GaO_x interface may be the result of larger kinetic barriers associated with ion diffusion in this system. The thermodynamic favorability for Ga-P bond over Ga-O bond was previously considered in developing a rationale for the unexpected result where Ga as a dopant was calculated to be favoring internal and bulk sites of InP magic-sized cluster lattice unlike heterovalent dopants such as Cd and Zn that preferred surface sites.[57] The role of Ga may be important in preventing P migration into the ZnSe shell that coincides with the modest narrowing of the linewidth. In a previous study, a subpopulation of In and P atoms incorporating into the ZnSe shell were measured by EDS, implicating such structural defects will have detrimental effects on the optical properties.[58] This highlights the important consideration for a well-controlled interface of the core/shell that connects our understanding of the chemical structure at the atomic level with the resultant PL properties such as the linewidth.

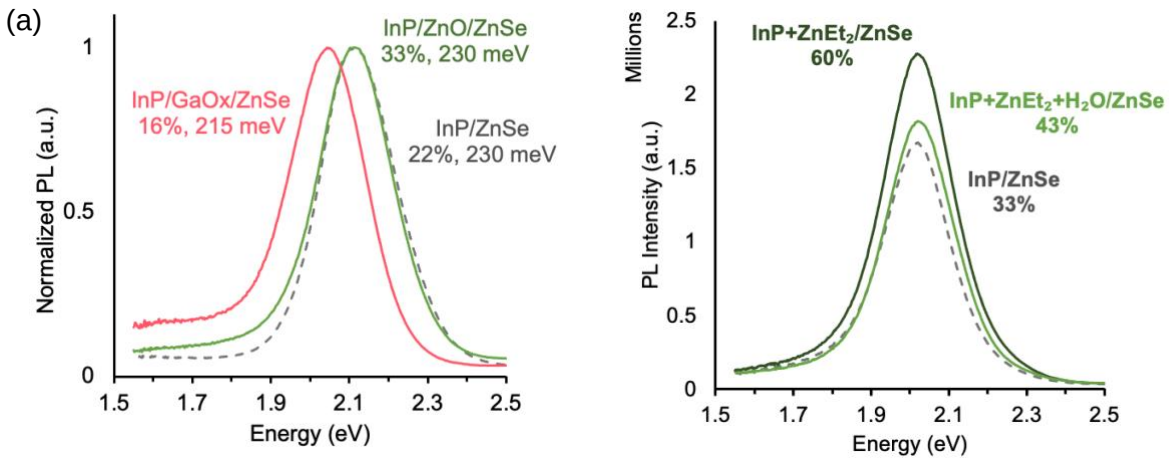

Figure 3.18. a) Normalized PL of InP/ZnSe, InP/ZnO/ZnSe, and InP/GaO_x/ZnSe with thin ZnSe shells to compare their emission linewidths, and b) relative PL and PL QY of InP/ZnSe, InP treated with $ZnEt_2$ prior to ZnSe shelling, and InP treated with $ZnEt_2$ and water prior to ZnSe shelling with thicker ZnSe shells. The shell grown here used 5 eq ZnSe to mmol In and is expected to have a ~2 unit cell monolayer thickness.

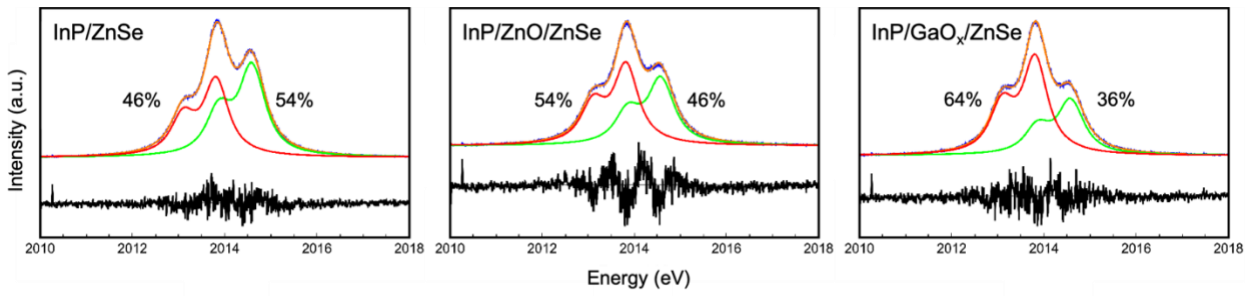

Figure 3.19. Phosphorus XES of InP/ZnSe, InP/ZnO/ZnSe, and InP/GaO_x/ZnSe showing the phosphide and phosphate components that make up the linear combination of the data and fit. ODE-Se was used as the Se precursor in the synthesis to avoid convolution from additional P oxidation from TOP-Se.

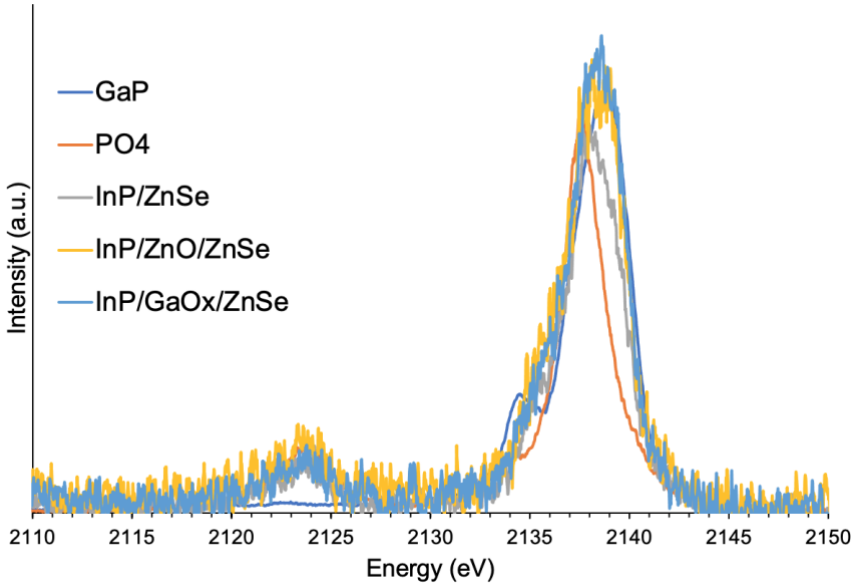

Figure 3.20. P Kβ XES of InP/ZnSe core/shell QDs with ZnO and GaO_x interface. Phosphate fingerprint around 2124 eV appears for all samples.

Additionally, we grew thicker shells of ZnSe on InP QDs with a ZnO interface. ZnSe shells at 5 eq to InP QDs were treated with either $ZnEt_2$ or one full cycle of metal oxide growth (i.e., $ZnEt_2$ and water). We observed more significant increase in the PL for those with metal oxide growth at the interface (**Figure 3.18b**), from 33% PL QY for InP/ZnSe to 60% with $ZnEt_2$ treatment and 43% with one full cycle of ZnO growth. With the improvement in the PL QY noted, the synthesis could use more optimization. A well-engineered band gap has been shown to repress Auger processes by delocalizing the wavefunction and softening the confinement potential (quasi-type-II) and a thick inorganic shell can be critical in solving blinking.[9,36,59] In type-I system, compositional gradient shells have been effective in smoothening out the interfacial wavefunction potential.[3] Leveraging well-controlled oxidic surface defects and various metal oxides at the interface and at the outermost shell layer could be new avenues to pursue in fabrication of bright InP based QDs.

3.3 CONCLUSIONS

In this work, we have explored how the identity of the metal oxide interface impacts emissive properties and stability of InP QDs using a combination of synthesis, DFT modelling, and physical and electronic structure characterization. Conventional ALD precursors can be used in a colloidal system for a facile, room-temperature growth of metal oxide shells on InP QDs in a layer-by-layer fashion to control the QD surface and interfaces with the goal of better controlling the optoelectronic properties of InP-based QDs. Our data support the formation and growth of ZnO, CdO, and GaO_x shells on InP QDs using this strategy. Interestingly, the first alkyl metal addition step alone forms a thin metal oxide shell, which we hypothesize to be due to the surface oxides already present in InP QDs. Surface oxide defects in InP QD systems are challenging to control or study, and this work contributes to our understanding of the impact of various metal oxide surfaces on InP QDs and how to leverage this for structural complexity and improved optoelectronic properties of InP QDs. With more optimization, the use of metal oxides as interfaces in core/shell systems and as outer coating layers can be further explored for charge injection, extraction, and transport applications.

3.4 EXPERIMENTAL

3.4.1 *General considerations and materials*

All glassware was dried in a 160 °C oven overnight prior to use. All reactions, unless otherwise noted, were performed under an inert atmosphere of nitrogen using a glovebox or using standard Schlenk techniques. Indium acetate (99.99%), anhydrous oleic acid (≥99%), myristic acid (≥99%), anhydrous acetonitrile (99.8%), diethyl zinc (52 wt% based on Zn), trimethyl aluminum (97%) were purchased from MilliporeSigma and used without further purification. Zinc stearate

(tech grade), and selenium powder (99.99%) were purchased from MilliporeSigma and dried before use. Dimethyl cadmium (97%), trimethyl indium (98%), and trimethyl gallium (≥99%) were purchase from Strem and used without further purification. *Caution: dimethyl cadmium is extremely toxic and pyrophoric and should be handled with caution and with special care in waste disposal, Diethyl zinc, trimethyl aluminum, trimethyl gallium, and trimethyl indium are pyrophoric and should be handled with caution*. Toluene was purchased from MilliporeSigma, collected from a solvent still and stored over activated 3 Å molecular sieves in a glovebox. Acetone (HPLC grade) was purchased from Fisher and used as purchased. 1-Octadecene (1-ODE, 90%) was purchased from MilliporeSigma, dried over CaH_2, distilled, and stored over activated 3 Å molecular sieves in a nitrogen atmosphere glovebox. C_6D_6 was purchased from Cambridge Isotope Laboratories and was similarly dried and stored. Bio-Beads S-X1 for gel permeation chromatography were purchased from Bio-Rad Laboratories and dried under vacuum at elevated temperature before being stored in a glovebox. Omni Trace nitric acid was purchased from MilliporeSigma and used without further purification. Hydrogen peroxide (30%, ACS grade) was purchased from Fisher and used as purchased. 18 MΩ water was collected from MilliporeSigma water purification system. $P(SiMe_3)_3$ was prepared by modifying a literature procedure in which sodium naphthalene was used in place of Na/K alloy.[60] *Caution: $P(SiMe_3)_3$ is a highly pyrophoric liquid that may form toxic phosphine gas upon reaction with air or water and should be handled with caution and care.*

3.4.2 *Synthesis of InP QDs*

Myristate or oleate-capped InP QDs were synthesized from myristate or oleate-capped InP magic-sized clusters (MSC) following a modified preparation.[41,61] Briefly, InP clusters (200 mg myristate MSC or 234 mg oleate MSC, 0.012 mmol) were dissolved in 5 mL of 1-ODE and hot-injected into a flask containing 35 mL of 1-ODE at 300 °C. The growth of the nanocrystals was

monitored by UV-vis spectroscopy until the absorbance maximum no longer redshifted and was halted between 40-60 min. Once the reaction was complete, the heating mantle was removed to cool down the solution flask. To start purification, 1-ODE was removed by vacuum distillation, and the resulting nanocrystal paste was transferred into a glovebox for precipitation/redissolution cycles using toluene and acetonitrile as solvent and anti-solvent, respectively. For further purification, the QD solids were dissolved in toluene and purified twice using gel permeation chromatography in a glovebox following literature procedures.[44,62] Purified InP QDs were dissolved in ~10 mL of toluene and stored as a stock solution in a glovebox. The absorbance value for 100 µL in 3 mL toluene was found to be 0.197 for 7 mL of stock solution containing 0.04 mmol In and used to calculate QD stock concentration.

3.4.3 *Colloidal ALD-inspired metal oxide (MO_x) shelling of InP QDs*

From a stock solution of InP QDs, a volume containing 0.04 mmol In was transferred to a vial. More toluene was added to make a total of 2 mL solution. 2 µL of $ZnEt_2$ (0.02 mmol) was added. After stirring at room temperature for 1 hour, the reaction was evacuated to complete dryness. To continue on the growth cycle with water addition, the QDs were re-dissolved in toluene and brought outside of the glove box in a syringe sealed with a septum. The QDs were injected into a 15 mL round bottom flask on the Schlenk line. Water and acetone were mixed at 1:7 ratio to facilitate injection of water at sub-microliter volume. This specific ratio additionally allows the injection of the same volume as $ZnEt_2$ for equimolar amounts. After stirring at room temperature for 1 hour, the reaction was again evacuated to complete dryness. To continue growth, these steps were repeated for addition of $ZnEt_2$ and water (refer to Text S1 for the calculation of addition equivalents taking into account the increase in volume). For the growth of cadmium oxide, gallium oxide, aluminum oxide, and indium oxide, 0.02 mmol of $CdMe_2$, $GaMe_3$, $AlMe_3$, and $InMe_3$ were

added respectively. Note that $InMe_3$ is a solid at room temperature and can be added to the reaction accordingly. The reaction can be halted at any point in the growth cycle by evacuating the system and discontinuing further additions.

3.4.4 *Synthesis of InP/ZnSe QDs and InP/MO_x/ZnSe QDs*

Thin shelling of ZnSe was adapted from a literature preparation method.[7] From a stock solution addition on of InP QDs, a volume containing 0.1 mmol In was transferred to a vial and dried under reduced pressure. The QD solids were redissolved in 3 mL of 1-ODE, injected into an evacuated flask, and brought up to 270 °C while stirring. Zinc stearate (95 mg, 0.15 mmol, suspended in 0.5 mL of 1-ODE) was injected and stirred for 10 min. ODE-Se (400 µL, 0.08 mmol, from 0.2 M stock solution) was added and the reaction temperature was maintained at 270 °C. The reaction was monitored by UV-Vis and PL spectroscopy and halted after 20 min. For thicker shelling (5 eq ZnSe to In) adapted from literature method[63], a volume of InP QD stock containing 0.04 mmol In was dried down and re-dissolved in 2 mL 1-ODE. Zinc stearate (126 mg, 0.2 mmol, suspended in 1.5 mL of 1-ODE) was injected and stirred for 40 min at 220°C. TOP-Se (200 µL, 0.2 mmol, from 1.0 M stock solution) was added, and the reaction temperature was raised to 300 °C. After 60 minutes, the reaction flask was cooled to room temperature, 1-ODE was removed by vacuum distillation. The reaction flask was transferred into a glovebox for precipitation/redissolution cycles using toluene and acetonitrile as solvent and anti-solvent, respectively.

InP/ZnSe QDs with metal oxide interface were prepared following the same steps for making InP/ZnSe QDs, after the QDs were treated with alkyl metal or 1 cycle of alkyl metal and water. QD solids were redissolved in 3 mL of 1-ODE and injected to an evacuated flask to start ZnSe shelling as described above.

3.4.5 *Synthesis of InP/ZnO/SiO_2*

Silica shelling of metal oxide shelled InP QDs was necessary to stabilize the QD sample under electron beam for EDS imaging. Adapting from literature preparation method[64], InP/ZnO QDs (0.04 mmol In) were first suspended in 9 mL of cyclohexane. Then, 1.3 mL of Igepal CO-520 (surfactant) and 150 µL ammonia (20%, catalyst) were added to the suspension. The cloudy mixture was sonicated for 10 minutes. Finally, 200 µL of TEOS was added dropwise over 2 min and stirred for 1 day to complete silica shelling of the QDs. The product was precipitated by centrifugation, washed with water twice, and redispersed in water.

3.4.6 *Characterization techniques*

^{1}H NMR spectra were collected on a 300 MHz Bruker Avance spectrometer. UV−vis spectra were collected on a Cary 5000 spectrophotometer from Agilent. Fluorescence and absolute quantum yield measurements were taken on a Horiba Jobin Yvon FluoroMax-4 fluorescence spectrophotometer with the QuantaPhi integrating sphere accessory. Powder X-ray diffraction spectra were collected on solid films drop-cast onto a Si wafer using a Bruker D8 Discover diffractometer. QD solids were digested with H_2O_2 and nitric acid overnight and diluted with 18 MΩ water to prepare ICP samples with which ICP-OES was performed using a PerkinElmer Optima 8300. All samples were purified by size-selective purification prior to the analysis and analyzed once except for as-synthesized InP QDs, for which the In:P ratio has been very consistent across at least 10 samples prepared at varying concentrations. Transmission electron microscopy (TEM) images were collected on an FEI Tecnai G2 F20 microscope at 200 kV. TEM samples were prepared by spotting 3 µL of a dilute solution of QDs dispersed in toluene onto an ultrathin carbon on holey carbon support film purchased from Ted Pella. Size distribution analysis was performed on >300 individual NCs per sample.

P Kα and Kβ X-ray emission spectroscopy (XES) measurements were performed on a laboratory spectrometer, to be described in Abramson, et al.[65], with a design similar to that of Holden et al.[66] and where the methodology of Stein et al.[18] was used for estimating the oxidation state. The spectrometer is set up in the N_2-filled glove box and uses a low-power, unfocused X-ray tube (Varex VF-80, 100 W) to illuminate the sample, whose emitted X-rays are analyzed by a 10 cm radius of curvature cylindrical crystal analyzer and detected using a new homemade CMOS direct-exposure color X-ray camera. The two multiplexed spectrometers are tuned to the P Kα and Kβ emission energies, respectively. Data collection followed the methodology from Abramson, et al.[65] InP QD samples were dropcast onto Si wafer with a spot size of ~5 mm diameter. The Kα emission spectra were analyzed using linear combination fitting with the nonlinear least-squares fitting Python package LMFIT.36 (described in more detail in Stein et al.). Briefly, two oxidation state components were fit using bulk GaP (2013.57 eV) and Na_2HPO_4 (2014.55 eV) measurements as reference standards.

Extended X-ray absorption fine structure (EXAFS) spectroscopy experiments were conducted on Beamline 20-BM of the Advanced Photon Source at Argonne National Laboratory. 20-BM is a spectroscopy beamline equipped with a Bending Magnet source and Si 111 monochromator. Zinc K-edge XAS data was collected in transmission mode over an energy range of 9460 eV-10515 eV (200 eV below the Zn-K edge of 9660.76 eV to approximately 855 eV above). A total of 430 data points were collected for each scan. XAS data processing and analysis was executed using XAS Viewer within the LARCH software package. First, the transmission data were plotted as $\mu(E) = -\log(I_{Transmitted}/I_0)$. Next, four scans each for "InP + $ZnEt_2$" and "InP/ZnO (2 cycles)" were deglitched (point removal) and averaged together reduce noise level. Only a single scan was available for "InP + Zn stearate" due to beam dropout. Raw μ(E) for each sample was

normalized with linear and quadratic functions for pre- and post-edge energy ranges respectively.

3.4.7 *Theory: choice of basis and method*

Quasi-spherical InP quantum dot, $In_{77}P_{77}$ (diameter ~2 nm), was constructed using the bulk zinc blende crystal structure. The undoped structure conformed to a C_{3v} symmetry before optimization. Core-shell MOx structures were built from the InP core by exchanging surface In with M (where M=Zn, Cd, Ga, Al) and P with O to form $In_{x-y}P_{x-y}/M_yO_y$. Ground-state geometric optimizations were performed, and the structures were considered optimized when both the forces [maximum and root-mean-square (rms) of the force 0.000450 and 0.000300 Hartree/Bohr, respectively] and displacement [maximum and rms displacement 0.00018 and 0.0012 Bohr, respectively] values were below the threshold criteria. Surface dangling bonds were terminated using a pseudo-hydrogen capping scheme to compensate surface ions (±1/3 to passivate the pure, InP quantum dot) resulting in an $In_{77}P_{77}H_{108}$ structure for the pure, non-shelled system. These systems are expected to exhibit quantum confinement (Bohr exciton radius is 10 nm for InP), however the diameters of the prepared dots are similar to those able to be created experimentally.[20] Calculations were conducted using the Gaussian software package[67] using the Perdew, Burke, and Ernzerhof hybrid functional (PBE0)[68-70] to compute the Kohn-Sham ground-state electronic structure. The Los Alamos National Lab 2-Double Zeta (LANL2DZ) pseudopotential and associated basis sets[71-74] were used. This combination is able to fairly accurately reproduce the experimentally-observed 3.7 eV band gap[6] (computational gap is 3.89 eV, +5% in relation to experiment). The electronic structures of excited states were calculated using time-dependent DFT (TD-DFT) within the linear-response framework.[75-77]

3.4.8 *Optimized structures of $In_{77}P_{77}$ and $In_{31}P_{31}/M_{46}O_{46}$*

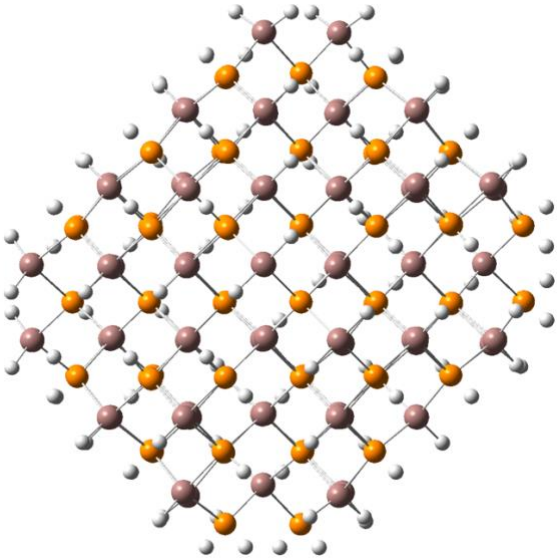

$In_{77}P_{77}H_{108}$

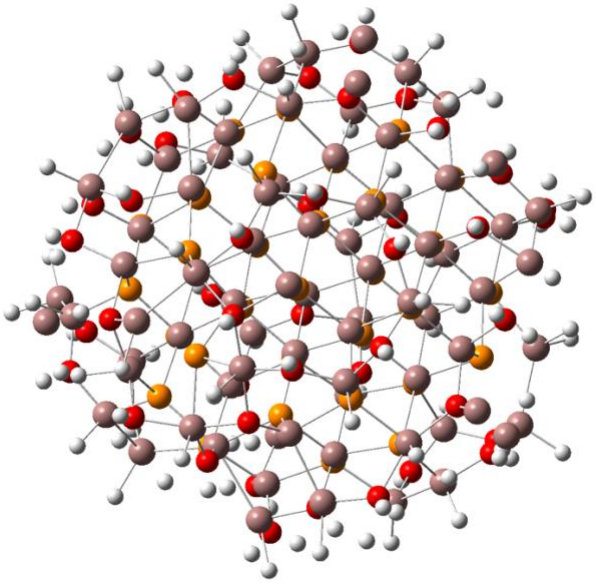

$In_{77}P_{31}O_{46}H_{108}$

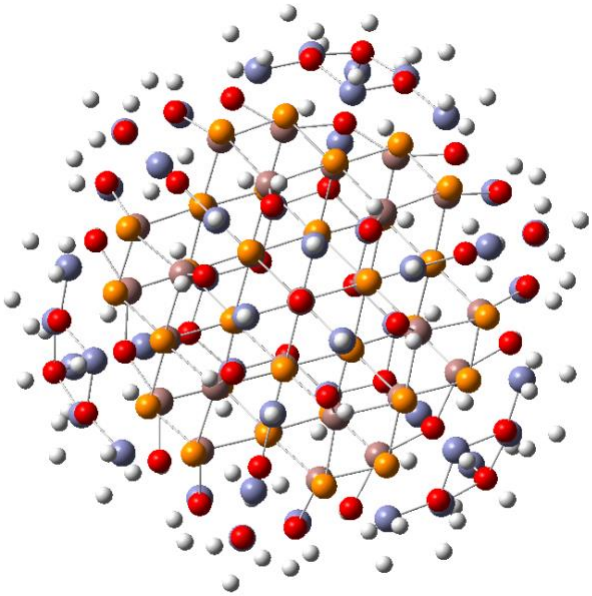

$In_{31}P_{31}Zn_{46}O_{46}H_{108}$

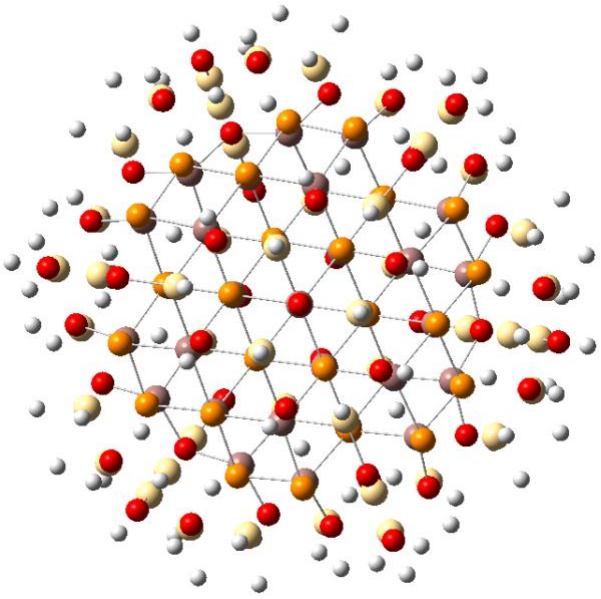

$In_{31}P_{31}Cd_{46}O_{46}H_{108}$

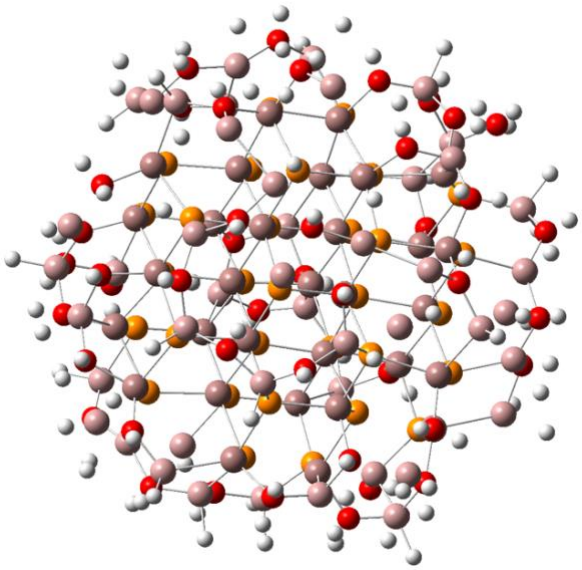

$In_{31}P_{31}Ga_{46}O_{46}H_{108}$

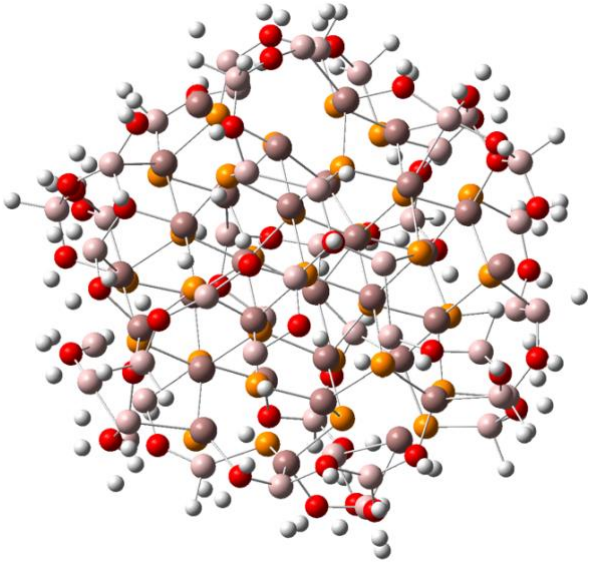

$In_{31}P_{31}Al_{46}O_{46}H_{108}$

3.4.9 *Calculation of Zn mmol equivalents for unit cell monolayers (ML)*

When examining the structure of zinc blende and wurtzite lattices, the (111) facet of zinc blende structure (e.g. InP QD core) and the (1010) facet of wurtzite structure (e.g. ZnO shell) are well-matched for continuous growth (without taking lattice parameter into account). This leads us to assume the shell growth in the *c* direction. One unit cell monolayer shell growth on ~3.0 nm InP QD core (c = 0.52 nm for wurtzite ZnO) amounts to 4.04 nm diameter core/shell, which has a volume of 34.53 nm^3 ($V_{core/shell}$ or V_{cs}). From here, the volume of shell (V_s) can be calculated by subtracting the volume of InP core to approximate the number of ZnO unit cells occupying the shell volume. From the number of In and Zn atoms per unit cell, the number of total In and Zn atoms was estimated to lead to the results in **Table 3.8** of Zn equivalents calculation.

Table 3.8. Zn equivalents to In for unit cell monolayers of ZnO growth on 3 nm InP QDs.

	V_{cs} (nm^3)	V_s (nm^3)	V_s/V_{ZnO}	# In	# Zn	Zn:In
InP QD 3 nm	-	14.14	-	279.78	-	-
ZnO ML 0.5	22.84	8.70	182.70	279.78	548.09	2.0
ZnO ML 1	34.53	20.39	428.19	279.78	1284.58	4.6
ZnO ML 1.5	49.65	35.51	745.77	279.78	2237.30	8.0
ZnO ML 2	68.64	54.50	1144.69	279.78	3434.08	12.3
ZnO ML 2.5	91.95	77.82	1634.25	279.78	4902.75	17.5

3.5 REFERENCES

(1) Kovalenko, M. V.; Manna, L.; Cabot, A.; Hens, Z.; Talapin, D. V.; Kagan, C. R.; Klimov, V. I.; Rogach, A. L.; Reiss, P.; Milliron, D. J.; Guyot-Sionnnest, P.; Konstantatos, G.; Parak, W. J.; Hyeon, T.; Korgel, B. A.; Murray, C. B.; Heiss, W. Prospects of Nanoscience with Nanocrystals. *ACS Nano* **2015**, *9* (2), 1012–1057.

(2) Shu, Y.; Lin, X.; Qin, H.; Hu, Z.; Jin, Y.; Peng, X. Quantum Dots for Display. *Angew.Chem.Int. Ed.* **2020**, *59*, 22312–22323.

(3) Jang, E.; Kim, Y.; Won, Y.-H.; Jang, H.; Choi, S.-M. Environmentally Friendly InP-Based Quantum Dots for Efficient Wide Color Gamut Displays. *ACS Energy Lett.* **2020**, *5* (4), 1316–1327.

(4) Kagan, C. R.; Bassett, L. C.; Murray, C. B.; Thompson, S. M. Colloidal Quantum Dots as Platforms for Quantum Information Science. *Chem. Rev.* **2021**, *121* (5), 3186–3233.

(5) Cao, F.; Wang, S.; Wang, F.; Wu, Q.; Zhao, D.; Yang, X. A Layer-by-Layer Growth Strategy for Large-Size InP/ZnSe/ZnS Core–Shell Quantum Dots Enabling High-Efficiency Light-Emitting Diodes. *Chem. Mater.* **2018**, *30* (21), 8002–8007.

(6) Won, Y.-H.; Cho, O.; Kim, T.; Chung, D.-Y.; Kim, T.; Chung, H.; Jang, H.; Lee, J.; Kim, D.; Jang, E. Highly Efficient and Stable InP/ZnSe/ZnS Quantum Dot Light-Emitting Diodes. *Nature* **2019**, *575* (7784), 634–638.

(7) Li, Y.; Hou, X.; Dai, X.; Yao, Z.; Lv, L.; Jin, Y.; Peng, X. Stoichiometry-Controlled InP-Based Quantum Dots: Synthesis, Photoluminescence, and Electroluminescence. *J. Am. Chem. Soc.* **2019**, *141* (16), 6448–6452.

(8) Li, H.; Zhang, W.; Bian, Y.; Ahn, T. K.; Shen, H.; Ji, B. ZnF2-Assisted Synthesis of Highly Luminescent InP/ZnSe/ZnS Quantum Dots for Efficient and Stable Electroluminescence. *Nano Lett.* **2022**, *22* (10), 4067–4073.

(9) Toufanian, R.; Piryatinski, A.; Mahler, A. H.; Iyer, R.; Hollingsworth, J. A.; Dennis, A. M. Bandgap Engineering of Indium Phosphide-Based Core/Shell Heterostructures Through Shell Composition and Thickness. *Front Chem* **2018**, *6*.

(10) Eren, G. O.; Sadeghi, S.; Bahmani Jalali, H.; Ritter, M.; Han, M.; Baylam, I.; Melikov, R.; Onal, A.; Oz, F.; Sahin, M.; Ow-Yang, C. W.; Sennaroglu, A.; Lechner, R. T.; Nizamoglu, S. Cadmium-

Free and Efficient Type-II InP/ZnO/ZnS Quantum Dots and Their Application for LEDs. *ACS Appl. Mater. Interfaces* **2021**, *13* (27), 32022–32030.

(11) Jo, J.-H.; Jo, D.-Y.; Lee, S.-H.; Yoon, S.-Y.; Lim, H.-B.; Lee, B.-J.; Do, Y. R.; Yang, H. InP-Based Quantum Dots Having an InP Core, Composition-Gradient ZnSeS Inner Shell, and ZnS Outer Shell with Sharp, Bright Emissivity, and Blue Absorptivity for Display Devices. *ACS Appl. Nano Mater.* **2020**, *3* (2), 1972–1980.

(12) Lee, S. H.; Kim, Y.; Jang, H.; Min, J. H.; Oh, J.; Jang, E.; Kim, D. The Effects of Discrete and Gradient Mid-Shell Structures on the Photoluminescence of Single InP Quantum Dots. *Nanoscale* **2019**, *11* (48), 23251–23258.

(13) Zhang, H.; Ma, X.; Lin, Q.; Zeng, Z.; Wang, H.; Li, L. S.; Shen, H.; Jia, Y.; Du, Z. High-Brightness Blue InP Quantum Dot-Based Electroluminescent Devices: The Role of Shell Thickness. *J. Phys. Chem. Lett.* **2020**, *11* (3), 960–967.

(14) Ramasamy, P.; Kim, B.; Lee, M.-S.; Lee, J.-S. Beneficial Effects of Water in the Colloidal Synthesis of InP/ZnS Core–Shell Quantum Dots for Optoelectronic Applications. *Nanoscale* **2016**, *8* (39), 17159–17168.

(15) Tessier, M. D.; Baquero, E. A.; Dupont, D.; Grigel, V.; Bladt, E.; Bals, S.; Coppel, Y.; Hens, Z.; Nayral, C.; Delpech, F. Interfacial Oxidation and the Photoluminescence of InP-Based Core/Shell Quantum Dots. *Chem. Mater.* **2018**, *30* (19), 6877–6883.

(16) Cros-Gagneux, A.; Delpech, F.; Nayral, C.; Cornejo, A.; Coppel, Y.; Chaudret, B. Surface Chemistry of InP Quantum Dots: A Comprehensive Study. *J. Am. Chem. Soc.* **2010**, *132* (51), 18147–18157.

(17) Virieux, H.; Le Troedec, M.; Cros-Gagneux, A.; Ojo, W.-S.; Delpech, F.; Nayral, C.; Martinez, H.; Chaudret, B. InP/ZnS Nanocrystals: Coupling NMR and XPS for Fine Surface and Interface Description. *J. Am. Chem. Soc.* **2012**, *134* (48), 19701–19708.

(18) Stein, J. L.; Holden, W. M.; Venkatesh, A.; Mundy, M. E.; Rossini, A. J.; Seidler, G. T.; Cossairt, B. M. Probing Surface Defects of InP Quantum Dots Using Phosphorus Kα and Kβ X-Ray Emission Spectroscopy. *Chem. Mater.* **2018**, *30* (18), 6377–6388.

(19) Guzelian, A. A.; Katari, J. E. B.; Kadavanich, A. V.; Banin, U.; Hamad, K.; Juban, E.; Alivisatos, A. P.; Wolters, R. H.; Arnold, C. C.; Heath, J. R. Synthesis of Size-Selected, Surface-Passivated InP Nanocrystals. *J. Phys. Chem.* **1996**, *100* (17), 7212–7219.

(20) Cho, E.; Kim, T.; Choi, S.; Jang, H.; Min, K.; Jang, E. Optical Characteristics of the Surface Defects in InP Colloidal Quantum Dots for Highly Efficient Light-Emitting Applications. *ACS Appl. Nano Mater.* **2018**, *1* (12), 7106–7114.

(21) Van Avermaet, H.; Schiettecatte, P.; Hinz, S.; Giordano, L.; Ferrari, F.; Nayral, C.; Delpech, F.; Maultzsch, J.; Lange, H.; Hens, Z. Full-Spectrum InP-Based Quantum Dots with Near-Unity Photoluminescence Quantum Efficiency. *ACS Nano* **2022**, *16* (6), 9701–9712.

(22) Janke, E. M.; Williams, N. E.; She, C.; Zherebetskyy, D.; Hudson, M. H.; Wang, L.; Gosztola, D. J.; Schaller, R. D.; Lee, B.; Sun, C.; Engel, G. S.; Talapin, D. V. Origin of Broad Emission Spectra in InP Quantum Dots: Contributions from Structural and Electronic Disorder. *J. Am. Chem. Soc.* **2018**, *140* (46), 15791–15803.

(23) Vikram, A.; Zahid, A.; Bhargava, S. S.; Jang, H.; Sutrisno, A.; Khare, A.; Trefonas, P.; Shim, M.; Kenis, P. J. A. Unraveling the Origin of Interfacial Oxidation of InP-Based Quantum Dots: Implications for Bioimaging and Optoelectronics. *ACS Appl. Nano Mater.* **2020**, *3* (12), 12325–12333.

(24) Cui, J.; Beyler, A. P.; Marshall, L. F.; Chen, O.; Harris, D. K.; Wanger, D. D.; Brokmann, X.; Bawendi, M. G. Direct Probe of Spectral Inhomogeneity Reveals Synthetic Tunability of Single-Nanocrystal Spectral Linewidths. *Nat. Chem.* **2013**, *5* (7), 602–606.
(25) Yazdani, N.; Volk, S.; Yarema, O.; Yarema, M.; Wood, V. Size, Ligand, and Defect-Dependent Electron–Phonon Coupling in Chalcogenide and Perovskite Nanocrystals and Its Impact on Luminescence Line Widths. *ACS Photonics* **2020**, *7* (5), 1088–1095.
(26) Hazarika, A.; Fedin, I.; Hong, L.; Guo, J.; Srivastava, V.; Cho, W.; Coropceanu, I.; Portner, J.; Diroll, B. T.; Philbin, J. P.; Rabani, E.; Klie, R.; Talapin, D. V. Colloidal Atomic Layer Deposition with Stationary Reactant Phases Enables Precise Synthesis of "Digital" II–VI Nano-Heterostructures with Exquisite Control of Confinement and Strain. *J. Am. Chem. Soc.* **2019**, *141* (34), 13487–13496.
(27) Ithurria, S.; Talapin, D. V. Colloidal Atomic Layer Deposition (c-ALD) Using Self-Limiting Reactions at Nanocrystal Surface Coupled to Phase Transfer between Polar and Nonpolar Media. *J. Am. Chem. Soc.* **2012**, *134* (45), 18585–18590.
(28) Loiudice, A.; Strach, M.; Saris, S.; Chernyshov, D.; Buonsanti, R. Universal Oxide Shell Growth Enables in Situ Structural Studies of Perovskite Nanocrystals during the Anion Exchange Reaction. *J. Am. Chem. Soc.* **2019**, *141* (20), 8254–8263.
(29) Segura Lecina, O.; Hope, M. A.; Venkatesh, A.; Björgvinsdóttir, S.; Rossi, K.; Loiudice, A.; Emsley, L.; Buonsanti, R. Colloidal-ALD-Grown Hybrid Shells Nucleate via a Ligand–Precursor Complex. *J. Am. Chem. Soc.* **2022**, *144* (9), 3998–4008.
(30) Sayevich, V.; Robinson, Z. L.; Kim, Y.; Kozlov, O. V.; Jung, H.; Nakotte, T.; Park, Y.-S.; Klimov, V. I. Highly Versatile Near-Infrared Emitters Based on an Atomically Defined HgS Interlayer Embedded into a CdSe/CdS Quantum Dot. *Nat. Nanotechnol.* **2021**, *16*, 673–679.
(31) Snee, P. T. DFT Calculations of InP Quantum Dots: Model Chemistries, Surface Passivation, and Open-Shell Singlet Ground States. *J. Phys. Chem. C* **2021**, *125* (21), 11765–11772.
(32) Rodosthenous, P.; Gómez-Campos, F. M.; Califano, M. Tuning the Radiative Lifetime in InP Colloidal Quantum Dots by Controlling the Surface Stoichiometry. *J. Phys. Chem. Lett.* **2020**, *11* (23), 10124–10130.
(33) Rusishvili, M.; Wippermann, S.; Talapin, D. V.; Galli, G. Stoichiometry of the Core Determines the Electronic Structure of Core–Shell III–V/II–VI Nanoparticles. *Chem. Mater.* **2020**, *32* (22), 9798–9804.
(34) Hussein, M. T.; Kasim, T.; Abdulsattar, M. A.; Kaka, A. K. Density Functional Theory Study of InP Quantum Dot and Oxidized Surface. *Int. J. Appl. Innov. Eng. Manag.* **2014**, *3* (5), 9.
(35) Chandrasekaran, V.; Tessier, M. D.; Dupont, D.; Geiregat, P.; Hens, Z.; Brainis, E. Nearly Blinking-Free, High-Purity Single-Photon Emission by Colloidal InP/ZnSe Quantum Dots. *Nano Letters* **2017**, *17* (10), 6104–6109.
(36) Dennis, A. M.; Buck, M. R.; Wang, F.; Hartmann, N. F.; Majumder, S.; Casson, J. L.; Watt, J. D.; Doorn, S. K.; Htoon, H.; Sykora, M.; Hollingsworth, J. A. Role of Interface Chemistry in Opening New Radiative Pathways in InP/CdSe Giant Quantum Dots with Blinking-Suppressed Two-Color Emission. *Adv. Funct. Mater.* **2019**, *29* (37), 1809111.
(37) Efros, A. L.; Nesbitt, D. J. Origin and Control of Blinking in Quantum Dots. *Nat. Nanotech.* **2016**, *11* (8), 661–671.
(38) Lingerfelt, D. B.; Williams-Young, D. B.; Petrone, A.; Li, X. Direct Ab Initio (Meta-)Surface-Hopping Dynamics. *J. Chem. Theory Comput.* **2016**, *12* (3), 935–945.
(39) Avouris, P.; Gelbart, W. M.; El-Sayed, M. A. Nonradiative Electronic Relaxation under Collision-Free Conditions. *Chem. Rev.* **1977**, *77* (6), 793–833.

(40) Send, R.; Furche, F. First-Order Nonadiabatic Couplings from Time-Dependent Hybrid Density Functional Response Theory: Consistent Formalism, Implementation, and Performance. *J. Chem. Phys.* **2010**, *132* (4), 044107.
(41) Gary, D. C.; Terban, M. W.; Billinge, S. J. L.; Cossairt, B. M. Two-Step Nucleation and Growth of InP Quantum Dots via Magic-Sized Cluster Intermediates. *Chem. Mater.* **2015**, *27* (4), 1432–1441.
(42) Park, N.; Eagle, F. W.; DeLarme, A. J.; Monahan, M.; LoCurto, T.; Beck, R.; Li, X.; Cossairt, B. M. Tuning the Interfacial Stoichiometry of InP Core and InP/ZnSe Core/Shell Quantum Dots. *J. Chem. Phys.* **2021**, *155* (8), 084701.
(43) Shen, Y.; Gee, M. Y.; Tan, R.; Pellechia, P. J.; Greytak, A. B. Purification of Quantum Dots by Gel Permeation Chromatography and the Effect of Excess Ligands on Shell Growth and Ligand Exchange. *Chem. Mater.* **2013**, *25* (14), 2838–2848.
(44) Roberge, A.; Stein, J. L.; Shen, Y.; Cossairt, B. M.; Greytak, A. B. Purification and In Situ Ligand Exchange of Metal-Carboxylate-Treated Fluorescent InP Quantum Dots via Gel Permeation Chromatography. *J. Phys. Chem. Lett.* **2017**, *8* (17), 4055–4060.
(45) Chen, P. E.; Anderson, N. C.; Norman, Z. M.; Owen, J. S. Tight Binding of Carboxylate, Phosphonate, and Carbamate Anions to Stoichiometric CdSe Nanocrystals. *J. Am. Chem. Soc.* **2017**, *139* (8), 3227–3236.
(46) Gary, D. C.; Flowers, S. E.; Kaminsky, W.; Petrone, A.; Li, X.; Cossairt, B. M. Single-Crystal and Electronic Structure of a 1.3 Nm Indium Phosphide Nanocluster. *J. Am. Chem. Soc.* **2016**, *138* (5), 1510–1513.
(47) Zhao, Q.; Kulik, H. J. Electronic Structure Origins of Surface-Dependent Growth in III–V Quantum Dots. *Chem. Mater.* **2018**, *30* (20), 7154–7165.
(48) Hanrahan, M. P.; Stein, J. L.; Park, N.; Cossairt, B. M.; Rossini, A. J. Elucidating the Location of Cd2+ in Post-synthetically Treated InP Quantum Dots Using Dynamic Nuclear Polarization 31P and 113Cd Solid-State NMR Spectroscopy. *J. Phys.Chem. C* **2021**, *125* (5), 2956-2965.
(49) Holder, C. F.; Schaak, R. E. Tutorial on Powder X-Ray Diffraction for Characterizing Nanoscale Materials. *ACS Nano* **2019**, *13* (7), 7359–7365.
(50) Trigg, E. B. DebyeByPy. 2015, GitHub repository http://github.com/etrigg/DebyeByPy.
(51) Calvin, J. J.; Kaufman, T. M.; Sedlak, A. B.; Crook, M. F.; Alivisatos, A. P. Observation of ordered organic capping ligands on semiconducting quantum dots via powder X-ray diffraction. *Nat. Commun.***2021**, *12*, 2663.
(52) Ping, L. K.; Berhanuddin, D. D.; Mondal, A. K.; Menon, P. S.; Mohamed, M. A. Properties and Perspectives of Ultrawide Bandgap Ga2O3 in Optoelectronic Applications. *Chin. J. Phys.* **2021**, *73*, 195–212.
(53) Pourret, A.; Guyot-Sionnest, P.; Elam, J. W. Atomic Layer Deposition of ZnO in Quantum Dot Thin Films. *Adv. Mater.* **2009**, *21* (2), 232–235.
(54) Tsui, E. Y.; Hartstein, K. H.; Gamelin, D. R. Selenium Redox Reactivity on Colloidal CdSe Quantum Dot Surfaces. *J. Am. Chem. Soc.* **2016**, *138* (35), 11105–11108.
(55) Kim, S.; Kim, T.; Kang, M.; Kwak, S. K.; Yoo, T. W.; Park, L. S.; Yang, I.; Hwang, S.; Lee, J. E.; Kim, S. K.; Kim, S.-W. Highly Luminescent InP/GaP/ZnS Nanocrystals and Their Application to White Light-Emitting Diodes. *J. Am. Chem. Soc.* **2012**, *134* (8), 3804–3809.
(56) Sadeghi, S.; Bahmani Jalali, H.; Melikov, R.; Ganesh Kumar, B.; Mohammadi Aria, M.; Ow-Yang, C. W.; Nizamoglu, S. Stokes-Shift-Engineered Indium Phosphide Quantum Dots for Efficient Luminescent Solar Concentrators. *ACS Appl. Mater. Interfaces* **2018**, *10* (15), 12975–12982.

(57) Taylor, M. G.; Kulik, H. J. Mapping the Origins of Surface- and Chemistry-Dependent Doping Trends in III–V Quantum Dots with Density Functional Theory. *Chem. Mater.* **2021**, *33* (17), 7113–7123.
(58) Reid, K. R., McBride, J. R., Freymeyer, N. J., Thal, L. B. & Rosenthal, S. J. Chemical Structure, Ensemble and Single-Particle Spectroscopy of Thick-Shell InP–ZnSe Quantum Dots. *Nano Lett.* **2018**, *18*, 709–716.
(59) Hollingsworth, J. A.; Htoon, H.; McBride, J.; Orfield, N. J.; Mishra, N.; Hanson, C. J.; Click, S. M.; Singh, A. *Suppressed-Blinking Green (and Infrared)-Emitting "Giant" Quantum Dots (GQDs): From Synthesis to Structure to Function*; Los Alamos National Laboratory (LANL), **2017**.
(60) Gary, D. C.; Cossairt, B. M. Role of Acid in Precursor Conversion During InP Quantum Dot Synthesis. *Chem. Mater.* **2013**, *25* (12), 2463–2469.
(61) Park, N.; Monahan, M.; Ritchhart, A.; Friedfeld, M. R.; Cossairt, B. M. Synthesis of In37P20(O2CR)51 Clusters and Their Conversion to InP Quantum Dots. *JoVE (Journal of Visualized Experiments)* **2019**, No. 147, e59425.
(62) Shen, Y.; Roberge, A.; Tan, R.; Gee, M. Y.; Gary, D. C.; Huang, Y.; Blom, D. A.; Benicewics, B. C.; Cossairt, B. M.; Greytak, A. B. Gel Permeation Chromatography as a Multifunctional Processor for Nanocrystal Purification and On-Column Ligand Exchange Chemistry. *Chem. Sci.* **2016**, *7*, 5671–5679.
(63) Lim, J.; Bae, W. K.; Lee, D.; Nam, M. K.; Jung, J.; Lee, C.; Char, K.; Lee, S. InP@ZnSeS, Core@Composition Gradient Shell Quantum Dots with Enhanced Stability. *Chem. Mater.* **2011**, *23* (20), 4459–4463.
(64) Darbandi, M.; Lu, W.; Fang, J.; Nann, T. Silica Encapsulation of Hydrophobically Ligated PbSe Nanocrystals. *Langmuir* **2006**, *22* (9), 4371–4375.
(65) Abramson, J. E.; Seidler, G. T. *et al.* Laboratory X-ray Emission Spectrometer for Phosphorus Kα and Kβ of Air-Sensitive Samples. **2022** *[Unpublished manuscript]*.
(66) Holden, W. M.; Hoidn, O. R.; Ditter, A. S.; Seidler, G. T.; Kas, J.; Stein, J. L.; Cossairt, B. M.; Kozimor, S. A.; Guo, J.; Ye, Y.; Marcus, M. A.; Fakra, S. A Compact Dispersive Refocusing Rowland Circle X-Ray Emission Spectrometer for Laboratory, Synchrotron, and XFEL Applications. *Review of Scientific Instruments* **2017**, *88* (7), 073904.
(67) M. J. Frisch, G. W. Trucks, H. B. Schlegel, G. E. Scuseria, M. A. Robb, J. R. Cheeseman, G. Scalmani, V. Barone, G. A. Petersson, H. Nakatsuji, X. Li, M. Caricato, A. V. Marenich, J. Bloino, B. G. Janesko, R. Gomperts, B. Mennucci, H. P. Hratchian, J. V. Ortiz, A. F. Izmaylov, J. L. Sonnenberg, D. Williams-Young, F. Ding, F. Lipparini, F. Egidi, J. Goings, B. Peng, A. Petrone, T. Henderson, D. Ranasinghe, V. G. Zakrzewski, J. Gao, N. Rega, G. Zheng, W. Liang, M. Hada, M. Ehara, K. Toyota, R. Fukuda, J. Hasegawa, M. Ishida, T. Nakajima, Y. Honda, O. Kitao, H. Nakai, T. Vreven, K. Throssell, J. A. Montgomery, Jr., J. E. Peralta, F. Ogliaro, M. J. Bearpark, J. J. Heyd, E. N. Brothers, K. N. Kudin, V. N. Staroverov, T. A. Keith, R. Kobayashi, J. Normand, K. Raghavachari, A. P. Rendell, J. C. Burant, S. S. Iyengar, J. Tomasi, M. Cossi, J. M. Millam, M. Klene, C. Adamo, R. Cammi, J. W. Ochterski, R. L. Martin, K. Morokuma, O. Farkas,; J. B. Foresman, and D. J. Fox. Gaussian 16, Revision B.01, 2016.
(68) Ernzerhof, M.; Scuseria, G. E. Assessment of the Perdew–Burke–Ernzerhof Exchange-Correlation Functional. *J. Chem. Phys.* **1999**, *110* (11), 5029–5036.
(69) Adamo, C.; Barone, V. Toward Reliable Density Functional Methods without Adjustable Parameters: The PBE0 Model. *J. Chem. Phys.* **1999**, *110* (13), 6158–6170.

(70) Perdew, J. P.; Burke, K.; Ernzerhof, M. Errata: Generalized gradient approximation made simple. *Phys. Rev. Lett.* **1997**, *78*, 1396.
(71) Dunning Jr., T. H; Hay, P. J. *Methods of Electronic Structure Theory, Ed. H. F. Schaefer III*; Plenum Press: New York, 1977; Vol. 3.
(72) Wadt, W. R.; Hay, P. J. Ab Initio Effective Core Potentials for Molecular Calculations. Potentials for Main Group Elements Na to Bi. *J. Chem. Phys.* **1985**, *82* (1), 284–298.
(73) Hay, P. J.; Wadt, W. R. Ab Initio Effective Core Potentials for Molecular Calculations. Potentials for the Transition Metal Atoms Sc to Hg. *J. Chem. Phys.* **1985**, *82* (1), 270–283.
(74) Hay, P. J.; Wadt, W. R. Ab Initio Effective Core Potentials for Molecular Calculations. Potentials for K to Au Including the Outermost Core Orbitals. *J. Chem. Phys.* **1985**, *82* (1), 299–310.
(75) Casida, M. E. *Recent Advances in Density Functional Methods: Part I, Ed. D. P. Chong*; World Scientific: Singapore, 1995; Vol. 1.
(76) Dreuw, A.; Head-Gordon, M. Single-Reference Ab Initio Methods for the Calculation of Excited States of Large Molecules. *Chem. Rev.* **2005**, *105* (11), 4009–4037.
(77) Stratmann, R. E.; Scuseria, G. E.; Frisch, M. J. An Efficient Implementation of Time-Dependent Density-Functional Theory for the Calculation of Excitation Energies of Large Molecules. *The J. Chem. Phys.* **1998**, *109* (19), 8218–8224.

VITA

Nayon Park was born in Chuncheon, South Korea. She moved to Singapore with her family when she was 11 and attended school there until moving across the globe to go to Carleton College in Minnesota, USA. For two summers during college, she worked in the lab of Prof. Christopher Bielawski at Ulsan National Institute of Technology (UNIST) in Ulsan, South Korea where she was able to see herself going to graduate school for chemistry. The summer research experience and taking Chemistry at the Nanoscale course in her junior year spring with Prof. Trish Ferrett sparked her interest in materials chemistry and especially in the colorful world of quantum dots. After graduating from college, she moved to Seattle for UW's chemistry program where she joined Prof. Brandi Cossairt's lab to explore the surface chemistry and photoluminescence properties of indium phosphide quantum dots. While in grad school, she was also actively involved with outreach and organizations across campus including Inclusion in Chemical Sciences (InCS), Clean Energy Institute (CEI) and Molecular Engineering Materials Center (MEM-C) outreach, and UAW 4121, the Union of Academic Student Employees and Postdocs at the University of Washington, where she was chemistry steward, Head Steward, and then Vice President. Outside of the lab and organizing, she enjoys spending time with her friends and family on hikes, travel, and with good food.